# Non-Hermitian effects in exciton-polariton systems

**Daniel Philip Comber-Todd**

A thesis submitted for the degree of
**Master of Philosophy**
of The Australian National University.

Nonlinear Physics Centre
Research School of Physics and Engineering
ANU College of Science

November, 2019

# Declaration

This thesis is an account of research undertaken at the Nonlinear Physics Centre, Research School of Physics and Engineering, ANU College of Science, The Australian National University, Canberra, Australia. Except where acknowledged in the customary manner, the material presented in this thesis is, to the best of my knowledge, original and has not been submitted in whole or part for a degree in any university.

Daniel Comber-Todd

November, 2019

# Acknowledgements

I must thank my supervisor, A/Prof Elena Ostrovskaya for her patient and generous guidance and support. She has served as a role model whose scientific integrity, intellectual rigour, and dedication to mentorship I aspire to. I would also like to thank the members of the ANU polariton BEC group for their enthusiasm and for many useful discussions. I am grateful for the company of my friends from the ANU Mountaineering Club, with whom I have shared many memorable adventures in my time in Canberra, and for the support provided by my friends and family.

The experiments described in Section 3.3 were performed by Tingge Gao, who also analysed the data. Elena Ostrovskaya suggested and produced initial analysis of the theory studied in Section 3.5.1.

# Abstract

In this thesis we study non-Hermitian aspects of exciton-polariton Bose-Einstein condensates. Exciton-polaritons are hybrid matter-light quasiparticles created when microcavity photons are strongly coupled to quantum well excitons, which are bound electron-hole pairs. Being composite bosons with a very low effective mass, exciton-polaritons can undergo Bose-Einstein condensation at relatively high temperatures - from cryogenic to as high as room temperature in some semiconductors. Exciton-polariton condensates are an experimentally attractive system due to the high transition temperature and ease of *in-situ* diagnostics. They are also fundamentally non-Hermitian because they exist in a balanced landscape of loss and gain, where excitation by a pump laser counteracts the radiative decay of polaritons. Because of their hybrid light-matter nature exciton-polariton condensates are also an ideal platform for designing new optoelectronic devices, and non-Hermitian effects may be useful to this end.

Hermiticity is posited as an axiom of quantum mechanics in order to ensure that energies are real. However in recent decades it has been shown that a class of non-Hermitian Hamiltonians which adhere to a weaker condition of symmetry under simultaneous spatial and time reversal (PT symmetry) can still have real energies. Many of the essential features of Hermitian quantum mechanics can be reproduced with such Hamiltonians. In general PT symmetric systems exhibit two phases, one in which eigenvalues are real, and another in which the eigenvectors spontaneously break the PT symmetry and eigenvalues are complex. The transition occurs at an exceptional point, a non-Hermitian degeneracy where eigenstates coincide as well as eigenvalues. EPs can also be observed in non-Hermitian systems lacking PT symmetry. This has led to a collection of interesting experiments in optical and other systems that provide analogues of non-Hermitian quantum mechanics because loss and gain are represented by an imaginary potential. In these systems PT symmetry breaking has allowed for enhanced sensing, loss-induced transparency, gain-induced suppression of lasing, and sensitive switching. Exciton-polariton condensates are inherently non-Hermitian as they experience loss and gain. However this aspect has been largely overlooked, apart from a few experiments which demonstrate EPs. Experiments in optical and other systems suggest that non-Hermitian effects in polaritons may be harnessed to design optoelectronic devices. In addition, the demonstration of PT symmetry breaking in yet another system is of inherent intellectual interest.

We aim to provide theoretical guidance for current and future experiments that exploit the non-Hermiticity of polariton condensates. One chapter focuses on a very simple PT symmetric system - a PT symmetric square well. This system is simple enough to be analytically tractable, but also exhibits interesting and subtle behaviour. We show how a nearly-PT symmetric square well can be implemented for polaritons using established trapping techniques. We further show that unavoidable PT asymmetry removes the PT symmetry breaking transition, but that most of this behaviour can easily be restored.

In support of recent experiments, another part of the work focuses on whispering gallery modes (WGMs) of polariton condensates in a shallow circular trap. We show that an interesting experimental effect - a robust blueshift of half a free spectral range under certain pumping conditions - can be attributed to coupling with a non-Hermitian resonator. We also discuss the viability of various schemes for reaching EPs of polariton WGMs, and present preliminary numerical results which show some of these schemes are viable.

The research presented in this thesis provides a road map for future experimental and theoretical work that will harness non-Hermitian effects beyond the observation of EPs in polariton condensates.

# Contents

# Introduction

## 1.1 Exciton-Polaritons

Exciton-polaritons are 2D quasiparticles that arise from strong coupling between optical microcavity modes and quantum well excitons. As composite bosons with a very small effective mass, they can undergo bose-einstein condensation at fairly high temperatures. In this section we review the basics of exciton-polaritons, and of exciton-polariton bose-einstein condensation. Our presentation of these topics follows that in Ref. [1]. We then present the accepted mean-field model used to describe experiments with exciton-polariton condensates and review methods of creating potentials for exciton-polaritons. After this, we summarise some interesting features of non-Hermitian systems including real spectra of Hamiltonians possessing parity-time symmetry, and exceptional points, which are non-Hermitian degeneracies. We review results from experiments in a few non-Hermitian systems, and briefly discuss nonlinear PT symmetric systems.

### 1.1.1 Optical Microcavities

Optical microcavities consist of two mirrors enclosing a thin layer of optical medium. High quality mirrors can be made from distributed Bragg reflectors (DBRs), which consist of alternating layers of two materials with different refractive indices, illustrated in Figure 1.1. Interference between light reflected and transmitted by the various layers leads to a stop-band - a region of very high reflectively - at certain wavelengths as shown in Figure 1.2. The high reflectivity of DBRs allows for microcavities with exceptionally high quality factors - typically on the order of $10^5$-$10^6$, resulting in long photon lifetimes.

The mirror arrangement in a microcavity leads to confinement of the electric field in the direction perpendicular to the mirror planes, and hence quantisation of the perpendicular component of the photon wave vector, which is given as

$$k_\perp = n_c \frac{2\pi}{\lambda_c},$$

(1.1)

where $n_c$ is the refractive index of the cavity, and $\lambda_c$ is the wavelength of the cavity mode. Upon decomposing the photon wave vector in to perpendicular and in-plane components, the energy of the cavity mode can be expressed as

$$E_{\text{cav}} = \frac{\hbar c}{n_c} \sqrt{k_\parallel^2 + k_\perp^2},$$

(1.2)

1
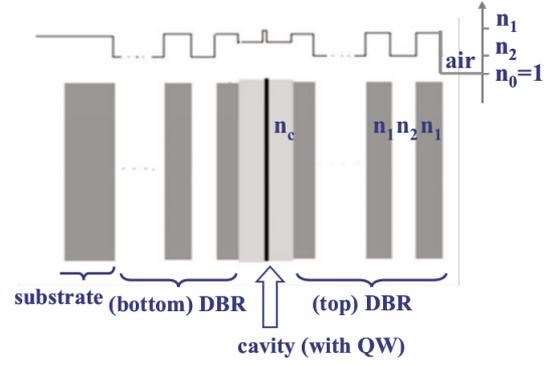
Figure 1.1: Schematic of a DBR microcavity used to produce exciton-polaritons. A thin quantum well with spacer material is sandwiched between two DBRs which confine photons. Reproduced from Ref. [1].
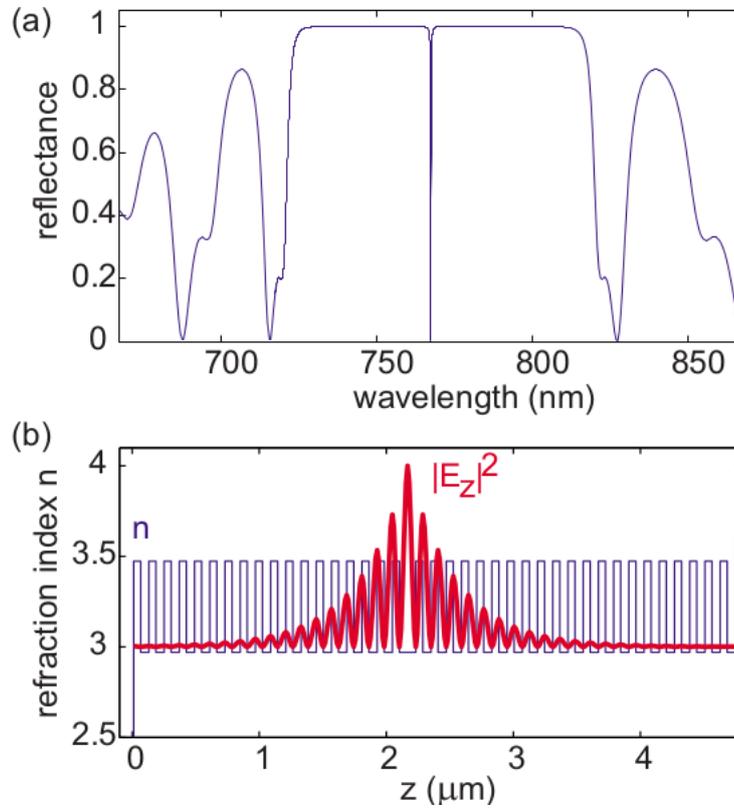


Figure 1.2: Reflectance of a DBR microcavity and electric field distribution inside the microcavity. Reproduced from Ref. [1].

where $k_\parallel$ is the component in the direction parallel to the mirrors. Confined photons have low in-plane momentum, so expanding Equation (1.2) around $k_\parallel = 0$ yields

$$E_{\text{cav}} \approx E_{\text{cav}}(k_\parallel = 0) + \frac{\hbar^2 k_\parallel^2}{2m_{\text{cav}}}. \tag{1.3}$$

The first term represents the rest energy of a cavity mode photon whereas the second term represents the kinetic energy contribution of in-plane motion. Consequently, confinement endows trapped photons with an effective mass given by

$$m_{\text{cav}} = \frac{E_{\text{cav}}(k_\parallel = 0)}{c^2 n_c^2}. \tag{1.4}$$

Typical effective masses are very low - around $10^{-5} m_{\text{e}^-}$.
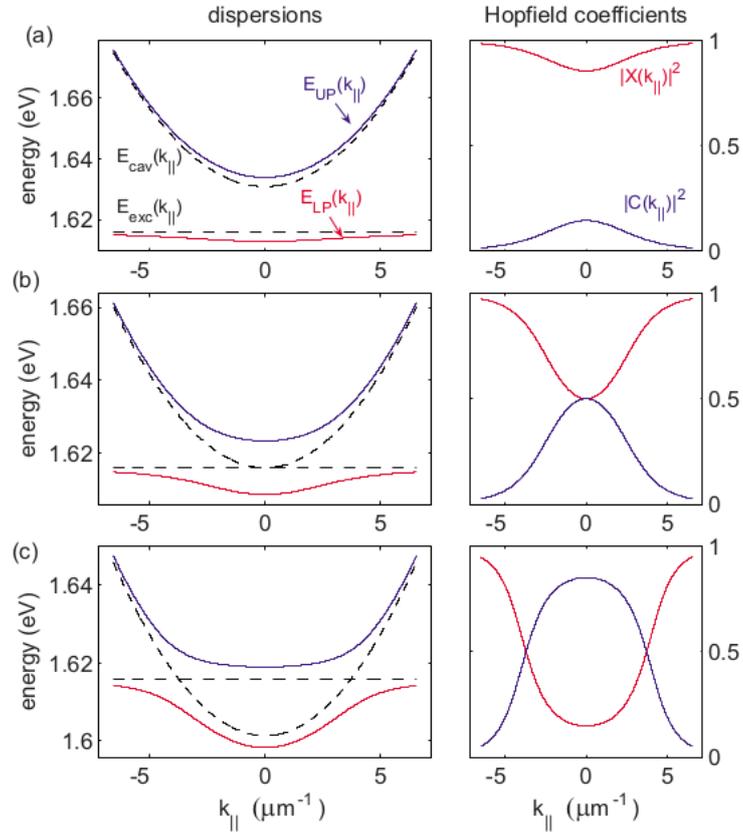


Figure 1.3: Polariton dispersions and corresponding Hopfield coefficients for detuning, $\Delta E = E_{\text{exc}}(0) - E_{\text{cav}}(0)$ equal to: (a) $2g_0$, (b) 0, (c) $-2g_0$. Dispersions of quantum well excitons and cavity photons are shown with dotted lines. Reproduced from Ref. [1].

### 1.1.2  Excitons

When an electron is excited to the valence band of a semiconductor it leaves behind a hole - a region of excess positive charge. The electron and hole interact via the Coulomb force, resulting in a bound pair - a neutral composite quasiparticle called an exciton,

analogous to a hydrogen atom[1]. Dielectric screening of the electric field reduces the effective strength of the Coulomb force, leading to large Bohr radius and low binding energy of excitons compared to hydrogen atoms. Typical values are $a_{\mathrm{B}} = 7\,\mathrm{nm}$ and $E_{\mathrm{B}} = 5\,\mathrm{meV}$. As composite quasiparticles, excitons behave as bosons for a bulk excitation in GaAs below the Mott density. Moreover, excitons present a dipole that can interact with the electric field.

In order to enhance the interaction with photons, excitons are confined to two dimensions. Confinement is achieved in a quantum well - a thin layer of semiconductor material surrounded by layers with higher bandgaps, which results in a confining potential. The quantum well is narrow enough that only one transverse mode is supported. This confinement results in a smaller Bohr radius and increased binding energy and oscillator strength.

### 1.1.3 Exciton-Polaritons

When a quantum well is placed at the antinode of a microcavity mode, excitons interact strongly with the optical mode. If the coupling rate between the excitons and the cavity mode is much larger than the relevant decay rates, a photon can interact with excitons many times before leaking from the cavity. The system is then best viewed in terms of new eigenstates, exciton-polaritons which are composite quasiparticles that are part photon and part exciton. Strong coupling is possible because of the high quality factor of semiconductor microcavities with DBR, and the enhanced optical interaction achieved by confining excitons to a quantum well.

More formally, under the rotating wave approximation the Hamiltonian can be decomposed into parts representing the cavity modes, the excitons, and their interaction. That is,

$$
\begin{aligned}
\hat{H} &= \hat{H}_{\mathrm{cav}} + \hat{H}_{\mathrm{exc}} + \hat{H}_I \\
&= \sum E_{\mathrm{cav}}(k_\parallel, k_c)\hat{a}^\dagger_{\mathbf{k}_\parallel}\hat{a}_{\mathbf{k}_\parallel} + \sum E_{\mathrm{exc}}(k_\parallel)\hat{b}^\dagger_{\mathbf{k}_\parallel}\hat{b}_{\mathbf{k}_\parallel} + g_0 \sum \left( \hat{a}^\dagger_{\mathbf{k}_\parallel}\hat{b}_{\mathbf{k}_\parallel} + \hat{a}_{\mathbf{k}_\parallel}\hat{b}^\dagger_{\mathbf{k}_\parallel} \right),
\end{aligned}
\tag{1.5}
$$

where $\hat{a}^\dagger_{\mathbf{k}_\parallel}$ and $\hat{b}^\dagger_{\mathbf{k}_\parallel}$ are creation operators for photons and excitons with in-plane momentum $k_\parallel$ and $k_c = \mathbf{k} \cdot \hat{\mathbf{z}}$, is a longitudinal wavenumber determined by the cavity resonance, the $\hat{\mathbf{z}}$ direction is perpendicular to the plane of the mirrors, and $g_0$ is the strength of the interaction between the excitons and the photons. This Hamiltonian may be diagonalised by a transformation of the form

$$
\begin{aligned}
\hat{P}^\dagger_{\mathbf{k}_\parallel} &= X_{\mathbf{k}_\parallel}\hat{b}_{\mathbf{k}_\parallel} + C_{\mathbf{k}_\parallel}\hat{a}_{\mathbf{k}_\parallel}, \\
\hat{Q}^\dagger_{\mathbf{k}_\parallel} &= -C_{\mathbf{k}_\parallel}\hat{b}_{\mathbf{k}_\parallel} + X_{\mathbf{k}_\parallel}\hat{a}_{\mathbf{k}_\parallel},
\end{aligned}
\tag{1.6}
$$

to yield

$$
\hat{H} = \sum E_{\mathrm{LP}}(k_\parallel)\hat{P}^\dagger_{\mathbf{k}_\parallel}\hat{P}_{\mathbf{k}_\parallel} + \sum E_{\mathrm{UP}}(k_\parallel)\hat{Q}^\dagger_{\mathbf{k}_\parallel}\hat{Q}_{\mathbf{k}_\parallel},
\tag{1.7}
$$

---

[1]There are a number of different types of excitons. Experiments in polariton condensation utilise Wannier-Mott excitons, which have low binding energies and a radius larger than the crystal lattice spacing.

from which we can see that $\hat{P}^\dagger_{\mathbf{k}_\parallel}$ and $\hat{Q}^\dagger_{\mathbf{k}_\parallel}$ are creation operators for the new eigenmodes of the system, which are superpositions of photons and excitons, called upper and lower polaritons respectively. Experimental realisations of polariton condensation focus on lower polaritons because they represent the ground state of the system in the strong coupling regime.

The numbers $X_{\mathbf{k}_\parallel}$ and $C_{\mathbf{k}_\parallel}$ are called the Hopfield coefficients [2]. They represent the photonic and excitonic fractions of polaritons, and determine many of the properties of polaritons. Writing the exciton-photon detuning as $\Delta E(k_\parallel) = E_{\text{exc}}(k_\parallel) - E_{\text{cav}}(k_\parallel, k_c)$, the Hopfield coefficients are

$$|X_{\mathbf{k}_\parallel}|^2 = \frac{1}{2}\left(1 + \frac{\Delta E(k_\parallel)}{\sqrt{\Delta E(k_\parallel)^2 + 4g_0^2}}\right),$$

$$|C_{\mathbf{k}_\parallel}|^2 = \frac{1}{2}\left(1 - \frac{\Delta E(k_\parallel)}{\sqrt{\Delta E(k_\parallel)^2 + 4g_0^2}}\right), \tag{1.8}$$

and the polariton energies are

$$E_{\text{LP,UP}}(k_\parallel) = \frac{1}{2}\left(E_{\text{exc}} + E_{\text{cav}} \pm \sqrt{4g_0^2 + (E_{\text{exc}} - E_{\text{cav}})^2}\right). \tag{1.9}$$

For low in-plane momentum, $\hbar^2 k_\parallel^2 / 2m_{\text{cav}} \ll 2g_0$, we can expand Equation (1.9) in $k_\parallel$ to yield

$$E_{\text{LP, UP}}(k_\parallel) \approx E_{\text{LP, UP}}(0) + \frac{\hbar^2 k_\parallel^2}{2m_{\text{LP, UP}}}, \tag{1.10}$$

from which we can see that polaritons are endowed with an effective mass from the in-plane momentum. The effective masses are given by

$$\frac{1}{m_{\text{LP}}} = \frac{|X|^2}{m_{\text{exc}}} + \frac{|C|^2}{m_{\text{cav}}},$$

$$\frac{1}{m_{\text{UP}}} = \frac{|C|^2}{m_{\text{exc}}} + \frac{|X|^2}{m_{\text{cav}}}. \tag{1.11}$$

Since the photon effective mass is much less than the exciton mass, the polariton effective masses are well-approximated as

$$m_{\text{LP}}(k_\parallel \approx 0) \approx \frac{m_{\text{cav}}}{|C|^2},$$

$$m_{\text{UP}}(k_\parallel \approx 0) \approx \frac{m_{\text{cav}}}{|X|^2}. \tag{1.12}$$

Typical values of $m_{\text{LP}}$ range from $10^{-4} m_{\text{e}^-}$, to $10^{-5} m_{\text{e}^-}$, and depend strongly on the detuning. The low effective mass of polaritons is one of a few key properties that make them an attractive platform for bose-einstein condensation [1].

Figure 1.3 shows the Hopfield coefficients and polariton energies as a function of $k_\parallel$ for several different values of the detuning. Note that at high momenta the dispersion

of lower polaritons is effectively flat, reflecting the excitonic component. The effective mass, which is related to the gradient of the dispersion, varies by up to four orders of magnitude depending on the momentum.

Excitons decay radiatively, and photons leak from the microcavity, so exciton-polaritons have a decay rate which is given as

$$\gamma_{\mathrm{LP}} = |X|^2 \gamma_{\mathrm{exc}} + |C|^2 \gamma_{\mathrm{cav}},$$
$$\gamma_{\mathrm{UP}} = |C|^2 \gamma_{\mathrm{exc}} + |X|^2 \gamma_{\mathrm{cav}}. \tag{1.13}$$

Lifetimes, i.e. inverse decay rates as high as $\gamma_{\mathrm{cav}}^{-1} \approx 200\,\mathrm{ps}$ are typical [3]. Because $\gamma_{\mathrm{exc}}^{-1} \approx 1\,\mathrm{ns}$, the lifetime of polaritons is mainly determined by the cavity photon lifetime, and hence the cavity quality factor.

The energy, effective mass, and lifetime of exciton-polaritons all depend on the detuning, which is determined by the energy of the cavity mode, and hence the cavity thickness. Typical microcavity samples are wedge-shaped, i.e. the length of the microcavity varies across the sample. By choosing different positions on the sample, the polariton properties may be varied.

Exciton-polaritons have a pseudospin degree of freedom resulting from the polarisation of the cavity photons. We will neglect this, however many experiments explore spin effects. A detailed review is given in [4].

### 1.1.4   Bose Einstein Condensation of Exciton-Polaritons

Below a critical temperature or above a critical density, dilute bosons gases exhibit significant occupation of the ground state, leading to the appearance of a coherent matter wave, a bose-einstein condensate. A well-known heuristic argument for this phenomenon is that the wavepackets of the particles, whose size is estimated by the de Broglie wavelength, begin to overlap significantly. The thermal de Broglie wavelength is given by

$$\lambda_T = \sqrt{\frac{2\pi\hbar^2}{k_B m T}}, \tag{1.14}$$

where $k_B$ is the Boltzmann constant, $m$ is the particle mass, and $T$ is the temperature. Condensation occurs at a critical temperature where $\lambda_T$ becomes comparable to the mean interparticle distance. Since $\lambda_T$ decreases with $m$, a lower mass results in a lower critical temperature.

Bose-einstein condensation was first observed in dilute gases of alkali atoms [8]. These atoms are relatively heavy, resulting in a low critical temperature, on the order of $1\,\mathrm{nK}$. However laser cooling techniques which rely on the electronic structure of alkali atoms in combination with evaporative cooling in magnetic traps allows these temperatures to be reached. Achieving bose-einstein condensation in alkali atoms requires sophisticated cooling and trapping techniques, and isolation from the environment.

(a)



(b)
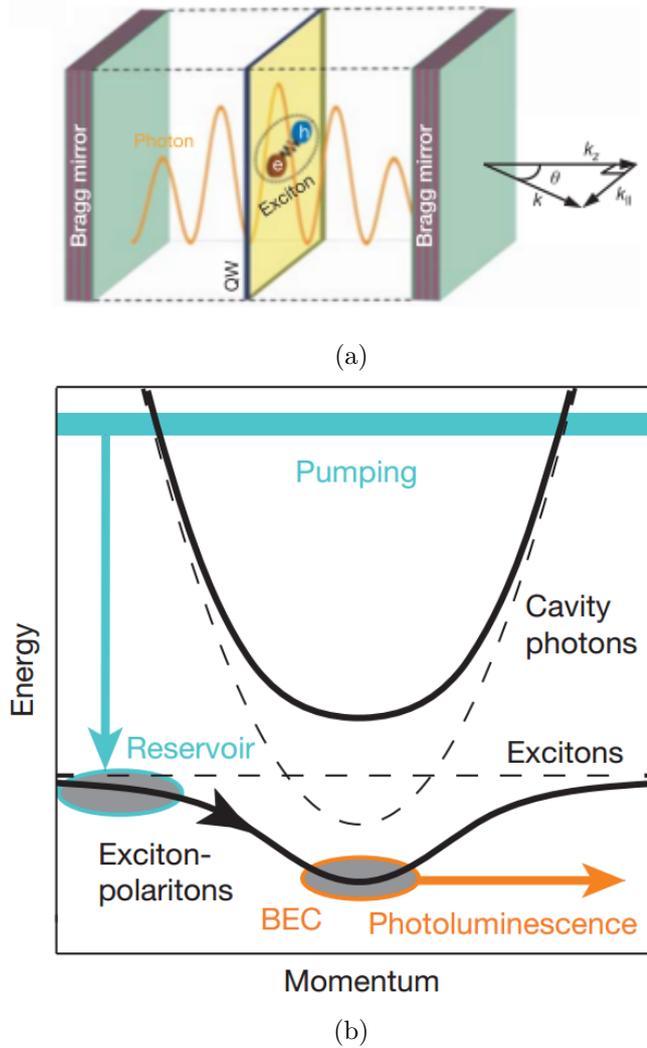
Figure 1.4: Schematics of the microcavity and BEC formation. (a): microcavity formed by two DBRs with a quantum well placed at the antinode of the cavity resonance. Adapted from Ref. [5]. (b): incoherent excitation scheme. Quantum well free carrier states are excited by CW pumping. They relax to the lower polariton branch by various processes. Relaxation continues down the lower polariton branch until a "bottleneck" momentum is reached [6]. At this point, the gradient of the dispersion relation sharply increases, which restricts further relaxation because of the requirement to simultaneously lose a large amount of energy and a small amount of momentum in a collision. A significant population forms at this momentum, constituting a reservoir, some of which condenses by stimulated scattering. Leakage of cavity of photons from decaying excitons allows for measurement of the condensate. Reproduced from Ref. [7].
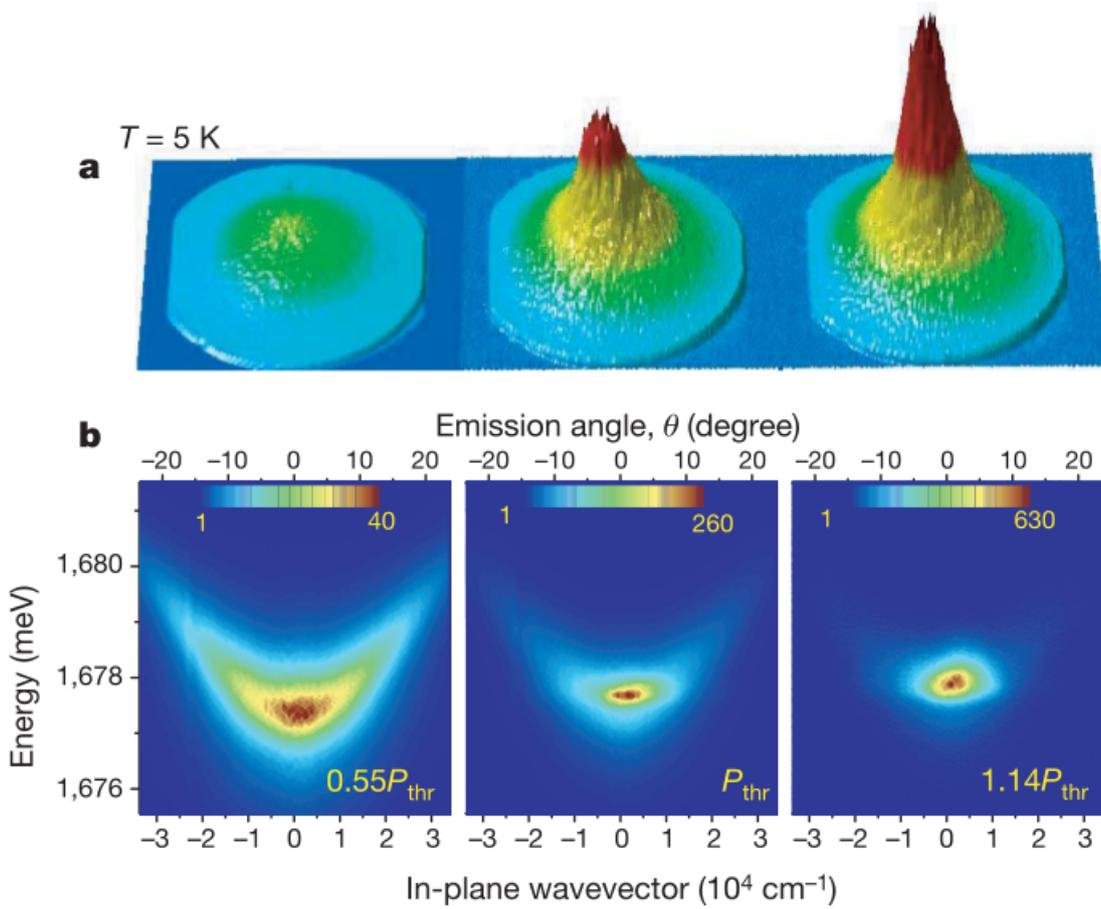
Figure 1.5: Photoluminescence of a system of exciton-polaritons undergoing bose-einstein condensation. (a): near-field emission intensity indicating polariton density, (b): dispersion. Below the threshold power, the emission is widely spread in energy and momentum, roughly reflecting the polariton dispersion. Above threshold, emission is concentrated near $k_\parallel = 0$. Reproduced from Ref. [5].

As exciton-polaritons are composite bosons at low densities, they can also undergo bose-einstein condensation. The effective mass of exciton-polaritons is very low, resulting in a critical temperature much higher than that of alkali atoms. Typical values range from 1 K to room temperature, which can be achieved with simple cryogenic techniques or no cooling at all. Table 1.1 compares the parameters of a few different systems used in BEC research. In contrast to neutral atoms, exciton-polaritons have finite lifetimes, often shorter than the thermalisation time, and exciton-polariton condensates are typically nonequilibrium systems, although cavities with very high Q factors have recently lead to observations of polariton condensates in thermal equilibrium [3]. Furthermore, polariton condensates experience loss and gain so condensation is also a matter of dynamical equilibrium, and polariton condensates are inherently non-Hermitian. In contrast to neutral atoms, where condensation is driven by a decrease in temperature, polariton condensation is driven by density as we outline below in Section 1.2. Some of these issues are discussed in relation to the definition of bose-einstein condensation in Ref. [1, 9].

TABLE I. Parameter comparison of BEC systems.

| Systems | Atomic gases | Excitons | Polaritons |
|---|---|---|---|
| Effective mass $m^*/m_e$ | $10^3$ | $10^{-1}$ | $10^{-5}$ |
| Bohr radius $a_B$ | $10^{-1}$ Å | $10^2$ Å | $10^2$ Å |
| Particle spacing: $n^{-1/d}$ | $10^3$ Å | $10^2$ Å | 1 $\mu$m |
| Critical temperature $T_c$ | 1 nK–1 $\mu$K | 1 mK–1 K | 1–>300 K |
| Thermalization time/Lifetime | 1 ms/1 s$\sim 10^{-3}$ | 10 ps/1 ns$\sim 10^{-2}$ | (1–10 ps)/(1–10 ps)$=0.1$–10 |

Table 1.1: Comparison of parameters for some BEC systems. The larger Bohr radius of polaritons compared to atoms is more than compensated by the extremely low effective mass. As indicated by the last row, thermalisation times are typically shorter than polariton lifetimes, although recent experiments report complete thermalisation using microcavities with very high Q factors [3]. Reproduced from Ref. [1].

Spontaneous bose-einstein condensation of exciton-polaritons requires only non-resonant laser excitation. Free carriers are injected well above the lower polariton energy by the pump laser. They relax down the lower polariton branch due to scattering and interactions with phonons. These processes are greatly suppressed at a certain "bottleneck" momentum, at which the decreasing energy density of states and polariton lifetime result in the accumulation of a significant population, which acts as an incoherent reservoir. Stimulated scattering from the reservoir to $k_\parallel \approx 0$ states results in Bose Einstein condensation around $k_\parallel \approx 0$. This process is illustrated in Figure 1.5. The exact dynamics of this process can be studied using semiclassical Boltzmann rate equations [1], or Keldysh field theory [10, 11]. Resonant excitation can also be used to excite polaritons at a given in-plane momentum by tuning the angle of the pump laser, but we consider only non-resonant excitation.

Polariton condensates are very experimentally accessible. Light leaks from the microcavity, so the condensate density can be inferred from near-field photoluminescence. Conservation of momentum implies that there is a one-to-one correspondence between the polariton momentum and the angle of the emitted light, so angle-resolved measurements

of the cavity photoluminescence characterise the momentum distribution. Spectroscopic measurements of the photoluminescence allow one to measure spatial energy profiles and also the dispersion. Interferometry can also be used to access the phase of the condensate. As explained in Section 1.1.3, wedge-shaped cavities allow one to access a wide range of polariton parameters, ranging from very photonic to very excitonic polaritons.

## 1.2 Mean-Field Models of Exciton-Polariton Condensates

A mean field model for exciton-polariton condensates has not yet been derived from microscopic theory. However, a simple phenomenological model has been successful in describing most experimental phenomena. This model is based on a modification of the Gross-Pitaevskii equation (GPE), which was rigorously derived for atomic condensates, where the total atom number is fixed [12]. It describes the dynamics of the macroscopically populated state.

Mean-field approximations typically allow for analysis of quantum many body systems that would be otherwise intractable. Field operators are replaced with complex numbers representing their expectation value, and equations of motion for these expectation values are derived from the Heisenberg equations of motion for the field operators. Quantum fluctuations are neglected [12].

For atomic BECs, one first replaces the two-body interaction potential with a contact potential. Applying a mean-field approximation then yields the GPE, which describes the order parameter, $\psi$, of the condensate. The GPE reads

$$i\hbar\partial_t\psi(r,t) = \left(-\frac{\hbar^2}{2m}\nabla^2 + V(r) + g|\psi|^2\right)\psi, \tag{1.15}$$

where $m$ is the mass of a boson, $V(r)$ is any external potential $g$ is a measure of the two-body interaction strength. The nonlinearity arises from boson-boson interactions. The GPE is the mainstay of atomic BEC theory in the regime of weak interactions [12].

In contrast to atomic BECs, polariton BECs are inherently open systems. Polaritons experience loss through radiative decay, and gain from stimulated scattering from the reservoir population. They also interact with the reservoir. To account for this, loss, gain, and interaction terms are added to the GPE to yield [13]

$$i\hbar\partial_t\psi(r,t) = \left(-\frac{\hbar^2}{2m_{\mathrm{LP}}}\nabla^2 + V(r) + g_C|\psi|^2 + g_R n_R + \frac{i\hbar}{2}(R[n_R] - \gamma_C)\right)\psi, \tag{1.16}$$

The term $g_R n_R$ accounts for repulsive interactions with the reservoir population, the term $-i\hbar\gamma_C/2$ models polariton loss, and the term $i\hbar R[n_r]/2$ models gain from stimulated scattering from the reservoir, which depends on the reservoir population.

It is then necessary to couple Equation (1.16) to an equation that describes the reservoir

population. Reservoir polaritons are much heavier than polaritons near $k_\parallel \approx 0$, so it is reasonable to assume that the reservoir polaritons do not move relative to the condensate polaritons. A simple rate equation for the reservoir, accounting for loss due to decay and stimulated scattering, and gain from the laser pump therefore suffices. The equation for the reservoir is then

$$\partial_t n_R(r,t) = P(r,t) - \gamma_R n_R - R[n_R]|\psi|^2, \qquad (1.17)$$

where the rate of reservoir injection $P(r,t)$ models gain from the pump laser, and $\gamma_R$ is the radiative loss rate for reservoir polaritons. The gain rate is typically assumed to be proportional to the reservoir population. That is, $R[n_R] = R n_R$, where $R$ is a constant, in both Equations (1.16) and (1.17). Together, Equations (1.16) and (1.17) are called the open dissipative Gross Pitaevskii equation (ODGPE).

A common approximation illuminates the role of the pump laser. If the reservoir timescales are much faster than the condensate timescales, we can adiabatically eliminate the reservoir. Setting $\partial_t n_R = 0$ yields

$$
\begin{aligned}
n_R &= P \left( \gamma_R + R|\psi|^2 \right)^{-1} \\
&\approx \frac{P}{\gamma_R} \left( 1 - \frac{R}{\gamma_R}|\psi|^2 \right),
\end{aligned}
\qquad (1.18)
$$

where we have expanded to the first order in condensate density in the second line. The second term reflects depletion of the reservoir due to stimulated scattering into the condensate. If the condensate density is low, or if $R << \gamma_R$, meaning that stimulated scattering into the condensate is negligible compared to the reservoir loss rate, we can neglect the second term to yield

$$n_R = \frac{P}{\gamma_R}, \qquad (1.19)$$

in which the reservoir population is set only by the pump rate.

Substituting Equation (1.19) in to the ODGPE (Equation (1.16)) yields

$$i\hbar\partial_t\psi(r,t) = \left( -\frac{\hbar^2}{2m}\nabla^2 + g_C|\psi|^2 + \frac{g_R}{\gamma_R}P + \frac{i\hbar}{2}\left( \frac{RP}{\gamma_R} - \gamma_C \right) \right)\psi, \qquad (1.20)$$

which shows that the pump laser induces a real potential, $\frac{g_R}{\gamma_R}P$, and an imaginary potential, $\frac{i\hbar}{2}\frac{RP}{\gamma_R}$, which is a gain term. The real potential arises because of repulsive interactions between the condensate and reservoir, and the imaginary part because stimulated scattering from the reservoir increases the number of condensate polaritons. The relative magnitude of the real and imaginary potentials can in principle be tuned because adjusting the detuning changes both the polariton-reservoir interaction, $g_R$ and in principle stimulated scattering rate, $R$, although the latter is a phenomenological parameter.

It is easy to deduce from the ODGPE, Equations (1.16) and (1.17), that there is a threshold power below which condensation will not occur. Assuming spatially homogeneous pumping and stationary solutions implies that, $\psi(r,t) = e^{-i\mu t}\psi_0$ and $n_R(r,t) = n_R^0$.

For a stationary solution, the condensate must experience zero net gain, so setting $i\hbar(Rn_R^0 - \gamma_C)/2 = 0$ in Equation (1.16) gives an expression for the reservoir density, $n_R^0 = \gamma_C/R$. For a stationary solution we must also have $\partial_t n_R = 0$. From this, and the expression for $n_R^0$, Equation (1.17) implies

$$|\psi_0|^2 = (P - P_{th})/\gamma_C, \tag{1.21}$$

where the homogeneous threshold power is defined as $P_{th} = \gamma_C\gamma_R/R$. From this, we can see that no condensate is present unless $P > P_{th}$. When this condition is met, the pump injects enough reservoir carriers that stimulated scattering from the reservoir into the condensate overcomes the radiative decay of polaritons. This reflects the fact that bose-einstein condensation of exciton-polaritons is driven by increasing excitation density rather that decreasing temperature.

Despite the phenomenological nature of the ODGPE, it has proven successful at describing many experimental phenomena in polariton condensates [7, 14, 15]. In addition, a slightly simplified form has been derived by applying approximations to the optical Maxwell-Bloch equations [16]. Although it is a low-momentum approximation, high momenta can be considered by replacing the kinetic energy term, which is $-\frac{\hbar^2}{2m}\nabla^2$ in the effective mass approximation, with the polariton dispersion. Additional terms may be added to model energy relaxation through interaction with phonons or by other means [17, 18]. Fluctuations arising from scattering from the reservoir may be treated with a truncated Wigner approach [19]. As an alternative to the mean field theory, Lindblad equations for the evolution of the condensate density matrix have also been derived [20].

## 1.3   Creating Potentials for Exciton-Polaritons

Engineering potentials for polaritons allows for condensation in traps, which has led to observation of a range of experimental phenomena, including robust switching between quantum states [15, 21], and encircling of an exceptional point [7, 22]. Many techniques have been developed [23], so we focus only on a few which are relevant to our work.

Polaritons can be trapped by inducing confinement for either the excitonic or photonic part of the wavefunction. Confining the photonic component of the wavefunction is most easily achieved by etching away parts of the cavity, for example using electron beam lithography. Lateral confinement of photons due to the difference in refractive indices at the semiconductor interface then introduces a strong potential for polaritons [24]. The maturity of lithographic techniques means that complicated structures such as lattices of coupled micropillars can be created [25]. However, etching down to the substrate leads to significant polariton loss because of surface effects [23].

An alternative approach is to induce a weaker potential by inducing only a small elongation to a part of the cavity. This is achieved with an etch-and-overgrowth technique, whereby the bottom DBR, quantum well, and spacer are first manufactured. After this, parts of the spacer layer are etched away, leaving a small local elongation. The upper DBR is then grown on top of this structure. The cavity is therefore slightly elongated in

the region where the spacer layer was not etched away [23, 26]. Such a structure is shown in Figure 1.6. Locally elongating the microcavity lowers the energy of cavity modes, and hence the energy of lower polaritons, thereby creating a trapping potential for lower polaritons. For ideal DBRs which are tuned to the spacer frequency, a length change of $\Delta L$ causes an approximate shift of $\Delta\omega_C = -\omega_m \Delta L / L_C$ in the resonant frequency of the cavity, where $\omega_m$ is the resonant frequency of the spacer and $L_C$ is the unaltered length of the cavity [27]. For typical cavities an elongation on the order of nanometres causes an energy shift on the order of millielectronvolts [26, 27]. Equation (1.9) shows that the shift in lower polariton energy is approximately proportional to the shift in the cavity mode energy. This technique allows for the creation of precisely shaped potentials with a depth that can be chosen during fabrication, but which cannot be adjusted thereafter. It is also worth mentioning that the difference in the detuning inside the elongated region means that the effective mass and other polariton parameters differ inside the trap. Using this technique, polariton condensation has been observed in both isolated traps [26] and periodic lattices [28].

Another well-developed technique is optical trapping. The optical pump induces a repulsive potential for polaritons due to two-body interactions with the reservoir population, which is largely bound to the pump location. Such potentials are typically on the order of several meV, which is sufficient to trap polaritons [29]. The great advantage of this technique is that the trap shape, and to some extent the depth, can be manipulated by reshaping the laser and adjusting its power. Spatial manipulation of the pump laser can be accomplished with spatial light modulators. One limitation is that the potential is altered by depletion of the reservoir due to stimulated scattering at high polariton densities [30]. In addition, the laser pump induces an imaginary potential as well as a real one, since stimulated scattering in to the condensate from the reservoir is a source of gain. Therefore the pump-dependent potential is unavoidably non-Hermitian. Although this could be seen as a limitation, it has in fact been exploited in several experiments. The gain of a trapped state is primarily set by its overlap with the pump region, which can be tuned by changing the width of the pump region while keeping the trap depth and size of the interior constant. On the other hand, the energy of a trapped state can be tuned by either increasing the trap depth, or decreasing the trap size, while keeping the width of the pump region constant. This interplay between the real and imaginary pump-dependent potential has been used to induce stable switching between trapped states [15, 21], and also to steer trapped states to an exceptional point (see Section 1.4.2) [7, 22]. The real and imaginary parts of the pump dependent potential are apparent immediately in the ODGPE, Equation (1.20), once the reservoir is eliminated. It is worth mentioning that both terms have different prefactors that depend on the polariton parameters, and hence the detuning. So the relative magnitude of the real and imaginary parts depends on the detuning.
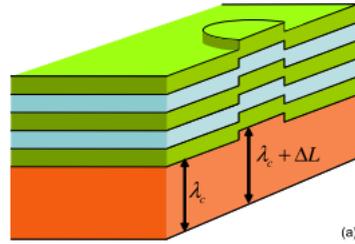
Figure 1.6: Schematic of a locally elongated microcavity fabricated using an etch-and-overgrowth technique. The energy of the optical mode is lower in the elongated region, resulting in a confining potential for exciton-polaritons. Reproduced from Ref. [27].

## 1.4 Non-Hermitian Systems and PT-Symmetric Quantum Mechanics

### 1.4.1 PT Symmetric Quantum Mechanics

Hermiticity of the Hamiltonian is often viewed as a fundamental axiom of quantum mechanics since it ensures not only that energies are real, but that time evolution is unitary. However, Hermiticity is a sufficient but not necessary condition for this to occur. Based first on numerical observations of non-Hermitian Hamiltonians that have entirely real spectra, and later theoretical work, theories of non-Hermitian quantum mechanics have been developed [31–34]. Although non-Hermitian Hamiltonians had been considered before, for example to describe radioactive decay or resonances with nonzero linewidth, it was tacitly assumed that loss and gain would have only small effects. In fact, non-Hermiticity gives rise to a range of novel behaviours.

Chief among the theories developed is PT-symmetric quantum mechanics. The genesis of this work was the observation and later proof that the spectrum of the non-Hermitian Hamiltonian

$$\hat{H} = \hat{p}^2 + i\hat{x}^3 \tag{1.22}$$

is entirely real [35]. The reason for this remarkable fact is that despite being non-Hermitian, the Hamiltonian (1.22) possesses a more subtle symmetry. It is unchanged by simultaneous spatial inversion and time reversal. The spatial inversion operator, $\hat{P}$ is defined by its action on a wavefunction:

$$\hat{P}\psi(x,t) = \psi(-x,t), \tag{1.23}$$

as is the time reversal operator, $\hat{T}$:

$$\hat{T}\psi(x,t) = \psi^*(x,-t). \tag{1.24}$$

The complex conjugate appears because the $T$ operator is antilinear. Since the Hamiltonian (1.22) is unchanged when both these operations are applied simultaneously, it is called PT symmetric. Generally, a PT symmetric Hamiltonian is defined to be one which commutes with the $\hat{P}\hat{T}$ operator. For Hamiltonians without explicit time-dependence,

time reversal simply corresponds to complex conjugation.

However, PT symmetry of the Hamiltonian is not sufficient to ensure real energies. It only implies that energies occur in complex conjugate pairs, which can be seen by applying the $\hat{P}\hat{T}$ operator to both sides of the eigenvalue equation

$$\hat{H}\psi = E\psi, \tag{1.25}$$

which yields

$$\hat{H}(\hat{P}\hat{T}\psi) = E^*\hat{P}\hat{T}\psi, \tag{1.26}$$

noting that the Hamiltonian commutes with the $\hat{P}\hat{T}$ operator, and $\hat{P}$ is linear but $\hat{T}$ is antilinear. This means that if $\psi$ is an eigenstate with eigenvalue $E$, then $\hat{P}\hat{T}\psi$ is also an eigenstate with eigenvalue $E^*$. In fact, the necessary and sufficient condition for the energies to be real is that the eigenstates are also PT symmetric. The essential reason for this condition can be seen by again applying the $\hat{P}\hat{T}$ operator the eigenvalue equation (1.25). The left hand side is equal to $\hat{P}\hat{T}\hat{H}\psi$, which is simply equal to $\hat{H}\psi$ if *both* the Hamiltonian and eigenfunction are PT symmetric. If the eigenfunction is PT symmetric, the right hand side, $\hat{P}\hat{T}E\psi$ simplifies to $E^*\psi$, and we can therefore conclude $E\psi = E^*\psi$, so the energy is real. The other direction is similar but the proof is not simple if degeneracy of the eigenstates is considered [36]. The extra condition is required simply because $\hat{T}$ and hence $\hat{P}\hat{T}$ is antilinear. If the $\hat{P}\hat{T}$ operator were linear, eigenstates of $\hat{H}$ would also be eigenstates of the $\hat{P}\hat{T}$ operator, since the two commute.

In practice, most PT symmetric systems exhibit two phases, one in which the eigenstates are also PT symmetric, and the energies are real, and a second in which some of the eigenstates are not PT symmetric, and the corresponding eigenvalues are complex. Typically, this transition is controlled by a parameter that essentially measures the non-Hermiticity of the system [36, 37]. For example, the PT symmetric Hamiltonian (1.22) can be generalised as

$$\hat{H} = \hat{p}^2 + \hat{x}^2(i\hat{x})^\delta, \tag{1.27}$$

where the real parameter $\delta$ essentially measures the strength of the non-Hermitian part. The spectrum is entirely real when and positive when $\delta \geq 0$. When $-1 < \delta < 0$, some eigenvalues are real and others are complex, and when $\delta < -1$, there are no real eigenvalues. In the PT asymmetric phase, the eigenstates spontaneously break the PT symmetry of the Hamiltonian. The symmetry breaking transition is associated with an exceptional point [31], a non-Hermitian degeneracy where eigenstates as well as eigenvalues coincide [38] (see Section 1.4.2).

An more enlightening demonstration is given in the behaviour the two-level model with a Hamiltonian

$$\hat{H}(\gamma) = \begin{pmatrix} \omega + i\gamma & \delta \\ \delta & \omega - i\gamma \end{pmatrix}, \tag{1.28}$$

where all the parameters are real. This represents two coupled energy levels, one which

experiences gain and the other loss. The parity operator is given by

$$\hat{P} = \begin{pmatrix} 0 & 1 \\ 1 & 0 \end{pmatrix}, \tag{1.29}$$

which swaps the levels, and the time reversal operator, $\hat{T}$ simply corresponds to complex conjugation. It is easy to verify that the Hamiltonian (1.28) commutes with the $\hat{P}\hat{T}$ operator. This amounts to stating that exchanging the levels and interchanging loss and gain leaves the system unchanged. The imaginary part of the diagonal elements, $\gamma$, quantifies the degree of non-Hermiticity. The energies are

$$E^{\pm} = \omega \pm \sqrt{\delta^2 - \gamma^2} \tag{1.30}$$

and the eigenstates are

$$\psi^{\pm} = \begin{pmatrix} \frac{i\gamma \pm \sqrt{\delta^- \gamma^2}}{\delta} \\ 1 \end{pmatrix}. \tag{1.31}$$

From (1.30), the eigenvalues are real when $|\gamma| < |\delta|$. To confirm that the system is in the PT symmetric phase, we have to also verify that the eigenstates are PT symmetric. To this end, note that for $|\gamma| < |\delta|$, the quantity $\sqrt{\delta^2 - \gamma^2}$ is real and hence the first entry of each of the eigenvectors (1.31) is a complex number with unit modulus. We can therefore write

$$\psi^+ = \begin{pmatrix} e^{i\alpha} \\ 1 \end{pmatrix}, \tag{1.32}$$

where $\alpha$ is real. This can be rescaled to

$$\tilde{\psi}^+ = \begin{pmatrix} e^{i\alpha/2} \\ e^{-i\alpha/2} \end{pmatrix}, \tag{1.33}$$

which is clearly an eigenstate of the $\hat{P}\hat{T}$ operator with eigenvalue 1. The same argument applies to $\psi^-$. However, when $|\gamma| > |\delta|$, the first entry of each of the eigenstates (1.31) is purely imaginary, so we can rewrite

$$\psi^+ = \begin{pmatrix} iA \\ 1 \end{pmatrix}, \tag{1.34}$$

where $A$ is real. Applying the $\hat{P}\hat{T}$ operator yields

$$PT\psi^+ = \begin{pmatrix} 1 \\ -iA \end{pmatrix}, \tag{1.35}$$

from which it is clear that $\psi^+$ is in general not an eigenstate of the $\hat{P}\hat{T}$ operator[2]. An identical argument holds for $\psi^-$. When $|\gamma| = |\delta|$, the eigenvalues are both $E^{\pm} = \omega$, and the eigenstates are both $\psi^{\pm} = (i\gamma/\delta, 1)^T$. To summarise, when $|\gamma| < |\delta|$, the system is in the PT symmetric phase - the eigenstates are PT symmetric and the eigenvalues are real. When $|\gamma| > |\delta|$, the system is in the broken symmetry phase - the eigenvalues are complex conjugates and the eigenstates are not PT symmetric. The transition between these two regions, $|\gamma| = |\delta|$ corresponds to an exceptional point - both the

---

[2]It is easy to see that $\hat{P}\hat{T}\psi^+$ can only be an eigenstate of the $\hat{P}\hat{T}$ operator if $A^2 = 1$. Since $A = (\gamma + \sqrt{\delta^2 - \gamma^2})/\delta$, this corresponds only to the symmetry breaking transition, $|\gamma| = |\delta|$.

eigenvalues and eigenstates coincide[3]. Note also that in the PT symmetric phase each of the eigenstates are equally-weighted linear combinations of a mode localised in the gain region and one localised in the loss region, which explains why the eigenvalues remain real. In the broken PT symmetry phase, the weights become unequal - for large $\gamma$, the quantity $A$ in Equation (1.35) is also large, and $\psi^+$ consists mostly of the active mode.

Most realisations of PT symmetric systems use loss and gain to create potentials that are PT symmetric. The Hamiltonian of a particle moving in a potential $\hat{V}(x)$ is given by

$$\hat{H} = \frac{\hat{p}^2}{2m} + \hat{V}(x). \tag{1.36}$$

Since the first term is PT symmetric[4], this Hamiltonian is PT symmetric when

$$\operatorname{Re} V(x) = \operatorname{Re} V(-x)$$
$$\operatorname{Im} V(x) = -\operatorname{Im} V(-x). \tag{1.37}$$

That is, that the real part of the potential is symmetric and the imaginary part is antisymmetric.

In the unbroken PT symmetry phase, energies are real so it is natural to ask whether the other features of conventional quantum mechanics can be recovered. Aside from real energies, these important features include unitary time evolution (in the sense that the norm of a state is preserved in time), orthogonality of eigenstates of the Hamiltonian, and completeness, in the sense that an arbitrary state can be expressed as a linear combination of eigenstates of the Hamiltonian. It turns out that many of these features can be recovered through a redefinition of the inner product [31, 32, 39], which yields a new type of quantum mechanics. Since time evolution is still generated by the Hamiltonian, a reasonable choice of inner product would be the PT inner product, defined by $\langle \psi | \phi \rangle^{PT} = \left\langle \hat{P}\hat{T}\psi \middle| \phi \right\rangle$. Because the Hamiltonian commutes with the $\hat{P}\hat{T}$ operator, the norm defined by this inner product is conserved by time evolution. However, this norm is not necessarily positive-definite. In fact, even after a normalisation, the PT norm of an eigenstate[5] is either 1 or -1. This problem is solved by the introduction of another operator, $\hat{C}$, to define a CPT inner product as $\langle \psi | \phi \rangle^{CPT} = \left\langle \hat{C}\hat{P}\hat{T}\psi \middle| \phi \right\rangle$. The operator $\hat{C}$ essentially measures the sign of the PT norm of an eigenstate, which ensures that the corresponding norm is positive definite since it contributes a factor of -1 to states with a negative PT norm. It also commutes with both the Hamiltonian and the $\hat{P}\hat{T}$ operator, which ensures unitary time evolution. This operator can be expressed in terms of the eigenstates of the Hamiltonian, which means it is in principle possible to calculate. Also, in the Hermitian limit, it reduces to the parity operator, $\hat{P}$. Since $\hat{P}^2 = 1$ and the $\hat{T}$ operator is antilinear, this means that the CPT inner product reduces to the conventional inner product of Hermitian quantum mechanics.

---

[3]There is an apparent re-entrant behaviour in that the PT symmetric phase corresponds to $-\gamma < |\delta| < \gamma$, but this is simply because a negative loss represents a gain and vice versa.

[4]Both the $\hat{P}$ and $\hat{T}$ operator take the momentum, $p$, to $-p$.

[5]In the PT symmetric phase, the eigenstates of the Hamiltonian are also eigenstates of the $\hat{P}\hat{T}$ operator. Since the PT eigenvalue of each of these eigenvectors is a pure phase, they can be normalised so that their PT eigenvalue is 1 without changing their energy.

Despite the simplicity of this theory, there remain a number of open problems and interesting features. Conventional quantum mechanics has many other features aside from those restored by the redefinition of the inner product, such as semiclassical limits, perturbation theory and so on [40]. There are even questions around the redefined inner product of PT symmetric quantum mechanics. For example, the statement of completeness for the PT normalised eigenstates has only been verified numerically for a few PT symmetric potentials [39, 41]. Although the definition of the $\hat{C}$ operator is simple, calculating it can be very involved. For example, even in such a simple system as a PT symmetric square well (see Chapter 2), a lengthy calculation yields only the first few terms of a perturbative expansion for $\hat{C}$ [42, 43]. Finally, the observables in PT symmetric quantum mechanics are different to those in conventional quantum mechanics. In conventional quantum mechanics, Hermiticity of an observable ensures that the expectation value of that observable remains real under time evolution. In PT symmetric quantum mechanics the equivalent condition is

$$\hat{A}^T = \hat{C}\hat{P}\hat{T} \; \hat{A} \; \hat{C}\hat{P}\hat{T}, \tag{1.38}$$

where $\hat{A}$ is the observable. Under this condition, position and momentum are no longer observables [39].

Finally, PT symmetric quantum mechanics is related to the wider field of pseudo-Hermitian quantum mechanics. An operator, $\hat{H}$, is pseudo-Hermitian if there exists a linear Hermitian operator, $\hat{\eta}$, such that

$$\hat{H}^\dagger = \hat{\eta}\hat{H}\hat{\eta}^{-1}. \tag{1.39}$$

Pseudo-Hermitian quantum mechanics encompasses both conventional and PT symmetric quantum mechanics [33, 40]. In pseudo-Hermitian quantum mechanics, conditions for the reality of eigenvalues can be found that are weaker than those for PT symmetry.

### 1.4.2   Exceptional Points in Non-Hermitian Systems

It is known that the eigenvalues of a parameter-dependent Hermitian Hamiltonian can exhibit degeneracies - at certain parameter values, eigenvalues become equal. For Hermitian Hamiltonians, the corresponding eigenstates remain distinct despite the degeneracy in eigenvalues. Such a degeneracy is often called a diabolical point (DP) because of its shape in energy-parameter space. However, non-Hermitian Hamiltonians exhibit different type of degeneracy where the eigenstates as well as the eigenvalues become degenerate. Such a non-Hermitian degeneracy is often called an exceptional point (EP) [38, 44]. EPs have a number of interesting properties not associated with diabolical points, most of which are a consequence of the characteristic complex square root behaviour of eigenvalues near an EP. Non-Hermiticity is most often found in open systems that exhibit loss and gain [37, 45]. Examples include optical and microwave resonators [46, 47], electrical circuits [48], and polariton condensates [7, 22]. In such systems, the unique properties of EPs have physical consequences [38]. Exceptional points occur at the PT-symmetry breaking transition in PT symmetric systems [49], and are also associated with quantum phase transitions [50].
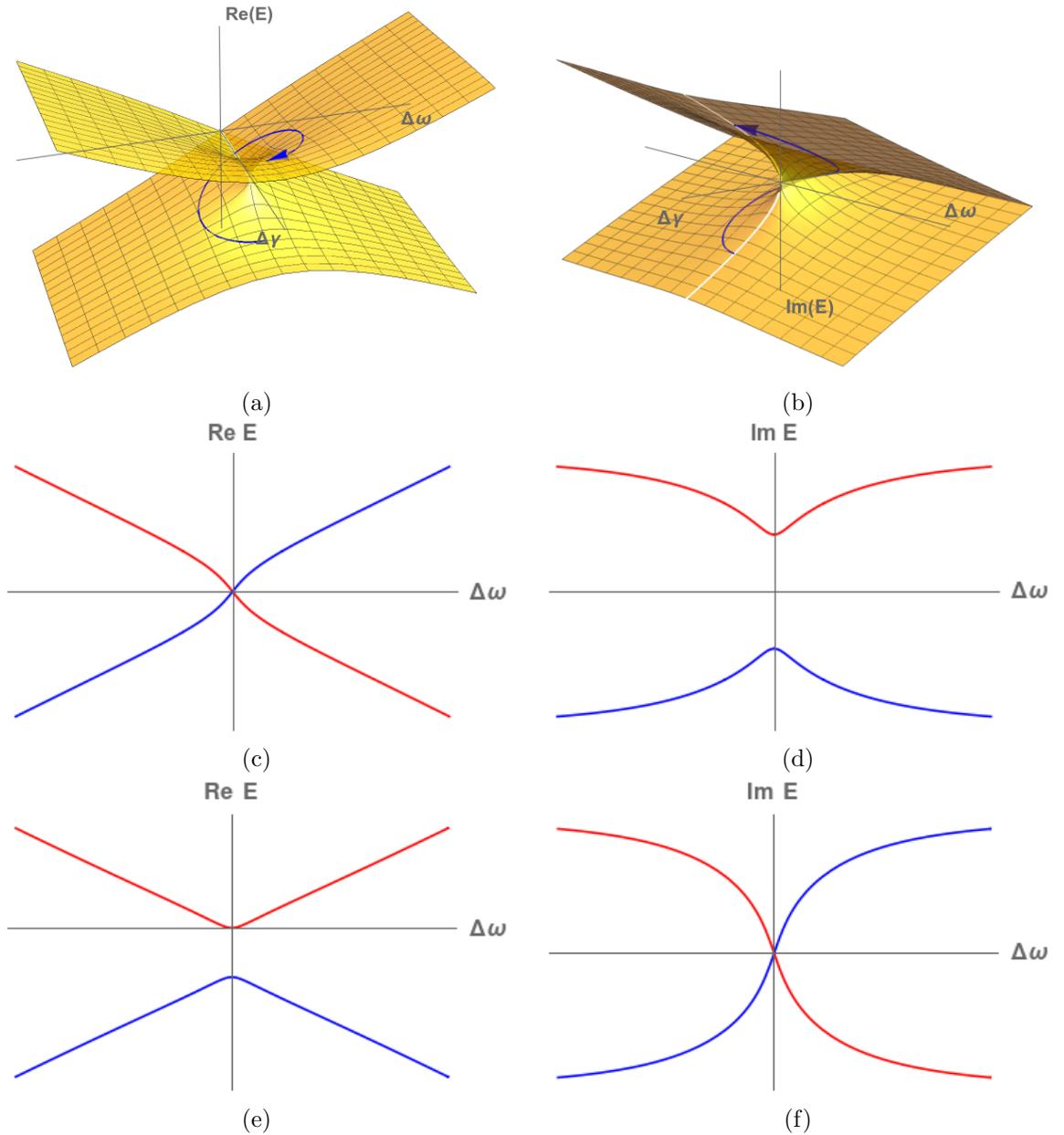
Figure 1.7: Topological structure of an exceptional point. The Riemann sheets associated with the real (a), and imaginary (b) parts of the eigenvalues of the eigenstates that coalesce at the EP. The blue curves illustrate the trajectory of the system when the EP is encircled, clearly showing why a single encircling of the EP switches the states. However, the geometric phase cannot be inferred from these graphs. The characteristic change from crossing to anticrossing of the real and imaginary parts of the eigenvalues near an EP is illustrated in (c)-(f). In each graph we slice along the $\Delta\omega$ axis. In (c) and (d), the real and imaginary parts of the eigenvalues are shown for a slice taken at a value of $\Delta\gamma$ smaller than the value for the EP. In (e) and (d), the same are show for a slice at a value of $\Delta\gamma$ larger than the value for the EP. Two things are clear: crossing of the real parts is associated with anticrossing of the imaginary parts, and the crossing-anticrossing behaviour is reversed for slices on either side of the EP. This change from crossing to anticrossing is an important experimental signature of an EP. Equation (1.41) shows that EPs come in pairs. We show only one here for clarity - the structure is symmetric in the $\Delta\omega$ axis and we have omitted the negative region.

We will consider EPs in which two eigenstates coalesce. EPs of arbitrarily high order are also possible, but the topological structure becomes more complex [38]. When only two eigenvectors coalesce, the full problem can be reduced, and the EP can be described by the simple two-level Hamiltonian [38, 51]

$$\hat{H}(\lambda) = \begin{pmatrix} \omega_1 & 0 \\ 0 & \omega_2 \end{pmatrix} + \lambda \begin{pmatrix} \epsilon_1 & \delta_1 \\ \delta_2 & \epsilon_2 \end{pmatrix}, \tag{1.40}$$

where the non-interacting energies are $E_k = w_k + \lambda \epsilon_k$, the couplings are given by $\delta_k$, and $\lambda$ is a complex parameter. The eigenvalues coalesce at two values of $\lambda$ given by

$$\lambda_{1,2} = \frac{-i(\omega_1 - \omega_2)}{i(\epsilon_1 - \epsilon_2) \pm 2\sqrt{\delta_1 \delta_2}}. \tag{1.41}$$

Near the EP the eigenvalues depend on $\lambda$ as

$$E_{1,2}(\lambda) = \frac{1}{2}\left(\omega_1 + \omega_2 + \lambda(\epsilon_1 + \epsilon_2) \pm \sqrt{(\epsilon_1 - \epsilon_2) + 4\delta_1\delta_2}\sqrt{(\lambda - \lambda_1)(\lambda - \lambda_2)}\right). \tag{1.42}$$

At each EP, there is only one eigenvector,

$$|\phi_{1,2}\rangle = \begin{pmatrix} \pm\frac{i\delta_1}{\sqrt{\delta_1\delta_2}} \\ 1 \end{pmatrix}. \tag{1.43}$$

Equation (1.42) shows that the EP is a stable phenomenon - changing the entries of the matrices in Equation (1.40) shifts the EP but does not remove it. Although Equation (1.40) generically describes all EPs where two states coalesce [52], it is not always clear how to derive a two-level model, for example, for the EP associated with PT-symmetry breaking in the PT symmetric square well (see Chapter 2).

If the underlying Hamiltonians are Hermitian, then $\omega_i$ and $\epsilon_i$ are real, and $\delta_2 = \delta_1^*$, so according to Equation (1.42), an EP is achieved for complex values of $\lambda$ (so long as $\delta_1 \neq 0$). Generally, to reach and encircle an EP, two parameters, for example $\operatorname{Re}\lambda$ and $\operatorname{Im}\lambda$, must be varied. Also, since $\lambda$ must be complex, the overall system is non-Hermitian even if the underlying matrices are Hermitian. The situation is a little simpler for PT-symmetric systems. For PT symmetry, the parity operation is swapping the underlying states in Equation (1.40), and time reversal corresponds to replacing $i$ with $-i$. So PT symmetry is achieved when $\omega_2 = \omega_1^*$, $\epsilon_2 = \epsilon_1^*$, and $\delta_2 = \delta_1$, which must also be real. Under these conditions, an EP is attained for real values of $\lambda$. This is easily illustrated with the simple Hamiltonian

$$H = \begin{pmatrix} \omega + i\gamma & \delta \\ \delta & \omega - i\gamma \end{pmatrix}, \tag{1.44}$$

which models a pair of interacting states that experience balanced loss and gain. The eigenvalues are given by

$$E_{1,2} = \omega \pm \sqrt{\delta^2 - \gamma^2}. \tag{1.45}$$

An EP occurs when $|\delta| = |\gamma|$, which can be reached by varying only one parameter, either the coupling, $\delta$ or the loss, $\gamma$. In practice, $\gamma$ is often kept constant and $\delta$ is varied [53, 54]. Here, the EP corresponds exactly to the PT-symmetry breaking transition. When $|\delta| < |\gamma|$, the energies are real, and when $|\delta| > |\gamma|$, they are complex conjugates.

The energies approach each other along the real axis and then diverge as a complex conjugate pair, as shown in Figure 1.8. This behaviour has been harnessed for mode selection and switching applications. Before the EP, neither mode experiences loss, but after the EP, one experiences gain and the other loss, and the lossy mode is suppressed [54–56].



(a)                                                      (b)
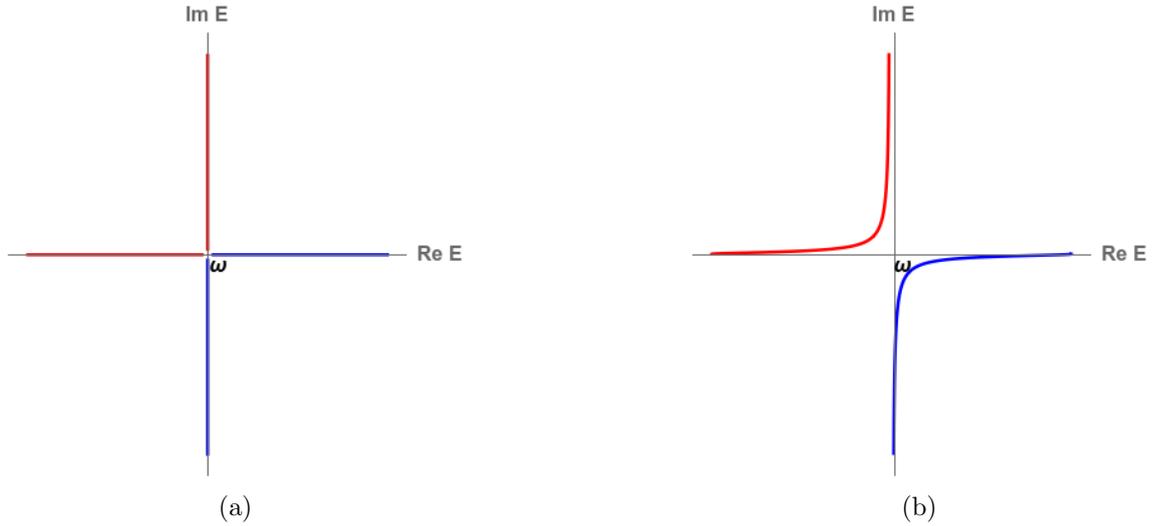
Figure 1.8: Behaviour of the eigenvalues near an EP associated with PT symmetry, as described by Equations (1.44), (1.45). As shown in (a), when the coupling $\delta$ is varied, the eigenvalues approach each other along the real axis, and split in to a complex conjugate pair at the EP, which is typical for the PT symmetry breaking transition. The effect of a small detuning between the eigenstates is illustrated in (b). The eigenvalues no longer cross. This characteristic avoided crossing behaviour can be used for switching or mode selection in experiments since one eigenstate experiences gain and the other loss.

There are a few interesting features of EPs that have physical consequences. Equation (1.42) shows that near an EP, the eigenvalues have a square root dependence on the parameter $\lambda$. For small values of $\lambda$, the derivative, $dE/d\lambda$ is therefore large, and this sensitivity can be exploited for switching [55, 57, 58], or to enhance the sensitivity of sensors [59–62]. Away from the EP, there are two linearly independent eigenvectors, and when the EP is encircled in parameter space (for example, by varying the real and imaginary parts of $\lambda$), the eigenvectors are interchanged with a sign change that is a result of a topological phase. This behaviour is a result of the complex square root structure near the EP, as illustrated in Figure 1.7. If the EP is encircled a second time, the eigenstates are interchanged again, but the sign change remains. Only after four encirclings are the eigenvectors restored. For clockwise encircling, the pattern is $|\psi_1\rangle \to -|\psi_2\rangle \to -|\psi_1\rangle \to |\psi_2\rangle \to |\psi_1\rangle$ [51, 63, 64]. This implies a chirality in that counterclockwise encircling produces a different pattern. The eigenstate at the EP, given is Equation (1.43) is also chiral [63, 65]. When $\delta_1 = \delta_2$, the eigenstate at one of the two EPs is given by

$$|\phi\rangle = \begin{pmatrix} \pm i \\ 1 \end{pmatrix}, \tag{1.46}$$

regardless of the choice of basis. In the context of quantum mechanics and optics, the basis states oscillate in time, so Equation (1.46) represents a superposition of basis

states with a phase difference of $\pi/2$. The oscillation of the first state trails or leads (depending on the sign) that of the second state by a quarter period. This phase lag leads to circular rotation with a well-defined direction - either clockwise or counterclockwise, that is, chirality [65]. An analogy in optics is the formation of circular polarisation by superposition of linearly polarised light.

The chirality of EPs is often manifested in experiments, for example in optical whispering gallery mode resonators where the eigenstate at the exceptional point is a travelling wave in either the clockwise or counterclockwise direction [66–68], in coupled resonators where intensity is localised in a single resonator [54, 69], and in optics unidirectional propagation has been demonstrated [53, 70, 71]. The interchange of modes when an exceptional point is encircled has been observed in many systems, including microwave resonators [46, 72] and polariton condensates [7, 22]. This topological behaviour has also been harnessed in an experiment with microwave waveguides, where carefully chosen modifications to the waveguide boundary steer the waveguide mode around an EP as it propagates. A combination of adiabatic transport on the Riemann sheets and a nonadiabatic jump from one sheet to the other [73] means that the system ends up in the same state after encircling regardless of the initial state, which allows for asymmetric switching between waveguide modes [74]. Dynamic encircling of an EP has also been studied in optomechanical systems [75] and atomic spectra [76].

Finally, the nontrivial square root structure near the EP can cause apparently counterintuitive effects such as the pump-induced suppression and then revival of lasing in coupled microresonators [77, 78]. This structure also leads to a characteristic crossing-anticrossing behaviour of the real and imaginary parts of the eigenvalues. For example, if one takes a slice along the $\mathrm{Re}\,\lambda$ axis near the EP in Figure 1.7, the real parts of the eigenvalues will cross, and the imaginary parts exhibit anticrossing. If a slice is taken on the other side of the EP, the behaviour is reversed - the real parts exhibit anticrossing, and the imaginary parts cross. It has been shown that crossing of the real parts is associated with anticrossing of the imaginary parts [51, 52, 79]. The change from crossing to anticrossing is an important experimental signature of an EP [7, 46] since the nonzero linewidth of states means it is generally not possible to resolve the EP in an experiment.

### 1.4.3 Physical Realisations of Non-Hermitian Systems and Exceptional Points

These results on non-Hermitian degeneracies and PT symmetric systems have inspired a wide range of experiments [36, 37]. Most experiments introduce non-Hermiticity through loss and gain, or by engineering a coupling between two states. By tuning the system to an exceptional point, many remarkable behaviours can be demonstrated. Since there are no known examples of a closed non-Hermitian quantum system, experiments inspired by PT symmetric quantum mechanics focus on classical wave systems where an analogy can be made with the Schrodinger equation. Despite the deeper theoretical results in PT symmetric quantum mechanics, most experiments focus on observing the PT symmetry breaking and phenomena related to the associated EP.

EPs have been predicted or observed in a range of systems. Some examples include electrical circuits [48], microwave resonators [72], optical resonators [53, 61], exciton-polaritons [7, 22], the optical spectra of atoms [76, 80], and also quantum phase transitions [50]. Optical systems have been a fruitful ground for phenomena associated with EPs since loss is unavoidable, and gain can be achieved with doping and optical pumping. Also, the field of optical microresonators is well-developed [81], and modes of these resonators can be coupled with only small perturbations to achieve an EP [82]. Some of the interesting phenomena associated with EPs in optical systems include loss-induced transparency [83], reversing the pump dependence of lasers [78], and enhanced sensing [53, 60, 61]. In polariton condensates, the non-Hermiticity of optical potentials, explained in Section 1.2 has been used to induce EPs. Changing the strength of the optical pump changes primarily the real part of mode energies whereas changing the area of the optical pump changes the imaginary part of a mode energy by modifying the gain of that mode, which is mostly determined by overlap with the optical potential.

The analogy between the Helmholtz equation and the Schrodinger equation allows for the creation of optical systems that are analogues of PT symmetric quantum systems [36]. The complex permittivity takes the place of the potential, and PT symmetry may be achieved with gain provided by optical pumping [78], or passively with a suitably designed asymmetric loss profile. In the latter case PT symmetry is not achieved, but a transformation allows one to recast the system in terms of a PT symmetric one [36, 83]. Most work focuses only on the EP that accompanies the PT symmetry breaking transition, and this has allowed for the demonstration of a number of interesting effects including loss-induced transparency [83], refraction asymmetry [84], and thresholdless single mode lasing [54, 56]. There are, however, significant limitations to the analogy - because the refractive index depends on frequency, PT symmetry can be attained only for a discrete set of frequencies rather than a frequency range, which makes observation of the PT symmetry breaking transition subtle and involved. It has also been argued that many of the effects observed in PT symmetric optical systems are not uniquely a result of PT symmetry [36].

One of the simplest means of achieving PT symmetry is through the introduction of gain and loss. At a microscopic level, gain and loss are manifested in open quantum systems by stochastic evolution [85]. However, the same gain and loss are represented by an imaginary potential in the semiclassical limit. In addition, the order parameter of such systems often obeys a Schrodinger-type equation, allowing for an analogue of a PT symmetric quantum system to be studied. The analogy is stronger than for optical systems both because these systems are inherently quantum, and because PT symmetry can truly be achieved. For example, the order parameter of both atomic BECs and BECs of exciton-polaritons is described by a Gross-Pitaevskii equation, which is a nonlinear Schrodinger equation. Since these systems are also nonlinear due to two-body interactions, results from PT symmetric quantum theory do not apply exactly, but this also means that they are a natural testing ground to explore the interplay of nonlinearity and PT symmetry [86]. Gain and loss are naturally present in polariton condensates because of leakage of photons from the cavity and stimulated scattering from the reservoir to the condensate as explained in Section 1.2. In contrast, gain and loss must be carefully induced in atomic condensates [37]. For example, loss can be engineered with electron

beams from scanning electron microscopes that knock atoms out of the condensate [87], and gain can be introduced via a condensate replenishing mechanism similar to that used in an atomic laser [88]. So far, such induced non-Hermiticity has been used in atomic BECs to achieve coherent perfect absorption [89], negative differential conductivity [87], bistability [90] and other effects [91]. In addition, PT symmetric atomic BECs have been explored theoretically. There are proposals for PT symmetric coupled double wells [92–95] and also multiwell potentials [96]. It has been shown that the nonlinearity does not remove the essential behaviour associated with PT symmetry breaking. However, the eigenvalue structure and time dynamics are both enriched by the nonlinearity.

Gain and loss are much easier to manipulate in polariton condensates, but apart from simple mode selection arguments [15, 21], non-Hermitian effects were largely overlooked until the relatively recent observation of exceptional points achieved by engineering optically-induced potentials [7, 22]. Exceptional points can be reached because the real and imaginary parts of the energies of modes of optically-induced traps can be independently tuned by adjusting the trap depth and width [15]. This has allowed both for the observation of the topological phase acquired upon circling the EP, and also of chiral modes in the vicinity of the EP [7, 22]. However, the EPs studied were not associated with the PT symmetry breaking transition. On the theoretical side, a PT symmetric Josephson junction formed by coupled polariton condensates in micropillars has been investigated [97]. PT symmetry is achieved by optical pumping of one pillar whereas the other pillar experiences loss because of the radiative decay of polaritons. Although the work focuses on condensates below threshold, a range of interesting behaviour associated with the combination of nonlinearity and PT symmetry was revealed, including spontaneous breaking of PT symmetry and hysteresis. More generally, losses are present in the photonic part of the polariton wavefunction due to leakage from the cavity, and gain is present in the excitonic part due to stimulated scattering from the reservoir. If these are balanced, theoretical predictions indicate that the associated PT symmetry can give rise to effects such as permanent Rabi oscillations [98].

### 1.4.4 PT Symmetry and Nonlinearity

The study of nonlinear PT symmetric systems is an active and developing field [58, 86], which has arisen not just because of the inherent theoretical interest, but also because optical systems are nonlinear for sufficiently large field strength. This field is diverse and complicated because of the range of phenomena already present in both dissipative and conservative nonlinear systems [99], and also the extra degree of freedom that nonlinearity adds to PT symmetry. One can choose to study systems with a conventional nonlinearity and a PT symmetric linear potential, or systems with a PT symmetric nonlinearity.

One of the most interesting features of nonlinear systems is the existence of solitons - wavepackets that maintain their shape while propagating at a constant velocity. Solitons retain their shape because dispersion is counteracted by nonlinearity. As such, one branch of nonlinear PT symmetric theory focuses on solitons. It has been shown that in systems with a conventional nonlinearity and a PT symmetric linear potential, PT symmetric solitons exist, and there is an attendant PT symmetry breaking transition [100]. These

solitons can even exist for parameter values that would cause the linear system to be in the broken symmetry phase. That is, the nonlinearity modifies the PT symmetry breaking transition. PT symmetric solitons in lattice systems with both a PT symmetric nonlinearity and a PT symmetric linear potential have also been studied [101, 102]. The symmetry breaking transition for these solitons is retained even if the PT symmetric linear potential is removed. In contrast to dissipative systems that lack PT symmetry, solitons exist as parameter-dependent families of solutions rather than as fixed points in parameter space and are very stable [86]. These predictions have been confirmed in experiments with a PT symmetric mesh lattice that was implemented using two coupled fibre loops [103]. It has also been shown that solitons in nonlinear PT symmetric systems have integrals of motion, which can generically be hard to find in dissipative nonlinear systems [86].

More generally, studies of nonlinear coupled PT symmetric dimers have revealed that the nonlinearity significantly modifies the PT symmetry breaking transition [104, 105]. In fact the behaviour seen in linear systems can be reversed. With increasing non-Hermiticity, the system can transition first from the linear broken symmetry phase to the nonlinear broken symmetry phase, and then to the nonlinear unbroken symmetry phase. This behaviour is essentially a result of a saturable nonlinearity, and depends on whether lasing starts in a PT symmetric mode or a broken symmetry mode. In fact, if lasing initially occurs in the unbroken mode, the system remains in the unbroken phase regardless of the nonlinearity.

Closely related is the theoretical study of coupled atomic BECs in PT symmetric double well potentials, which are a nonlinear version of the simple two level model in Equation (1.28). This started with the study of the linear eigenstates for a collection of PT symmetric delta function potential [106], which demonstrated the existence of PT symmetric bound states for sufficiently small values of non-Hermiticity, with a symmetry breaking transition as the non-Hermiticity is increased. Numerical studies of (nonlinear) BECs in PT symmetric double wells confirmed the existence of PT symmetric bound states [93, 94]. The nonlinearity also enriches the behaviour - in the presence of nonlinearity, additional eigenstates appear. These are called "self-trapping" states because they are strongly confined to a single well. These extra states complicate the PT symmetry breaking behaviour resulting in both a second order EP where two PT symmetric solutions coalesce, and a third order EP where two broken symmetry solutions coalesce with an unbroken symmetry solution. For certain parameter values, these two EPs can coincide, resulting in a fourth order EP. Also, the non-Hermiticity alters the threshold for the appearance of self-trapping states, since both the broken PT symmetry states and the self-trapping states are localised in a particular well. The dynamics of this system were also studied, in particular the stability of solutions [95]. It was found that the PT symmetric stationary solutions become unstable near, but not exactly at the PT symmetry breaking transition point. This discrepancy essentially arises because the nonlinearity depends on the norm of the wavefunction, which is no longer conserved due to the non-Hermiticity. These results are supported by a simple theoretical toy model [92]. In addition, coupled PT symmetric wells have been studied using a Bose-Hubbard model, which in contrast to mean field theory describes the dynamics when only a few particles are present. It was shown that while linear model with $N$ particles has a pair of EPs, both of order $N+1$, nonlinearity breaks this in to a cascade of lower order EPs [107].

The crossing scenario for a particular nonlinear non-Hermitian two-level system was also analysed to generalise some of these results [108]. In the same way that the two level Hamiltonian (1.40) generically describes EPs of order two, this model generically describes the coalescence of two levels in a non-Hermitian system with a particular nonlinearity. The nonlinear eigenstates are defined as stationary states of a discrete nonlinear Schrodinger equation. This analysis revealed a hybrid structure that has features of both the linear non-Hermitian crossing scenario (that is, an EP as described in Section 1.4.2) and the nonlinear Hermitian scenario. Sufficiently strong nonlinearity causes loops in the nonlinear eigenvalue structure, and this manifests also in loops in the nonlinear non-Hermitian eigenvalue structure. Overall, this results in a complicated structure with many bifurcations that can be achieved by tuning various parameters. The dynamics were also investigated, and two competing processes were identified: the effect of nonlinearity, and also decay, which reduces the norm of the state and hence the effective nonlinearity.

Experimental investigations of nonlinear PT symmetric systems remain in their infancy. Aside from the observation of PT symmetric solitons in a mesh lattice [103], coupled PT symmetric microdisk lasers have also been studied [53, 54]. Although these systems are analogous to BECs in coupled PT symmetric wells, nonlinear effects have not been extensively considered. PT symmetry breaking simply selects the lasing mode. However, a significant enhancement of nonlinearity was reported, which was attributed to the population asymmetry associated with eigenstates in the broken symmetry phase.

# PT Symmetric Square Well for Polariton Condensates

In this chapter we discuss a PT symmetric square well for polariton condensates. The PT symmetric square well is very simple and has been investigated analytically [109–111]. It is therefore an attractive system for achieving PT symmetry breaking in polariton condensates, and could provide a more straightforward demonstration of an exceptional point than previous experiments with polariton condensates [7]. We explain how a nearly PT symmetric square well can be created for polaritons by combining a real potential created with an etch-and-overgrowth technique with an imaginary potential that is induced optically. Perfect PT symmetry cannot be achieved because the loss is fixed, and an optically-induced real potential is unavoidable. We explain that the imperfect PT symmetry removes the EP associated with the PT symmetry breaking transition, but that it can easily be restored. We also discuss a few possible challenges for experimental implementation.

## 2.1 PT Symmetric Square Well

The first PT symmetric Hamiltonians to be studied were inspired by field theory and were approached numerically and perturbatively [35]. In contrast, the PT symmetric square well is simple and amenable to analytic treatment, which clarifies the PT symmetry breaking transition. For an infinite square well of width $L$, the real part of the potential is reflected in the boundary conditions, $\psi(x = \pm L) = 0$, and the imaginary part is given by

$$W(x) = \begin{cases} -iZ, & x < 0 \\ iZ, & x > 0 \end{cases} \tag{2.1}$$

where $Z$ is the strength of the non-Hermiticity. This potential is shown in Figure 2.1 (a). Since the real part is symmetric and the imaginary part is antisymmetric, this potential is PT symmetric according to the condition given in Section 1.4.1.

The eigenstates of this potential have been studied extensively by Znojil, who derived transcendental equations for the eigenvalues which he then solved graphically [110]. Some details of the graphical solution are shown in Figure 2.2. This analysis revealed that below a critical value of non-Hermiticity, $Z_c \approx 4.48$, all the eigenvalues are real. As $Z$ is increased beyond $Z_C$, the real parts of the lowest two eigenvalues merge, and the
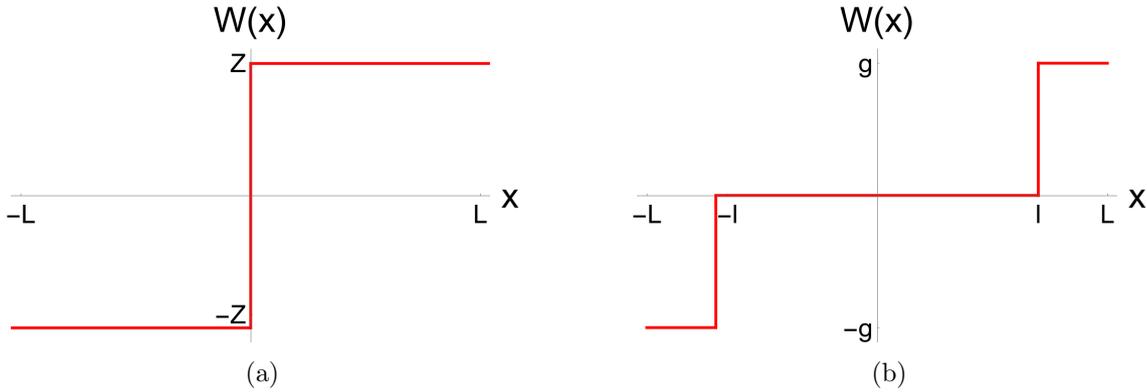
Figure 2.1: Imaginary part of the potential for (a): PT symmetric square well, Equation (2.1), (b): PT symmetric square well with a stepped potential, Equation (2.2).

eigenvalues continue in to the complex plane as complex conjugates [109]. With increasing $Z$, this behaviour repeats for successively larger pairs of eigenvalues, $E_{2n}$ and $E_{2n+1}$ whose real parts merge, generating an increasing sequence of thresholds, $Z_C^0 < Z_C^1 < \cdots$. This behaviour mirrors that of other PT symmetric Hamiltonians, where eigenvalues remain real until a certain parameter reaches a threshold [35].

In Figure 2.3 we show numerically computed eigenvalues and eigenstates of the PT symmetric square well to shed light on the PT symmetry breaking transition. Below the transition, the states that eventually merge are symmetric with respect to reflection about the centre of the well and hence each experience balanced loss and gain, resulting in purely real eigenvalues. Above the transition, the states lose reflection symmetry, and are mirror images of one another, which means their real parts remain equal, but their imaginary parts have the opposite sign. One becomes localised in the gain region, and the other in the loss region.

Much richer behaviour was later uncovered for a more complicated stepped imaginary potential of the form

$$W(x) = \begin{cases} -ig & -L < x < -l \\ 0 & -l < x < l \\ ig & l < x < L \end{cases},$$

(2.2)

in which the strength of the non-Hermiticity is controlled by two parameters, $g$ and $l$. This potential is shown in Figure 2.1 (b). The non-Hermiticity parameter, $Z$, is defined by $g = 2Z/(L-l)^2$ [111]. The introduction of a second parameter considerably complicates the graphical analysis, and the method of moving lattice must be employed [112]. This method allows for eigenvalues to be split in to two different classes based on the type of graphical intersection they correspond to. Eigenvalues of one class remain real at any value of Z, and are classified as stable. Eigenvalues of the other class are real below a certain value of Z, after which they merge in pairs and then become complex conjugates just like the eigenvalues of the simpler PT symmetric square well in Equation (2.1). The distinction between stable and unstable energies can be tuned in an intuitive way. For $l \approx L$, when the potential is nearly Hermitian, all of the energies are stable, whereas for $l \ll L$, which corresponds to the simpler PT symmetric square well, all of the energies
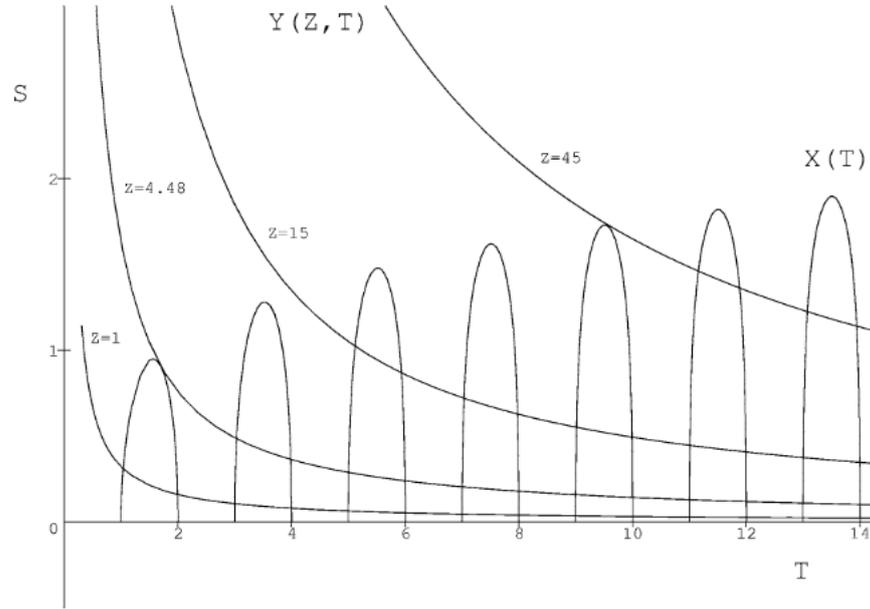
Figure 2.2: Details of graphical solution for the energies of a particle confined to a PT symmetric square well. After a reparamaterisation, energies are determined by intersections of the curves $X(T)$ and $Y(Z,T)$, in the $S$-$T$ plane. The energy is directly determined by the values of $S$ and $T$, and the curve $Y(Z,T)$ depends on the strength of the non-Hermiticity, $Z$. It is plotted for several values of $Z$. For small values of $Z$, the curve $Y(Z,T)$ is low, and there are infinite number of pairs of intersections. However, as $Z$ increases to the critical value $Z_C \approx 4.48$, the first pair of energies merges. As $Z$ increases further, successively higher pairs of energies merge. Note that the associated solution does not disappear after the merging of levels. In fact, the energies continue in to the complex plane as conjugates [109]. This is not evident from graphical solution, which is constructed assuming real energies. Reproduced from [110].

are unstable. For intermediate values of $l$, the stable and unstable energies are interspersed.
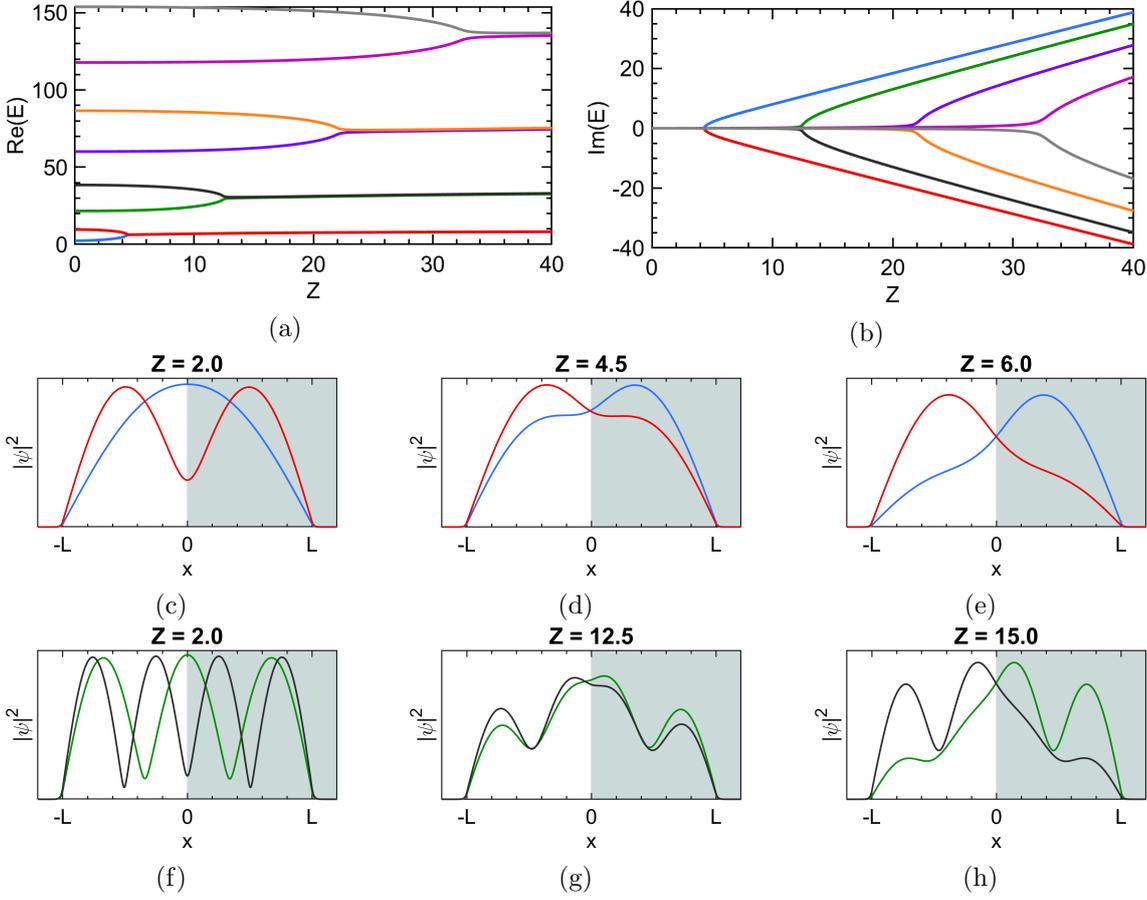
Figure 2.3: Eigenvalues and eigenstates of the PT symmetric square well. The dependence of the eigenvalues on the non-Hermiticity, $Z$ is shown in (a) and (b). With increasing non-Hermiticity, the real parts of successively larger pairs of eigenvalues merge. Before the real parts merge, the imaginary parts, (b), are both zero. After the real parts merge, the eigenvalues become complex conjugates. Studying the corresponding eigenstates, whose position densities are shown in (d)-(f) for the first pair, and (g)-(k) for the second pair, sheds light on the PT symmetry breaking transition. For low values of $Z$, shown in (c) and (f), eigenstates are similar to eigenstates of a Hermitian square well. Since they have reflection symmetry about the middle of the well, their overlap with the gain region (shaded in blue) is the same as the overlap with the loss region, so the imaginary part of the eigenvalue is zero. However, slightly above the PT symmetry breaking transition ((d) and (g)), the states lose reflection symmetry, and one becomes more localised in the gain region, with the other more localised in the loss region. The localisation is even more pronounced for larger values of $Z$, shown in (e) and (h). After the transition, the second state is the reflection of the first one about the centre of the well. Since the real part of the potential is symmetric and the imaginary part is antisymmetric, this means the real parts of the energies are equal, and the imaginary parts have the opposite sign. Note that the parity operation is reflection about the centre of the well ($x = 0$). Below the transition, states are symmetric with respect to the parity operation since they are not changed after reflecting about the origin. Above the transition, they lose parity symmetry due to localisation in the gain or loss region.

## 2.2   PT Symmetric Square Well for Polaritons

Implementing a PT symmetric square well for polaritons condensates is attractive for a number of reasons. The observation of PT symmetry breaking in polariton condensates is particularly interesting because polariton condensates are an inherently quantum system, whereas observations of PT symmetry breaking in optics rely on similarity between the classical wave equation and the Schrodinger equation. Exceptional points have previously been observed in polariton condensates [7, 22], but they were not associated with the PT symmetry breaking transition. As we have explained in Section 2.1, the behaviour of a *stepped* PT symmetric square well is much more subtle. Polariton condensates could serve as a useful system to test these predictions of PT symmetric quantum mechanics. Finally, polariton condensates benefit from a strong nonlinearity, which allows for the exploration of the interplay between nonlinearity and PT symmetry.

A nearly PT symmetric square well can be created for polaritons by combining a real trapping potential induced by local cavity lengthening (achieved with an etch-and-overgrowth method as discussed in Section 1.3) with an imaginary potential shaped by both the intrinsic loss of polaritons and the gain provided by a laser pump. Potentials induced with local cavity lengthening are typically on the order of $5\,\mathrm{meV}$ to $10\,\mathrm{meV}$ [27], deep enough to confine several states [26]. Although these potentials are two dimensional, quasi-one-dimensionality could be achieved by only elongating a narrow strip. Alternatively, one-dimensional condensates have been observed in microwire cavities formed by chemical etching [113, 114], and in ZnO microwires [115]. The intrinsic loss of polaritons manifests as a constant negative imaginary potential whereas a laser pump induces gain through the excitation of reservoir polaritons that feed the condensate by stimulated scattering as explained in Section 1.2. Hence a pump with a step profile will induce a stepped imaginary potential in the well. If the pump edge is aligned with the centre of the well, and the gain induced by the pump is exactly twice the intrinsic polariton loss, the well will be PT symmetric as shown in Figure 2.4. However, the pump also induces a real potential due to repulsive interactions with reservoir polaritons, which perturbs the PT symmetry. This potential is generally small compared to the gain, and its size is set by the density of the incoherent reservoir created by the pump as well as by the polariton-reservoir interaction strength. After eliminating the reservoir as in Equation (1.20), the total potential for polaritons given a stepped pump has real and imaginary parts

$$\mathrm{Re}\,V(x) = \begin{cases} V_0 & x < -L \\ 0 & -L < x < 0 \\ \frac{g_R}{\gamma_R}P & 0 < x < L \\ V_0 + \frac{g_R}{\gamma_R}P & x > L \end{cases}$$

and

$$\mathrm{Im}\,V(x) = \begin{cases} -\frac{i\hbar}{2}\gamma_C & x < 0 \\ \frac{i\hbar}{2}\left(\frac{RP}{\gamma_R} - \gamma_C\right) & x > 0 \end{cases} \tag{2.3}$$

where $V_0$ is the depth of the square well, $g_R$ is the condensate-reservoir interaction strength, $\gamma_R$ is the reservoir loss rate, $\gamma_C$ is the condensate loss rate, $P$ is the pump rate, $R$ is the

stimulated scattering rate from the reservoir to the condensate, and $2L$ is the width of the well. This potential is shown in Figure 2.4.
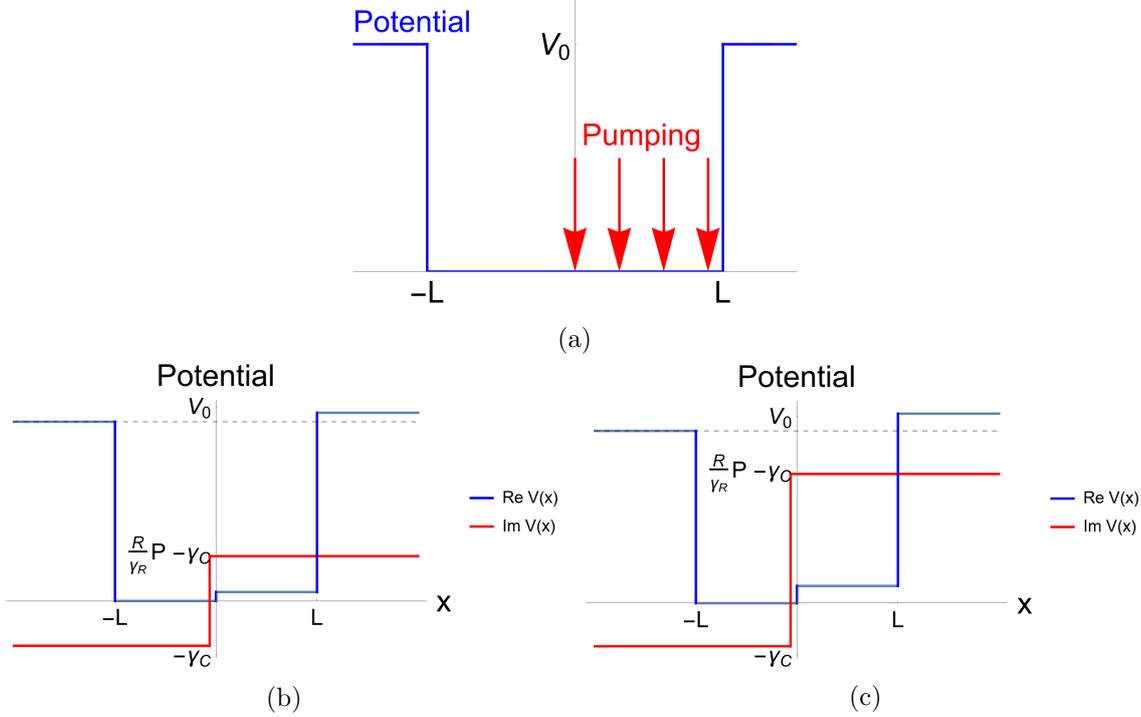


Figure 2.4: Nearly PT-symmetric potential for polaritons for: (a) balanced loss and gain, $P = 2\gamma_C\gamma_R/R$, (b) higher power, $P = 4\gamma_C\gamma_R/R$. The real potential is the sum of an external finite square well potential and pump-induced potential. The imaginary potential is the sum of the pump-induced gain and the natural polariton loss. The imaginary part of the pump-induced potential has been offset slightly for clarity.

This potential is not exactly PT symmetric. PT symmetry requires the real part of the potential to be symmetric and the imaginary part to be antisymmetric. Because the loss is fixed and the gain varies, the imaginary part is generally not antisymmetric. Antisymmetry is attained only when $P = 2\gamma_C\gamma_R/R$, that is when the gain induced by the pump is exactly twice the polariton loss rate. The real part of the potential is not symmetric because the pump induces a real potential as well as gain. Moreover, antisymmetry of the imaginary part of the potential is achieved only for a particular pump strength whereas the PT symmetry breaking transition occurs for a particular strength of antisymmetric imaginary part. When the imaginary part of the potential is antisymmetric, its strength may be far from that required for the transition. Condensation also occurs at a particular pump strength and is associated with a significant drop in the linewidth [5, 116]. If the PT symmetry breaking threshold is close to the condensation threshold, characteristics of condensation may obscure the symmetry breaking transition, which is inferred partly from the linewidths of the associated states. Finally, the well depth is finite whereas only an infinite PT symmetric square well has been studied before.

Simple estimates can clarify some of these problems. After appropriate rescaling the imaginary part of the potential relates to the parameter $Z$ of the PT symmetric infinite

square well, Equation (2.1), as

$$Z = \frac{2 \operatorname{Im}(V) L^2 m}{\hbar^2},$$
(2.4)

where $m$ is the polariton effective mass. For a typical polariton effective mass, $m = 10^{-4} m_{e^-}$, a well size $L = 10 \, \mu\text{m}$, and $P = 2\gamma_C \gamma_R / R$, chosen to make the imaginary part antisymmetric, we have $Z = 6.72$, which is very close to the critical value $Z_C^0 \approx 4.48$, where the lowest two energies merge and become complex conjugates. This shows that when asymmetry of the imaginary part of the potential is achieved, the strength of the imaginary part is approximately correct to induce the PT symmetry breaking transition. Also, these pump strengths are well above the homogeneous condensation threshold, $P_{\text{th}} = \gamma_R \gamma_C / R$, which in turn is higher than the condensation threshold in the trap. This means that the condensation threshold should not interfere with observation of the PT symmetry breaking transition.

The size of the asymmetry in the real part of the potential is $P g_R / \gamma_R$, which is equal to $g_R R / \gamma_R$ for the value of $P$ that makes the imaginary part antisymmetric. For typical parameters[1], this asymmetry is on the order of $10^{-1}$meV, much smaller than typical trap depths which are on the order of several to $10 \, \text{meV}$ [26, 27]. This shows that the real part of the potential will remain approximately symmetric for pump powers that induce the PT symmetry breaking transition. Finally, the ratio of the real part of the pump-dependent potential to the imaginary part is

$$\frac{\operatorname{Re} V_P}{\operatorname{Im} V_P} = \frac{\hbar}{2} \frac{R}{g_R},$$
(2.5)

which is approximately 1 for the typical values quoted before. This means that the real part of the pump dependent potential increases at the same rate as the imaginary part. Therefore we are assured that the asymmetry in the real potential will remain small even when the power is increased enough to cause merging of the energy levels. Although the potential is not exactly PT symmetric, it will remain nearly PT symmetric for experimental parameters that should induce the PT symmetry breaking transition.

## 2.3    Numerical Results

The first step towards implementing a PT symmetric square well for polaritons is determining whether the asymmetries we identified are large enough to remove the PT symmetry breaking transition. To support the approximate arguments, we can systematically investigate the effects of these asymmetries. In particular, we investigate the linear single-particle states of the system, which correspond to stationary solutions of the ODGPE, Equation (1.16), when nonlinearity is neglected, by numerically solving the Schrodinger equation in position space with the potential in Equation (2.3). We discretise the Hamiltonian on a Chebyshev grid [117], a task made simple with the use

---

[1]$g_R \approx 10^{-3}$meV $\mu\text{m}^2$, and $\gamma_C \approx 10^{-1}\text{ps}^{-1}$. The term $R$ is inherently phenomenological so its value cannot be measured. However values on the order of $\hbar R \approx 10^{-4}$meV $\mu\text{m}^2$ are typically used to successfully model experiments [7].

of Chebyshev differentiation matrices, and then solve for the complex eigenvalues and eigenvectors of the corresponding matrix using standard methods[2]. Since the potential is piecewise linear, it would also be possible to derive and numerically solve transcendental equations to find the eigenvalues. For simplicity, we focus on the coalescence of the lowest two eigenstates, but as we have explained in Section 2.1, in the PT symmetric square well, pairs of eigenstates with successively higher energies coalesce with increasing non-Hermiticity. Our results are hence readily adapted to the EP associated with coalescence of eigenstates with higher energy. We focus on a square well that is $10\,\mu m$ wide, with a potential depth of $5\,meV$, consistent with potentials that can be created with an etch-and-overgrowth technique [26]. We use typical values of polariton parameters[3], which determine the size of the fixed loss, and the potential induced by the pump.

### 2.3.1   Effect of Asymmetries

Figures 2.5 and 2.6 show the pump power dependence of the first two eigenvalues for the finite square well. Because energies of the first two eigenstates are well below the potential barrier, the results for an infinite square well are identical. For comparison with previous analytical results, we convert the pump power to the dimensionless parameter, $Z$, as explained in Section 2.2. In Figures 2.5 (a) and (b), we show the results for a PT symmetric square well. As predicted by previous analytical results [109, 110], the eigenvalues are real below the critical value, $Z_C \approx 4.48$, after which the real parts merge and the imaginary parts become complex conjugates.

In Figure 2.5 (f) and (h) we model the fixed polariton loss and varying pump-dependent gain. Even though the value of polariton loss means that PT symmetry (where the gain induced by the pump is exactly twice the polariton loss) does not occur at the critical value of $Z$, the essential features of the PT-symmetry breaking transition and EP are retained. Below a critical value of $Z$, the imaginary parts of the eigenvalues are equal and increase linearly with $Z$. At a critical value of $Z$, the real parts merge and the imaginary parts diverge. Although the eigenvalues are no longer complex conjugates, the imaginary parts diverge from the previous linear increase at the same rate. This behaviour is identical to that predicted in quasi PT-symmetric passive optical systems, where only varying loss is present [36, 118]. In these systems, PT symmetric behaviour is reproduced after a formal relabelling of the fields, which amounts to factoring out the fixed loss. In fact, the stepped imaginary potential considered in (f) and (h) can trivially be decomposed in to an antisymmetric part plus a fixed part, both of which grow with the pump power. The stepped imaginary potential is given by

$$W(x) = \begin{cases} -iV_1 & -L < x < 0 \\ iV_2 & 0 < x < L \end{cases}, \tag{2.6}$$

---

[2]For a square well $10\,\mu m$ wide, we discretise a $20\,\mu m$ region with approximately 1000 grid points. Since the bound states decay outside the well, we impose the Dirichlet boundary condition that the wavefunction vanishes at the edge of the discretisation region. This is easily accomplished by retaining only the interior points of the Chebyshev grid. It is well-known that such spectral methods converge rapidly with the number of grid points provided the solution is smooth [117], and convergence is easily verified by increasing the number of grid points until the computed eigenvalues converge.

[3]$m = 4 \times 10^{-4} m_{e^-}$  $g_R = 7 \times 10^{-4} meV\,\mu m^2$, $\gamma_C = 5 \times 10^{-2} ps^{-1}$, $\hbar R \approx 6.5 \times 10^{-3} meV\,\mu m^2$

which can be rewritten in the form

$$W(x) = \left\{ \begin{array}{ll} -iV_3 + iV_4 & -L < x < 0 \\ iV_3 + iV_4 & 0 < x < L \end{array} \right. , \tag{2.7}$$

where $V_3$ is the magnitude of the antisymmetric part, and $V_4$ is the fixed part, by choosing $V_3 = (V_1 + V_2)/2$ and $V_4 = (V_2 - V_1)/2$. In Equation (2.6), $V_1 = \tilde{\gamma}$ represents the dimensionless polariton loss rate, and $V_2 = \tilde{P} - \tilde{\gamma}$ represents the net gain due to pumping, so $V_3 = P/2 + \tilde{\gamma}$, which explains why the critical value of $Z$ is increased compared to the PT symmetric square well. Also, $V_4 = \tilde{P}/2 - \tilde{\gamma}$, which explains why the imaginary parts of the eigenvalues increase with pump power.

In Figures 2.6 (a) and (b) we return to an antisymmetric imaginary potential, but model the effect of the pump-dependent real potential by adding a small real potential that is proportional to pump rate. The constant of proportionality is determined by the polariton parameters as explained in Section 2.2. The imaginary parts of the eigenvalues still remain equal up to a threshold after which they become complex conjugates. However, the real parts no longer coalesce, and the divergence of the imaginary parts of the eigenvalues is smoothed compared to the PT symmetric square well. The eigenstate which acquires a positive imaginary part in the transition in Figure 2.6 (b) is localised in the gain region, and its energy is therefore increased, precluding degeneracy in the real parts in (a). In Figure 2.6 (f) and (g) we model all the asymmetries: fixed loss with varying gain, and the real part of the pump-induced potential. Compared to (a) and (b), the divergence of the imaginary parts and coalescence of the real parts is further smoothed.
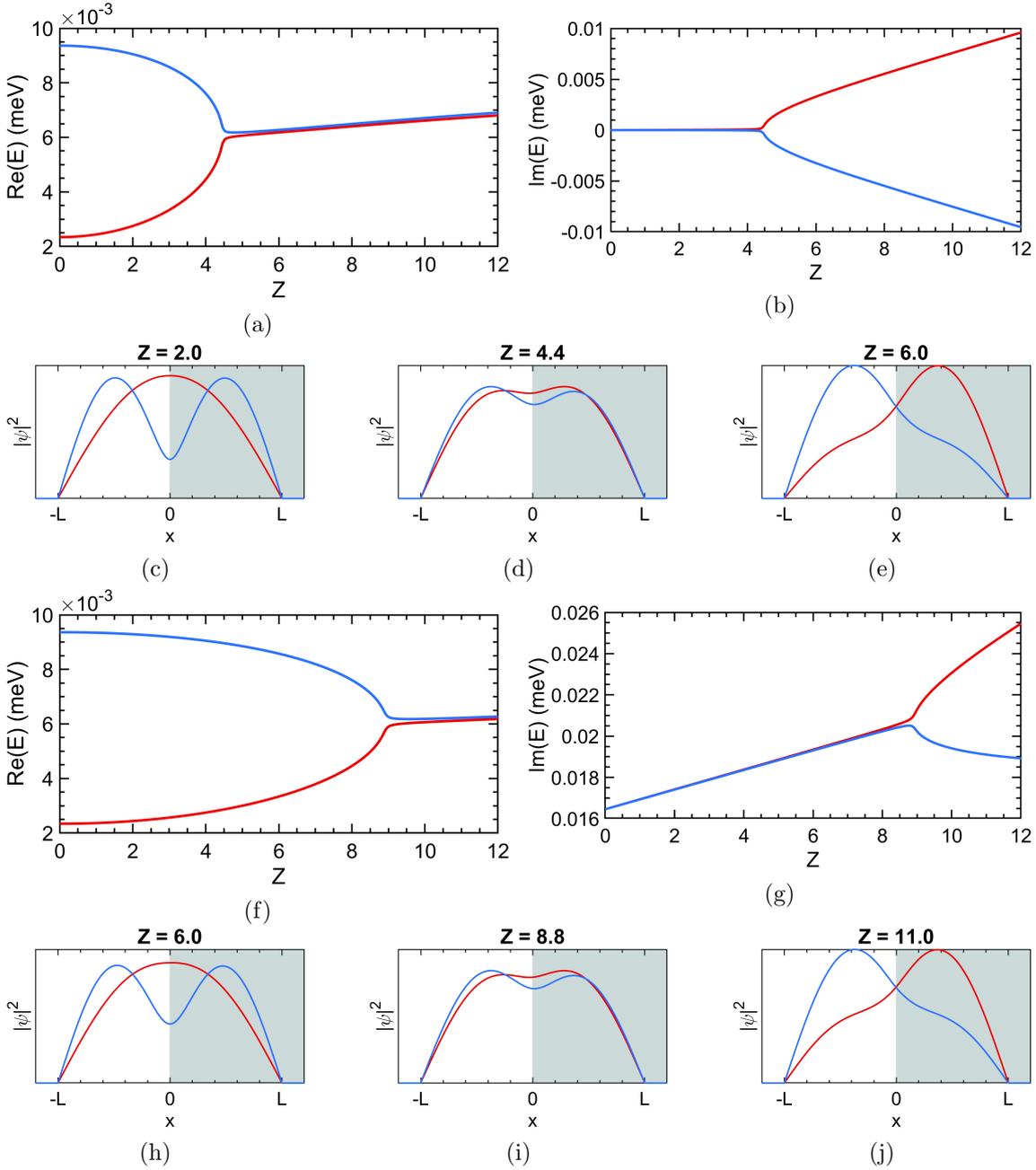
Figure 2.5: Lowest two eigenvalues and corresponding eigenstates of a non-Hermitian finite square well for various degrees of PT asymmetry: (a)-(e) PT symmetric, (f)-(j) fixed loss and varying gain. $Z$ is the dimensionless magnitude of the imaginary part of the potential (positive imaginary part for fixed loss and varying gain), consistent with the notation in [109–111]. The fixed loss is given by the polariton parameters as explained in Section 2.2. Fixed loss does not remove the essential characteristics of the PT symmetry breaking transition. The coalescence of the real parts remains, and the divergence of the imaginary parts is simply superimposed on a linear dependence on the gain. This is because the underlying eigenstates, (h)-(j) are identical for those in the perfectly PT symmetric case. The PT symmetry breaking threshold is slightly increased.
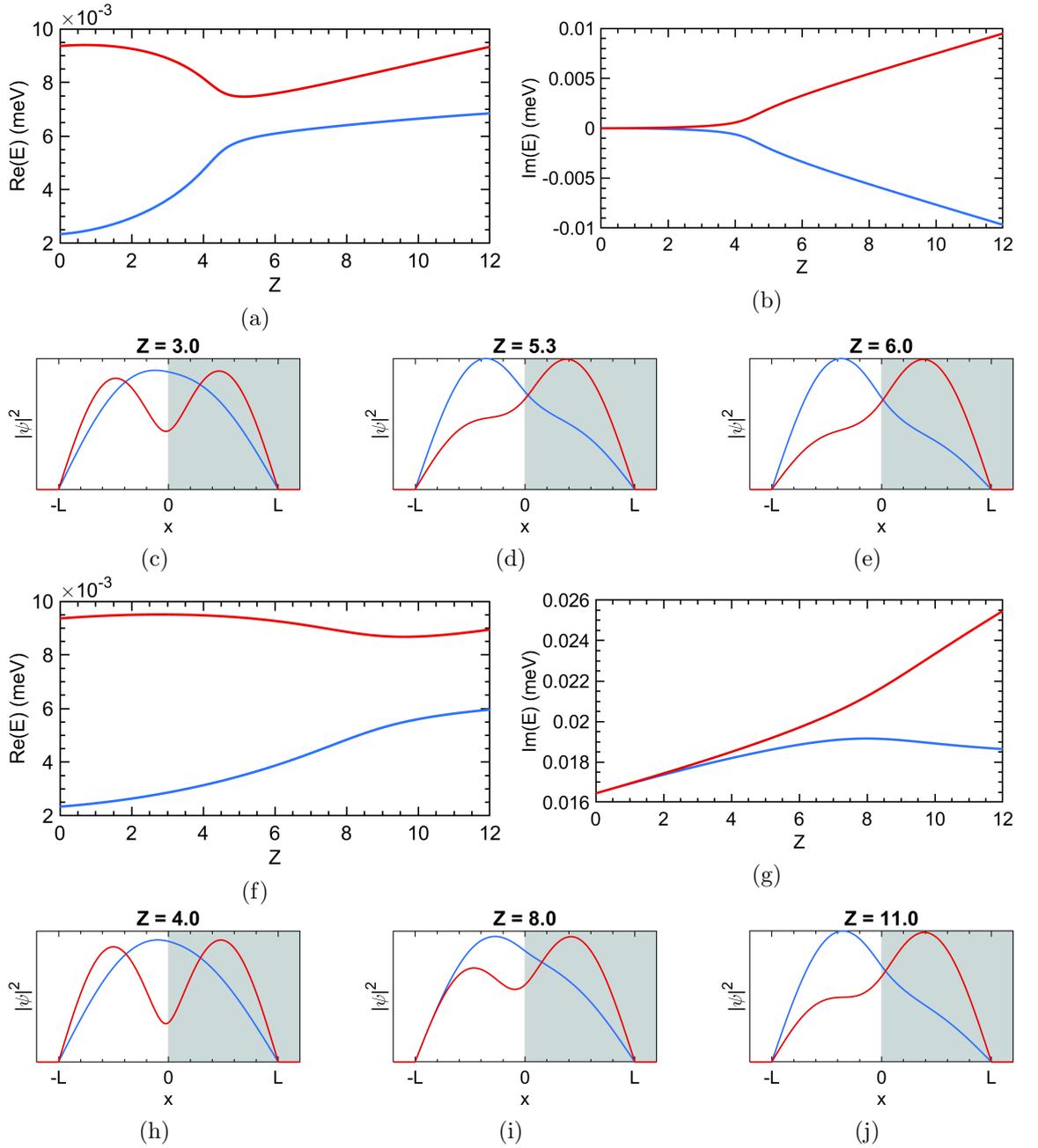
Figure 2.6: Lowest two eigenvalues and corresponding eigenstates of a non-Hermitian finite square well for various degrees of PT asymmetry: (a)-(e) balanced loss and gain, but with a real perturbation that increases with the imaginary part of the potential, (f)-(j) fixed loss and varying gain, with a real perturbation that increases with the imaginary part of the pump-dependent potential. $Z$ is the dimensionless magnitude of the imaginary part of the potential (positive imaginary part for the cases with fixed loss and varying gain), consistent with the notation in Section 2.1. The fixed loss, and the ratio of the real part of the pump-dependent potential to the imaginary part are set by the polariton parameters as explained in Section 2.2. As shown in (a) and (b), the real part of the pump-dependent potential removes the PT symmetry breaking transition. The real parts of the eigenvalues no longer coalesce, and the divergence of the imaginary parts is significantly smoothed. This is because the eigenstates, (c)-(e), no longer have reflection symmetry about the centre of the well. The eigenstate that is localised in the gain region (red) has a larger overlap with the real part of the potential, increasing its energy and precluding coalescence of the real parts of the eigenvalues. Combining the extra real potential with fixed loss and varying gain, as shown in (f)-(j) further smooths the PT symmetry breaking transition.

### 2.3.2   Restoring the Exceptional Point

As shown in Figure 2.6, the asymmetry associated with the real part of the pump dependent potential removes the EP associated with the PT symmetry breaking transition. A natural question is whether the EP associated with the transition can be restored. A similar smoothing of the EP has been observed in nearly PT symmetric optical waveguide systems, for example plasmonic structures [55, 119]. The smoothing here is considered undesirable because the singular behaviour of the imaginary parts of the eigenvalues near the EP can be exploited to implement switching [57]. The smoothing was attributed to a complex coupling coefficient in the coupled mode theory that varies with gain, a reflection of the slight lack of PT symmetry [119]. Based on this observation, a method to restore the exceptional point by modifying the detuning between the waveguides was proposed [55]. Only the eigenvalue difference of the coupled waveguides, and the gain and loss of the isolated waveguides is required to compute the optimal detuning, and these could be inferred from coupled mode simulations. As explained in Section 1.4.2, it is generally necessary to tune two parameters two drive a system to an EP. For the special case of a PT symmetric system, only one parameter is required. If the PT symmetry is slightly perturbed, a second parameter must be introduced to restore the EP.

Inspired by the previous results for waveguides, we have attempted to restore the EP in our nearly PT symmetric square well by varying a second parameter. Since we deal with eigenstates of a fixed potential rather than coupled waveguides, there is no clear way to derive a coupled mode theory that describes the EP for the nearly PT symmetric square well, so the previous results cannot easily be applied. Instead, we adjust the position of the pump-dependent potential, moving the position of its edge slightly away from the centre of the square well (see Figure 2.4). It easy to vary the position of the laser pump in the experiment, and it is also clear that this may restore the EP. The real part of the pump-dependent potential removes the EP because it increases the energy of the eigenstate that experiences gain, that eigenstate being more localised in the pump region. This precludes degeneracy in the real parts of the eigenvalues. Moving the edge of the pump confines the lossy mode, increasing its energy as well. We determine the location that restores the EP by optimising the pump power and position relative to the edge of the well to enforce simultaneous degeneracy of both the real and imaginary parts of the eigenvalues. We find that a shift corresponding to about 1% of the well width restores the EP.

We present several signatures of restoration of the EP[4]. An EP is defined by simultaneous coalescence of the eigenvalues and eigenstates, which can only be verified approximately with numerical simulations, and requires the EP to be exactly found in the pump power - pump position plane. Instead, the existence of an EP inside a particular region of parameter space is often verified by the characteristic transition from crossing to anticrossing of the real and imaginary parts of the eigenvalues, and the behaviour when the EP is encircled in parameter space [7, 72], both of which are explained in Section 1.4.2. To this end, we record the power dependence of the eigenvalues for two

---

[4]The EP cannot be exactly resolved due to the spectral resolution of the Chebyshev technique, which is set by the grid resolution. Since the technique involves diagonalising a matrix, high grid resolutions become impractical.

different pump edge positions which place the system on either side of the EP. These results are shown in Figure 2.7, which shows the characteristic transition from crossing to anticrossing of the real and imaginary parts of the eigenvalues near the EP [52]. For one pump edge position (Figure 2.7 (a-c)), the imaginary parts of the eigenvalues cross and the real parts do not. For the other pump edge position, this behaviour is reversed - the real parts cross, but the imaginary parts do not, indicating that there is an EP in the pump power - pump position plane located between the two curves. Figure 2.7 (d-f) and (j-i) shows a few eigenstates evaluated at particular pump powers. For the pump powers closest to the EP, corresponding approximately to (f) and (j), it is clear that the eigenstates are nearly identical. This is further evidence for an EP since a simultaneous coalescence of the eigenvalues and eigenstates is required. Also, near the EP, both eigenstates are more localised near the left side of the well, which supports the assertion that moving the pump edge restores the EP by confining the states in the loss region.

We also uncover topological features by tracking the eigenvalues and eigenstates as a contour in the pump power vs pump position parameter plane is traversed. This contour either encloses the EP (Figure 2.8), or does not (Figure 2.9). Figures 2.8 (a-c) show that encircling the EP causes both the eigenvalues and eigenstates to swap. Note that although we have only plotted the eigenstates at a few selected positions around the contour, we are able to correctly label them by carefully tracking the eigenvalues. Conversely, as shown in Figure 2.9 (a-c), when we traverse a contour that is identical apart from a kink on one side so as not to enclose the EP, neither the eigenvalues nor eigenstates swap. The exchange of eigenstates when the EP is enclosed is further confirmation of an EP.

It is not surprising that an EP can be achieved by simultaneously modifying the pump power and position, but it appears that shifting the pump edge position also restores many of the features of the PT symmetry breaking transition. The lines of constant pump position shown in Figure 2.7 are both taken very close to the EP. In (c) and (f) it is clear that the imaginary parts of the eigenvalues are approximately equal and increase slightly with pump power. After a critical power, they split and diverge from the linear increase at an equal rate. The real parts merge and then remain approximately equal. This is very similar to the behaviour for a PT-symmetric square well, shown in Figure 2.5 (g), where the eigenvalues are purely real below the threshold power, after which they diverge and become complex conjugates. The trace of the PT symmetry breaking transition is also reflected in the eigenstates which are shown in Figure 2.7 (j)-(l). Below the critical pump power, the eigenstates are approximately symmetric, whereas above the critical power they are highly asymmetric, with one more localised in the lossy region of the well and the other more localised in the gain region provided by the pump.

There are a few potential limitations to implementing this scheme in experiments. To restore the EP, only a small shift in the pump edge position of around 1% of the well width is required. This shift may be smaller than the precision in the laser pump position which would mean the EP could not be reliably observed. However, the shift in pump position is required to counteract the asymmetry imposed by the real part of the pump-dependent potential, so if the real part of the pump-dependent potential were larger, a larger shift would be required. As detailed in Section 2.2, the magnitude of the real part of the pump-dependent potential is set by the parameters $g_R$ and $\gamma_R$.
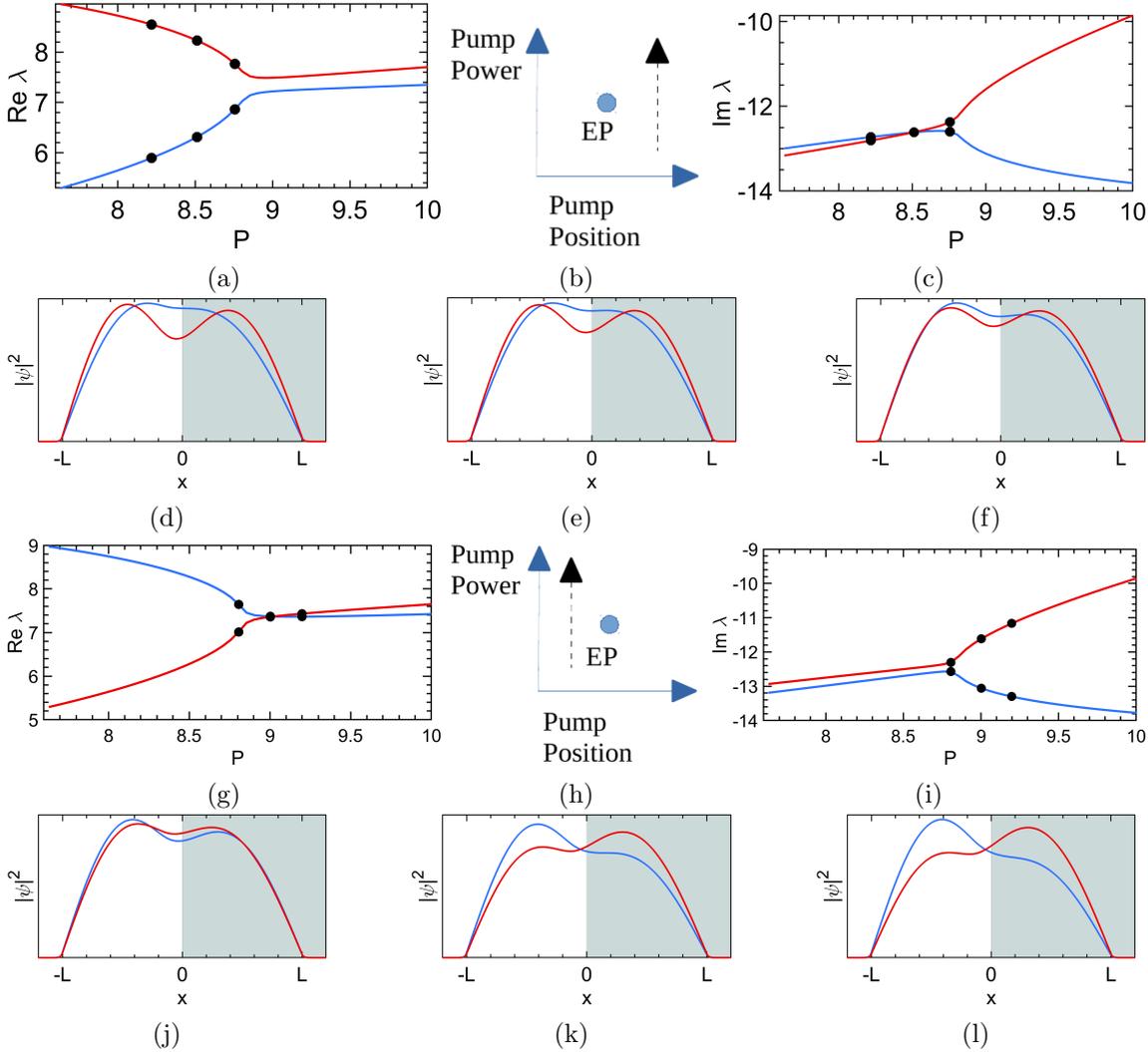
Figure 2.7: Characteristic transition from crossing to anticrossing of the real and imaginary parts of the real and imaginary parts of the eigenvalues near the EP. Here, we fix the pump edge position, and then vary the pump power and record the real (a) and imaginary (c) parts of the eigenvalues of the first two eigenstates. In (g) and (i), we do the same, but for a different pump edge position. These different pump edge positions put the system on different sides of the EP, as illustrated in (b) and (h). The characteristic crossing and anticrossing behaviour confirms the presence of an EP - on one side of the EP (a-c), the real parts of the eigenvalues do not cross, but the imaginary parts cross. This behaviour is reversed on the other side of the EP (g-i). The real parts cross and the imaginary parts do not. This is behaviour is explained in Section 1.4.2. In (d-f) and (j-l) we show the wavefunctions at the points indicated in (a-c) and (h-i). The wavefunctions closest to the EP are shown in (f), (l).

(a)                                                                    (b)

(c)
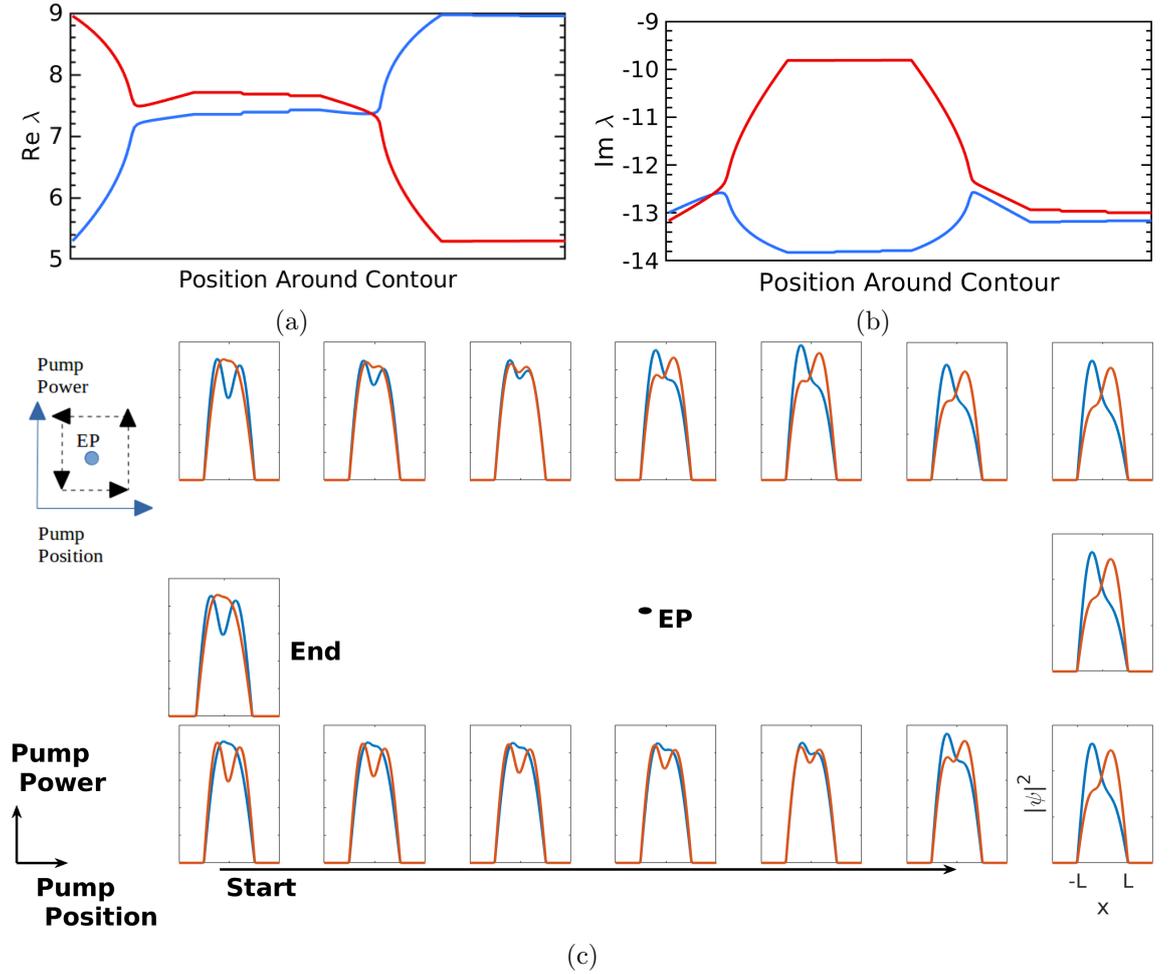
Figure 2.8: Encircling the EP with a closed contour in pump power, pump position space. In (a) and (b) the real and imaginary parts of the eigenvalues are plotted against the distance around the contour. The contour we trace is also illustrated. In (c), the eigenfunctions are plotted. Although the eigenfunctions are only plotted for a few parameter values, we can track their identity using the eigenvalues. The eigenstates at the end of the contour are identical to those at the start except that they have been interchanged. It is clear that encircling the encircling the EP exchanges the eigenstates.

The polariton-reservoir interaction strength, $g_R \sim g_{\text{exciton-exciton}}|X^2|$, depends on the polariton-exciton detuning since excitonic polaritons interact more strongly with the reservoir [120]. We have assumed a detuning that results in a fairly weak real part, but a different detuning will result in a larger real part that will require a larger correction, which makes experiments more feasible.

As shown in Figure 2.7 (c, i), the imaginary parts of the eigenvalues associated with the restored EP are large and negative, which limits experimental observability since modes with large loss may not be populated. This is entirely expected since shifting the pump edge confines the states to the loss region. In an experiment this could be mitigated by pumping across the whole well to ensure net gain, but with asymmetry to induce the EP. As we explained in Section 2.3.1, a net gain will simply shift the imaginary part of the eigenvalues without removing the behaviour associated with the PT symmetry

breaking transition.
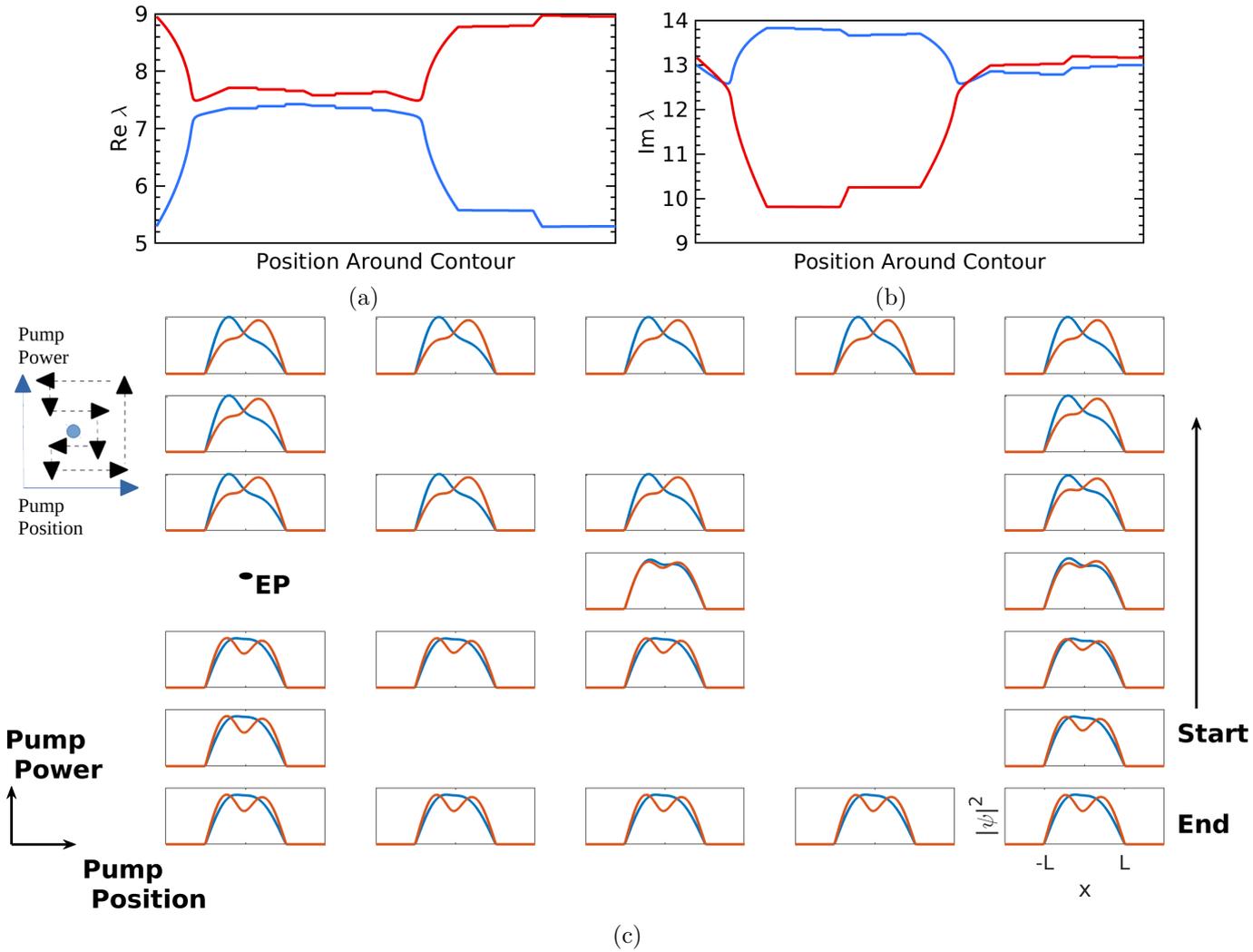
Figure 2.9: Traversing a contour that does not enclose the EP. In (a) and (b) the real and imaginary parts of the eigenvalues are plotted against the position around the contour. In (c), the eigenfunctions are plotted. The contour we trace is also illustrated. Although the contour has the same start and end points as the one in Figure 2.8 (it is identical apart from the left side, where there is a kink to avoid the EP), the eigenstates at the end of the contour are the same as at the beginning. If the EP is not included, traversing the contour does not cause the eigenstates to swap.

## 2.4   Conclusions and Further Work

The PT symmetric well is one of the simplest PT symmetric systems and has the advantage of being analytically tractable. The PT symmetry breaking transition is readily understood - successively larger pairs of eigenvalues merge and become complex conjugates when the non-Hermiticity is increased. Despite the simplicity, a PT symmetric square well with a stepped imaginary potential exhibits subtle and complicated behaviour. In particular, there exists tuneable interspersion of collections of eigenvalues that either remain real or become complex with increasing non-Hermiticity. We have investigated the possibility of realising a PT symmetric square well for polariton condensates, which would allow not only for the observation of PT symmetry breaking and the attendant exceptional point, but also provide a means for experimentally demonstrating previous theoretical predictions.

A PT symmetric square well for polariton condensates could be implemented by combining a real potential arising from confinement of the photonic part of the polariton wavefunction, for example by local cavity lengthening achieved with an etch-and-overgrowth technique, with a stepped imaginary potential that arises from the combination of the intrinsic polariton loss and the gain provided by a pump laser. However, such a potential would not be exactly PT symmetric because the loss is fixed but the gain varies, and the pump also induces a real potential. We have provided order of magnitude arguments to show that these asymmetries should remain small, and also systematically modelled the effect of these asymmetries on the PT symmetry breaking transition. We find that for typical polariton parameters, the asymmetry of the real part of the potential removes the PT symmetry breaking transition and the associated EP since it increases the energy of the state localised in the gain region. However, we have shown that the EP can be restored simply by slightly shifting the pump edge position from the centre of the well, which confines the lossy mode, slightly increasing its energy. Moreover, restoring the EP also restores many of the features of the PT symmetry breaking transition. Although a quantitative comparison is not possible, this technique is very similar to the restoration of an EP in nearly PT symmetric plasmonic systems by adjusting the detuning between coupled modes [55]. The nearly PT symmetric square well consists of a gain region coupled to a loss region. Adjusting the pump position relative to the mesa edge changes the sizes of these regions and hence the detuning. These results show that it should be possible to observe the PT symmetry breaking transition in a nearly PT symmetric square well for polaritons.

There is still much scope for future work. Focusing first on experimental implementation, a few technical details must be clarified. It may be necessary to investigate whether the required shift of the pump edge position can be increased. If the shift is smaller than the noise in the laser spot position, it will not be possible to reliably restore the EP in experiments. Operating at a different detuning, which modifies the polariton parameters, can increase the real part of the pump-dependent potential which should increase the required shift. Also, the imaginary part of the potential in an experiment will not have a step profile. Even if the laser profile is sharp, the potentials will be slightly smoothed due diffusion of the reservoir carriers. It is clear that a larger shift will be required for a smoothed profile, and it will also be necessary to investigate how much

smoothing increases the required shift. Most importantly, numerical simulations of the full ODGPE must be performed. The numerical work we have performed only identifies the linear eigenstates of the system. Time-dependent simulations will establish whether these eigenstates are strongly populated by the pumping scheme we use to achieve near PT symmetry. Full simulations will also clarify the effect of the nonlinearity induced by polariton-polariton interactions, which may alter the PT symmetry breaking behaviour as explained in Section 1.4.4.

There is also much more work to be done that goes beyond observation of the PT symmetry breaking transition associated with the coalescence of the lowest two eigenvalues. One obvious question is whether our trick of shifting the pump position restores the PT symmetry breaking transition for all pairs of states, or just for the lowest two. Previous analytical work for a PT symmetric square well with a more complicated imaginary potential [112] would suggest that shifting the pump position may restore the transition for a limited set of states, interspersed among states that do not undergo the transition. In fact, this previous theoretical treatment is readily adapted to our square well with a shifted pump. This would provide predictions about what will happen to states with higher energy, and may also clarify why shifting the pump edge restores the EP.

# Polariton Whispering Gallery Modes in Circular Traps

In this chapter we focus on whispering gallery modes (WGMs) of polariton condensates in circular traps. We review the results of an experiment that demonstrates excitation of many WGMs in a circular trap, and model this system using both a linear theory and a full simulation of the ODGPE. In addition, we present a phenomenological theory that explains some of more surprising experimental results. We also discuss schemes that have been used to drive WGMs of optical microresonators to exceptional points, and present numerical results which demonstrate some of these schemes are feasible for polariton WGMs.

## 3.1    Background

Whispering gallery modes (WGMs) are modes that are highly localised near a concave surface. The study of WGMs began with the peculiar acoustics of the so-called whispering gallery at St Paul's Cathedral in London. In this dome, whispers uttered close to the wall travel unusually large distances. This phenomenon was studied by Lord Rayleigh [121], who predicted the existence of modes of the cavity with low principal mode number and high azimuthal mode number. A simple geometrical model is that WGMs propagate by repeated reflection around the inside of the cavity, as illustrated in Figure 3.1. Because they are localised to the surface, the intensity of a WGM decays with the propagation distance, rather than the cube of the propagation distance as is the case for free waves [81]. In addition, losses upon reflection are relatively small, so WGMs typically have very high quality factors.

WGMs are generally present given a curved boundary or confining potential, and have been observed in a wide range of systems, including optical resonators [81], electron matter waves [122], exciton-polaritons [123, 124], and even antihydrogen [125]. WGMs have been most useful in optics. They are particularly attractive for a number of reasons: low mode volumes and high Q factors cause large field intensities and imply long ringdown times, and the localisation near the resonator boundary means WGMs are sensitive to external perturbations. WGM resonators facilitate research in quantum optics [126], nonlinear optics [126], lasers [127], and sensing [128].
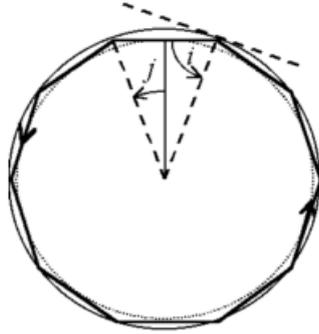
Figure 3.1: Ray picture of WGM propagation. WGMs propagate by repeated reflection from the cavity walls. Reproduced from [81].

Exceptional points (EPs) of WGMs in optical systems have been used to demonstrate interesting effects such as thresholdless single mode operation [56], and enhanced sensing [61, 62]. EPs are in principle easy to attain for polaritons because of intrinsic loss due to mirror leakage, and the ease of manipulating gain using optical pumping. This makes the study of EPs in polariton systems particularly promising.

## 3.2   Previous Work

### 3.2.1   WGMs for Polaritons

There have been multiple demonstrations of WGMs for polaritons. One branch of research studies ZnO micropillars. These micropillars provide strong confinement for photons, so polaritons are formed by the coupling of photonic WGMs to excitons [129]. ZnO pillars are an attractive experimental system because they are readily grown using chemical methods, and ZnO is a promising material for photonic devices [130]. However the polariton lifetime is limited by loss through the sides of the pillars. Strong coupling and the formation of exciton-polaritons has been demonstrated [123], as has polariton lasing [131, 132]. Energy relaxation dynamics has also been comprehensively studied, with the conclusion that parametric scattering between different WGMs in multimode condensates drives effective cooling [124].

WGMs of polariton condensates have also been observed in optically-induced annular traps [15]. In the regime studied, condensation into a particular mode of the trap is driven primarily by gain, leading to occupation of only a few modes which have the lowest condensation thresholds. By varying the strength and diameter of the pump, the gain of different modes - which depends on both the mode's overlap with the pump and the intrinsic mode shape - can be tuned, enabling the selection of particular modes, and switching between them. This includes trapped modes that are localised inside the pump annulus and also WGMs. Gain-based selection of WGMs is a slightly counterintuitive result since these modes are localised in the pump region, at the location of a repulsive potential which is created by a pump-injected reservoir [29]. The results are bolstered by

a theory of mode selection in trapped polariton condensates, which carefully considers loss and gain to formulate condensation thresholds in terms of solutions of a non-Hermitian eigenvalue problem [9]. This work represented a significant advance in the understanding of mode selection in polariton condensates, which was previously understood in relatively simplistic terms [21]. However, a serious weakness is that it only considers condensation thresholds and thus cannot provide an account of population redistribution due to relaxation processes.

Recent theoretical work focuses on frequency comb generation using polaritons in semiconductor microring resonators [133]. The authhours consider a microring that is coupled to a microwire. The microwire, excited with CW pumping, provides a resonant excitation to the microring. These structures can be fabricated with lithography or etch-and-overgrowth techniques [23]. Using coupled equations of motion for photons and excitons, it is possible to show that the whispering gallery modes can be significantly blueshifted by the excitonic nonlinearity. In addition, the nonlinearity allows for mode-locked pulses, which generate frequency combs.

Our work focuses on a relatively shallow circular potential for polaritons which is formed by local cavity lengthening, accomplished with an etch-and-overgrowth technique [23], discussed in Section 1.3. It has been shown in experiments that the induced trap supports several bound states [26], and this experimental work is bolstered by theoretical analysis [27]. Because polariton confinement is achieved by confining the photonic component of polaritons, a rigorous treatment must consider the confined photon modes, which are computed and then coupled to the planar exciton modes. The photon modes are discretised due to the local cavity lengthening, which creates an optical WGM resonator since the photon energy depends on the cavity length. This leads to discretisation of the polariton modes as well.

Building on this, our work studies polaritons in a similar trap formed by local cavity lengthening. The existence of whispering gallery modes in such traps was hinted at in the early theoretical work [27], but our work focuses exclusively on them, in particular on non-Hermitian aspects of these polariton WGMs. In contrast to the experiments with optically-induced potentials, trapping is provided by cavity lengthening rather than the pump, which also induces gain. This allows us to more carefully manipulate gain, and explore non-Hermitian effects. In addition, since gain is decoupled from the trapping potential, many modes can be populated. This is aided by our focus on relatively photonic detunings, where energy relaxation processes, mediated by exciton-exciton scattering [134] or interaction with lattice phonons [6] are weaker. In contrast with the recent theoretical work that emphasises the effects of nonlinearity [133], we are investigating the regime where these effects are negligible.

### 3.2.2  WGMs and EPs

Optical whispering gallery mode resonators (WGMRs) have been a fruitful platform for observing EPs because of the degeneracy between counterpropagating modes, and

because the strong localisation of WGMs near the boundary of the resonator means they are readily perturbed. The perturbation may be realised by a modification of the resonator boundary, or by placing a particle nearby, but outside the resonator to induce scattering between counterpropagating WGMs. To demonstrate an exceptional point it is necessary to adjust two parameters. Generally, the perturbation lifts a degeneracy in the real part of the energy, or couples two modes that are close in energy. The imaginary parts of the energies are then adjusted by tuning the imaginary part of the resonator refractive index to achieve an exceptional point. Alternatively, a PT symmetric system of coupled WGMRs is arranged, and the system is driven through the PT symmetry breaking transition to achieve an exceptional point. Here, the strong localisation of WGMs allows for coupling to be mediated and tuned simply by placing the resonators close together. Exceptional points are of particular interest for WGMRs because these resonators are used to construct sensors [81, 125]. The square-root behaviour of eigenvalues near an exceptional point can be used to greatly enhance sensitivity [59–62].

One approach to creating an EP in a WGMR is to induce asymmetrical scattering of counterpropagating WGMs by systematically perturbing the boundary of the resonator. This is best understood using a phenomenological toy model that describes the coupling between counterpropagating WGMs with the same azimuthal quantum number in cavities that lack mirror symmetry. Examples of such cavities include asymmetric limaçons [67] and microspiral cavities [66], illustrated in Figure 3.2. In the travelling wave basis, the Hamiltonian reads

$$H = \begin{pmatrix} E_0 & 0 \\ 0 & E_0 \end{pmatrix} + \begin{pmatrix} \Gamma & V \\ \eta V^* & \Gamma \end{pmatrix}. \tag{3.1}$$

The eigenvalues of the first matrix represent the energies of the counterpropagating modes in an unperturbed resonator, and the second matrix represents the coupling induced by the perturbation. The real parameter $\eta$ describes the degree of asymmetry, and when $\eta \neq 1$, the Hamiltonian is non-Hermitian. In the case of a spiral cavity, illustrated in Figure 3.2, the cause of the asymmetry is clear - waves propagating clockwise encounter the notch and are scattered to the counterclockwise direction, but this does not happen to waves propagating in the other direction. The eigenvalues and eigenvectors are

$$E_\pm = E_0 + \Gamma \pm \sqrt{\eta}|V|, \tag{3.2}$$

and

$$\alpha_\pm = \frac{1}{\sqrt{2}} \begin{pmatrix} 1 \\ \pm\sqrt{\eta}e^{-i\delta} \end{pmatrix}, \tag{3.3}$$

where $\delta$ is the complex argument of $V$. When $\eta \neq 1$, the eigenvectors are not orthogonal, and for small values of $\eta$ the eigenstates are nearly degenerate but are not orthogonal. In the limit of perfectly asymmetrical scattering, $\eta = 0$, and the eigenvalues and eigenvectors simultaneously coalesce. That is, an EP is reached. The physical reason for the EP is completely clear. When $\eta = 0$, waves travelling CW are all scattered but waves travelling CCW are not affected, so only one eigenstate remains.

It has been shown that perfectly asymmetrical scattering and hence an EP can be achieved using two external scatterers [68], for example silica nano-tips placed near an optical WGMR. This scheme was used to operate an optical WGM sensor near an EP,
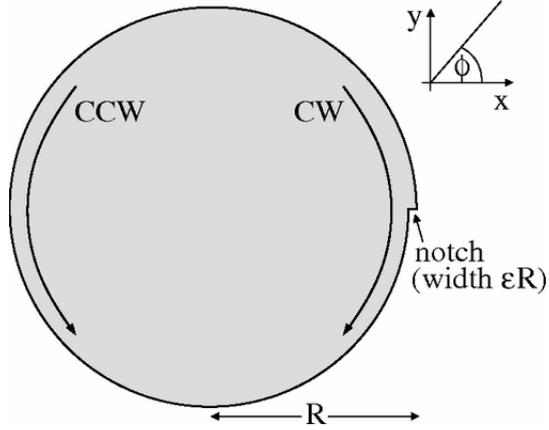
Figure 3.2: Microspiral Cavity. A small notch induces asymmetric scattering between counterpropagating (CW and CCW) WGMs with the same azimuthal mode number, resulting in a non-Hermitian two-level Hamiltonian (Equation (3.1)). Reproduced from [66]

yielding a significant improvement in sensitivity [60, 61].

A single external scatterer will introduce only symmetrical scattering. However, interference between waves scattered by two different scatterers allows a pair of scatterers to induce asymmetrical scattering. The interference can be tuned simply by adjusting the angle between the scatterers. For a given azimuthal mode number, $m$, a single external scatterer lifts the degeneracy between the even WGMs (which have a $\cos(m\phi)$ angular dependence) and odd the WGM (which have a $\sin(m\phi)$ angular dependence). If the scatterer is large enough to perturb both modes then the (Hermitian) perturbation Hamiltonian is given in the standing-wave basis by

$$H_1 = \begin{pmatrix} 2V_1 & 0 \\ 0 & 2U_1 \end{pmatrix}, \tag{3.4}$$

where the entries are complex and $|U_1| < |V_1|$ since the even parity mode is perturbed more than the odd parity mode for small scatterers. The parameters $V_1$ and $U_1$ must be calculated numerically, for example using a boundary-element method [135]. If a second scatterer is added with an angular position $\phi = \beta$, then in the travelling-wave basis the total perturbation is given by the Hamiltonian

$$H = \begin{pmatrix} \Omega & A \\ B & \Omega \end{pmatrix}, \tag{3.5}$$

where

$$\Omega = \Omega_0 + V_1 + U_1 + V_2 + U_2, \tag{3.6}$$

$$A = V_1 - U_1 + (V_2 - U_2)e^{-i2m\beta}, \tag{3.7}$$

and,

$$B = V_1 - U_1 + (V_2 - U_2)e^{i2m\beta}, \tag{3.8}$$

where $\Omega_0$ is the frequency of the unperturbed mode. The dependence on $\beta$ reflects the

phase acquired by a wave when propagating between the scatterers. The eigenvalues and eigenvectors are

$$\Omega_\pm = \Omega \pm \sqrt{AB}, \tag{3.9}$$

and

$$\psi_\pm = \begin{pmatrix} \sqrt{A} \\ \pm\sqrt{B} \end{pmatrix}. \tag{3.10}$$

In general, $V_j$ and $U_j$ are complex since the scatterers also cause loss, so the matrix in Equation (3.5) is non-Hermitian. Clearly, when either $A = 0$ or $B = 0$, the scattering is completely asymmetric and both the eigenvalues and eigenvectors coalesce. That is, an exceptional point occurs. Completely asymmetric scattering can be achieved by tuning the angle between the scatterers. For example, in the case of identical scatterers, for which $V_1 = V_2$ and $U_1 = U_2$, setting $\beta = \pi/2m$ yields $e^{-2im\beta} = -1$, and hence $A = 0$. This means that the CW to CCW scattering due to the first scatterer is exactly balanced by that due to the second scatterer. For EPs induced by asymmetric scattering, chirality of the eigenstate is reflected in unidirectional propagation. Asymmetric scattering means that only one of the two counterpropagating modes is preferred. This scheme has been used to create a WGM sensor which operates at an EP. Tuning the sensor to an EP increases its sensitivity to a target particle because of the square-root dependence of energies in the vicinity of an EP [59–61]. More recently, it has been proposed that asymmetric scattering induced by coupling a WGM resonator to a waveguide with a mirror at only one end yields a hypersurface of EPs, which may allow for the creation of an EP sensor which is robust to unwanted perturbations [136].

Instead of coupling degenerate counterpropagating WGMs, an EP can be realised by coupling WGMs to modes with a higher principal quantum number by making a small deformation of the cavity boundary. Because of the high degree of symmetry, it is generally possible to find WGMs that are nearly degenerate to modes that have a higher principal quantum number. This means that the required boundary deformation can be a thousand times smaller than the cavity radius [137, 138]. A perturbation theory for nearly-degenerate modes of circular cavities has been developed which allows for the magnitude of the required perturbation to be calculated [139, 140]. Tuning to an EP generally requires two parameters, so a two-parameter perturbation is required, or it is necessary to tune the imaginary parts of the mode energies by adjusting the imaginary part of the cavity refractive index. This scheme can be adapted to achieve higher-order WGMs.

Similarly, an EP can be engineered by coupling internal modes of a WGMR to external modes. Internal modes are the conventional bound states, which include WGMs. They are localised inside the cavity and have low decay rates. External modes, in contrast, are localised outside the cavity and have a large decay rate [141]. The real parts of the relevant modes can be brought to degeneracy simply by adjusting the real part of the cavity refractive index. The imaginary parts may be brought to degeneracy either by adjusting the imaginary part of the refractive index, or by introducing a perturbation to the cavity boundary that degrades the Q factor of the internal mode to match it to that of the external mode.

Finally, there are a number of schemes that use the PT symmetry breaking transition

to achieve an exceptional point [53, 62, 77, 78]. PT symmetry can be attained either in a photonic molecule consisting of two coupled WGMRs, one of which experiences gain and the other loss, or for a single WGMR by imposing periodic gain and loss regions which line up with the antinodes of the WGM. Both systems are described by the PT symmetric two-level Hamiltonian in Equations (1.29) and  (1.44).

Achieving EPs and PT symmetry breaking in polariton WGMs is attractive for a number of reasons. Polaritons are already a promising system for future optoelectronic devices [142], and effects associated with EPs of photonic WGMs such as enhanced sensing [61], and thresholdless single mode lasing [56] could be harnessed in polaritonic devices. Also, a demonstration of PT symmetry breaking in polariton condensates is attractive since they are an inherently quantum system. Polaritons also have a few properties that may be useful in engineering EPs of a PT symmetry breaking transition. Real and imaginary potentials for polaritons can be easily induced with a laser pump. The real potential arises from repulsive interactions between polaritons and reservoir carriers that are created by the pump whereas stimulated scattering from the reservoir to the condensate induces gain which manifests as an imaginary potential. To this end, the rest of this chapter is devoted to aspects of polariton WGMs in a circular trap.

## 3.3   Experimental Results

The circular trap is formed by patterning a shallow circular mesa on top of the spacer of the microcavity, which lengthens the cavity slightly, lowering the energy of the photon mode, as illustrated in Figure 1.6 and explained in Section 1.3. Such traps have previously been studied theoretically [27] and experimentally [26], but the focus was not on WGMs. The trapping potential for polaritons is approximately 5.1 meV, and the radius of the trap is approximately 10 μm. The trap is excited by shining a small (2 μm FWHM) CW laser pump spot on the boundary of the mesa. The spatial and momentum distribution of photoluminescence and spatially-resolved spectrum are recorded in the experiment. The experiment is performed at a relatively photonic detuning, corresponding to a photonic fraction, $|C|^2 \approx 0.88$, where energy relaxation processes are relatively weak [6, 134], allowing for the population of many states.

The experimental features with a single pump spot on the edge of the mesa are shown in Figure 3.3. The spectrum, Figure 3.3 (a), shows the occupation of a large number of discrete energy states with narrow linewidths that are localised near the edge of the trap. These states span an energy range of over 15 meV, with many above the potential barrier (5.1 meV). They are WGMs of the polariton condensate in the circular potential. For WGMs with energies higher than the trapping potential barrier, confinement is provided by a combination of the mesa potential and an effective centrifugal potential, as we explain in Section 3.4.1 below. A few other features are apparent: laterally-trapped states with energies lower than the mesa potential barrier are occupied, and there is emission from the planar condensate outside the mesa whose energy is set by the potential induced by the pump. Our simulations in Section 3.4.2 confirm that the energy of this planar condensate is several meV higher than the mesa potential barrier. Some asymmetry in intensity between the two sides of the mesa is also evident. This is a

(a)



(b)



(c)



(d)



(e)
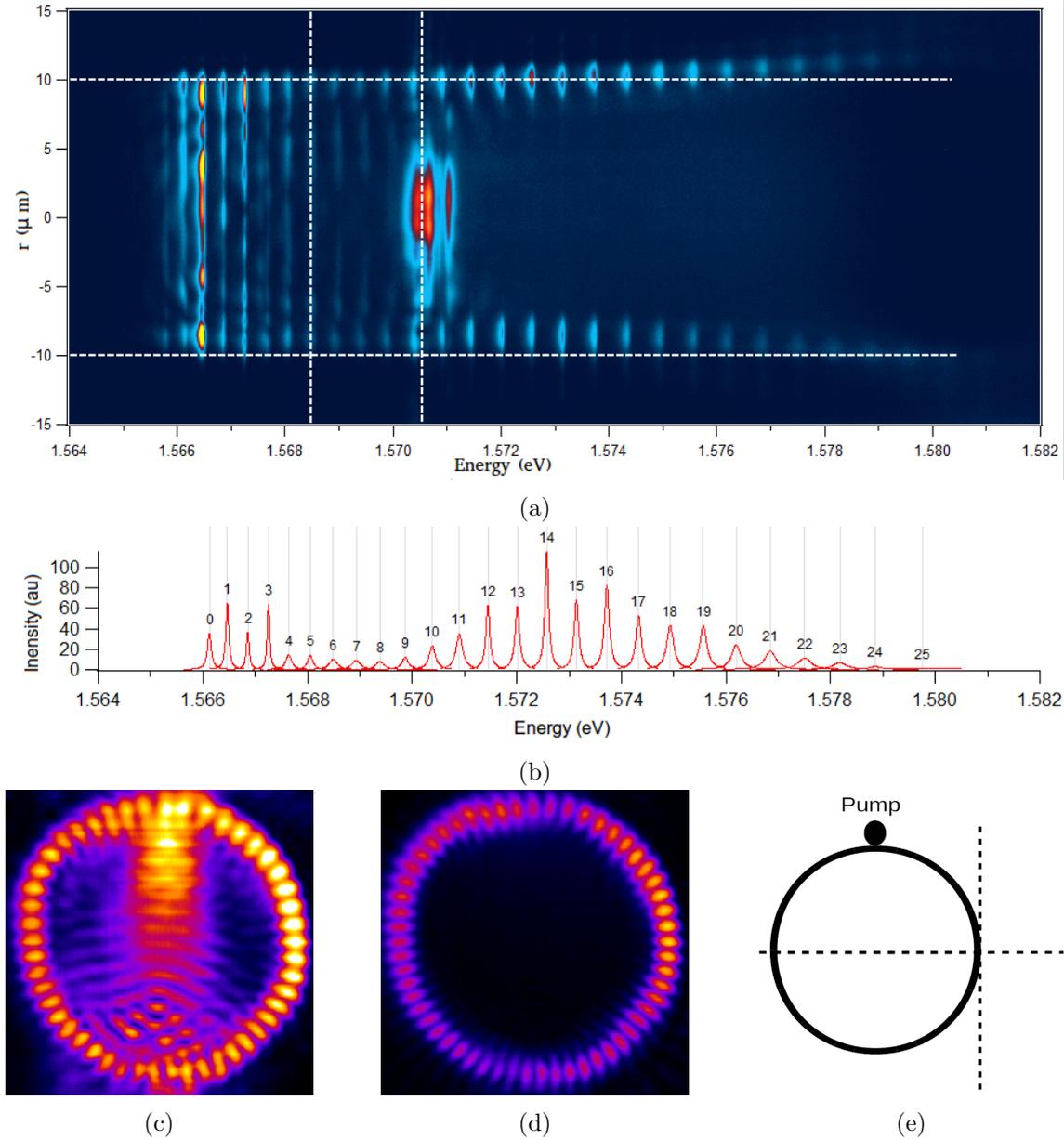
Figure 3.3: Experimental features of polariton condensation in a circular trap. The trap has a radius of $10\,\mu$m and is excited with a $2\,\mu$m pump spot near its edge. The spectrum, (a), is recorded by taking a slice across the diameter of the trap, $90°$ from the pump spot, as illustrated in (e). A large number of modes spatially localised near the trap edge are occupied. These are whispering gallery modes. Many of these modes have energies larger than the trapping potential, and are present due to radial confinement provided by the combination of the trapping potential and an effective centrifugal potential (see Section 3.4.1). Significant planar emission is present around $1.5705\,$eV, which our simulations (see Section 3.4.2) show is a few meV above the potential barrier, itself at $1.5685\,$meV. Occupation of trapped lateral modes below the energy of the confining potential is also evident. Asymmetry between the left and right sides of the trap is present due to the exciton-photon detuning gradient, which causes a small potential gradient. A line profile, (b), of the emission taken at $r \approx 10\,\mu$m (see (e)) confirms the occupation of many modes and reveals an envelope in the amplitudes. Energy-filtered photoluminescence is shown in (c) and (d), taken at approximately $1.571\,$eV and $1.573\,$eV, corresponding to $l = 24$ and $l = 28$ respectively.

consequence of the exciton-photon detuning gradient of the sample, which imposes a small linear potential gradient of approximately $0.1\,\text{meV}\,\mu\text{m}^{-1}$ for polaritons. A line profile, Figure 3.3 (b), of the spectrum taken at $r \approx 10\,\mu\text{m}$ confirms the occupation of discrete modes with narrow linewidths. An envelope in the emission intensity is also evident. The states closest in energy to the planar condensate are most strongly populated. We also show energy-filtered photoluminescence, Figure 3.3 (c) and (d), taken at approximately $1.5790\,\text{eV}$ and $1.571\,25\,\text{eV}$ respectively. An azimuthal nodal pattern typical of a WGM is apparent. Some emission from the planar condensate is also present at the lower energy, as is the asymmetry due to the detuning gradient. In addition to the planar emission at the lower energy, both filtered images exhibit some emission inside the potential opposite to the pump spot. The pattern of this emission is identical to short-lived components in the spatial mode pattern caused by an effective perturbation to the trap boundary, which have been predicted for optical WGMRs with a small boundary perturbation [140]. Counting the number of azimuthal antinodes reveals the azimuthal quantum number of the state. When this is done for all of the states in Figure 3.3 (a), a sequential increase in azimuthal quantum number is revealed. The quantum numbers are shown in Figure 3.3 (b). These results demonstrate excitation of a large number of WGMs.

The most interesting behaviour emerges when the condensate is excited by two pump spots as shown in Figure 3.4. Figure 3.4 (a) shows a line profile in energy, which is produced by first recording the spectrum by taking a slice across the mesa diameter, perpendicular to the line joining the two pump spots, and then extracting a slice at $r \approx 10\,\mu\text{m}$, as illustrated in (e). From bottom to top, the energy profile with only the first spot, only the second spot, and finally the two spots (blue) are shown. The most striking feature is a massive increase in polariton population coupled with a blueshift of exactly half the mode spacing, or free spectral range (FSR) when the second pump spot is added. Filtering the photoluminescence and counting antinodes demonstrates that the new spectral peaks correspond to blueshifted WGMs. The increase in population can not be attributed solely to the increased excitation density with two pump spots since the power in the original pump spot is split in half to generate the two spots.

The power dependence of the blueshift is shown in Figure 3.4 (b), where we focus on a few states and generate a waterfall plot by varying the power of the second pump spot. The blueshift and amplitude of the peaks initially increase rapidly with power. At higher powers, the blueshift saturates at half the FSR whereas the amplitude continues to increase with power. This is made clearer in Figure 3.4 (d), where we have extracted and plotted the blueshift against peak amplitude for each of the peaks shown in Figure 3.4 (b).

Since the blueshift is accompanied by a large increase in population, it is natural to assume that the blueshift is caused by polariton-polariton interactions, which induce a local blueshift of $g_C\, n(x)$, where $n(x)$ is the polariton density, and $g_C$ is the polariton-polariton interaction strength. However, elementary analysis of the data shows that the blueshift cannot be attributed to polariton-polariton interactions. Figure 3.4 (d) shows that for high powers, the blueshift saturates while the population increases by up to a factor of 3. If the blueshift were caused by polariton-polariton interactions, it would increase linearly with polariton population. Also, in Figure 3.4 (c), we extract both the blueshift and amplitude of each of the peaks shown in Figure 3.4 (a) and plot these. There is no clear

correlation between the blueshift and population increase. If the blueshift was caused by polariton-polariton interactions, a linear correlation would be seen. This evidence demonstrates that the blueshift cannot be attributed to polariton-polariton interactions.

(a)



(b)



(c)



(d)



(e)
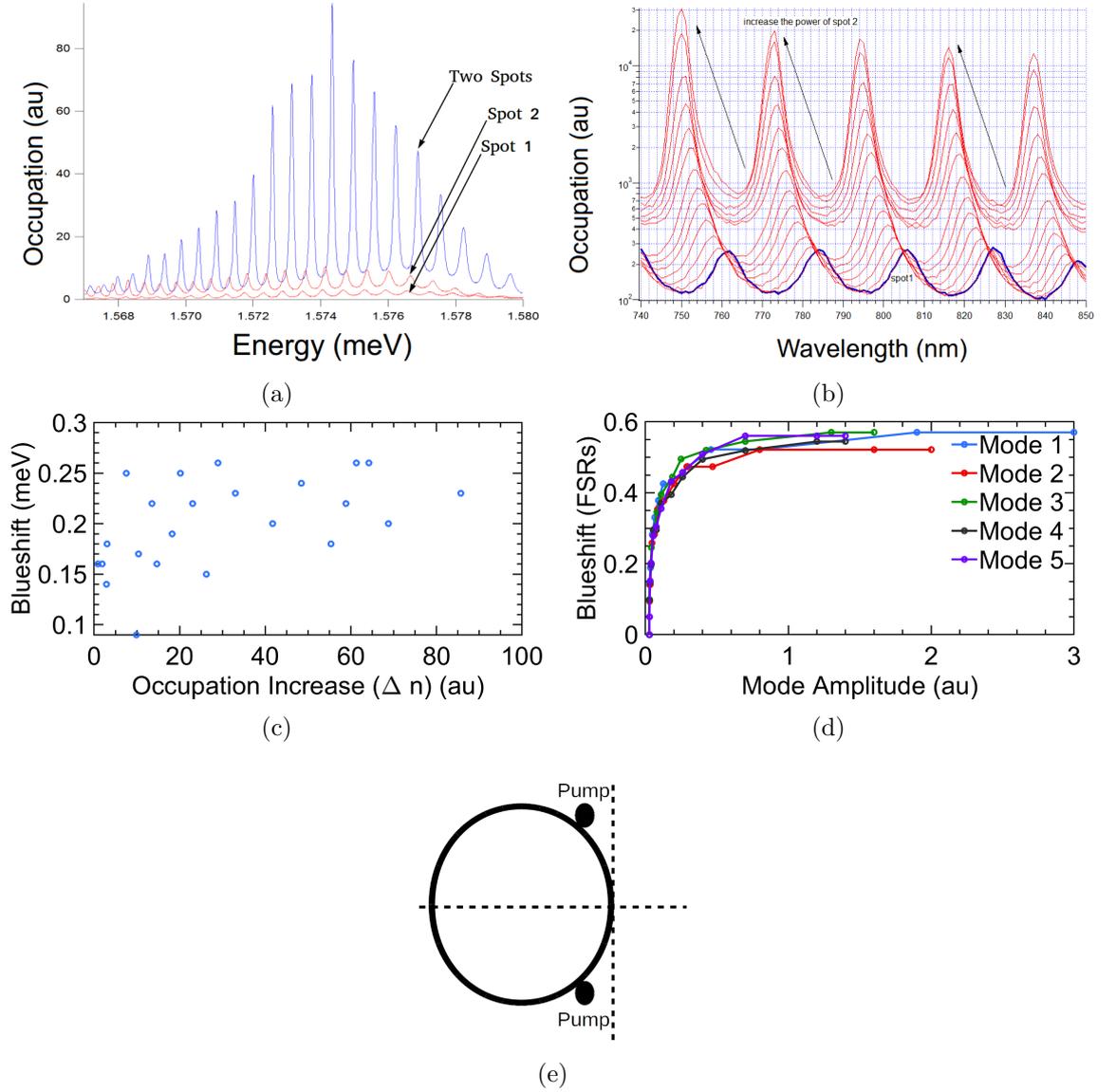
Figure 3.4: Experimental features of polariton WGMs in a circular trap excited with two pump spots. Both pump spots are approximately 2 μm (FWHM) in diameter, and are placed near the trap boundary, 90° apart. A line profile in energy, (a), is created from spectral data as in Figure 3.3 (b). The relative position of the pump spots and slice are shown in (e). From bottom to top, the energy profile with a single spot, the other spot, and then two spots (blue) are shown. With two spots, the peaks are shifted right by approximately half the mode spacing, or free spectral range (FSR), and their heights are increased. A waterfall plot of energy profiles, (b), produced by increasing the power of the second pump spot (from zero until it is equal to the power of the first spot) shows the blueshift increases rapidly with power until it reaches approximately half the FSR. In (d) we plot the dependence of blueshift on peak height (for increasing power of the second pump spot) for each of the peaks shown in (b). In (c) we extract and plot both the blueshift and occupation increase when the second pump spot is added for each peak shown in (a). There is no correlation between the occupation increase and the blueshift.

## 3.4   Theoretical Modelling

### 3.4.1   Whispering Gallery Modes

We consider polariton condensates in a circular trap which is formed by local length-ening of the microcavity, fabricated with an etch-and-overgrowth technique [23]. Since lengthening induces a potential for photons, the most rigorous approach to this system is to compute the trapped photon modes and then couple them to plane wave excitons to find new polariton modes [27]. A simpler approach is to assume that the lengthening simply induces an effective potential for polaritons, whose height is easily estimated experimentally from the energy shift of the lower polariton state in the planar region compared to that in a large mesa (approximately $100\,\mu$m in diameter). A further refinement on this approximation would be accounting for the difference in effective mass inside and outside the trap. Cavity lengthening changes the detuning and hence effective mass. We will see that these approximations are justified - this simplified model accurately predicts the energies of WGMs.

We first study the single-particle states by neglecting nonlinearity and both loss and gain. With these approximations, the ODGPE, Equation (1.20) reduces to a Schrödinger equation for a single-particle wavefunction in circular potential. Converting to radial coordinates, $(r, \theta)$, and assuming a separable wavefunction, $\psi(r, \theta) = R(r)Y(\theta)$, where the radial wavefunction, $R(r)$, is further rescaled as $R(r) = u(r)/\sqrt{r}$, yields [81, 122, 143]

$$-\frac{\hbar^2}{2m}u''(r) + \left(V(r) + \frac{\hbar^2}{2m}\frac{1}{r^2}\left(l^2 - \frac{1}{4}\right)\right)u(r) = Eu(r), \qquad (3.11)$$

and

$$Y''(\theta) = -l^2 Y(\theta), \qquad (3.12)$$

where $E$ is the energy of the WGM, $l$ is the azimuthal quantum number (orbital angular momentum), and $m$ is the effective mass of the lower polariton. The angular dependence, Equation (3.12) is easily solved as

$$Y(\theta) = a\exp(il\theta) + b\exp(-il\theta). \qquad (3.13)$$

The rotational symmetry implies periodic boundary conditions, so $l$ takes integer values, resulting in a discrete set of mode energies. The term $a\exp(il\theta)$ in Equation (3.13) represents a travelling wave that propagates in the clockwise direction, and which has an azimuthally uniform position density. The second term represents a travelling wave that propagates in the counterclockwise direction. When $a$ and $b$ are both nonzero, interference between the travelling waves results in a standing wave, with $2l$ antinodes.

Equation (3.11) is simply a one-dimensional Schrödinger equation with a potential, $V_{\text{eff}} = V(r) + \frac{\hbar^2}{2m}\frac{1}{r^2}\left(l^2 - \frac{1}{4}\right)$. The second term can be interpreted as an effective centrifugal potential that increases with $l$. Combined with an external barrier potential, this results in an effective potential with a local minimum near the barrier, as illustrated in Figure 3.5. Because of the local minimum, WGMs are confined near the barrier. Equation (3.11) is easily solved numerically, for example by deriving and solving a

transcendental equation from matching boundary conditions [143], or by the shooting method [144]. If a transcendental equation is solved, the computed energies can be verified to arbitrary accuracy.

To model the experiment we consider a circular step potential,

$$V(r) = \begin{cases} 0, & r < r_0 \\ V_0, & r \geq r_0 \end{cases}, \tag{3.14}$$

where $V_0 = 5.1\,\text{meV}$ and $r_0 = 10\,\mu\text{m}$.

### 3.4.2   Linear Theory

To find the energies of WGMs we solve Equation (3.11) for a given value of $l$ using a simple direct multiple shooting method [144], although more advanced shooting methods specially adapted to the radial Schrödinger equation are also available [145]. Shooting methods are a class of numerical techniques that solve boundary value problems by reducing them to initial value problems [144]. The initial value problem is solved with varying initial conditions until a solution which matches the boundary value is found. The variation of the initial conditions is typically formalised as a root-finding or optimisation problem, which can be solved with well-known techniques such as Newton's method. The boundary value problem to be solved is often also an eigenvalue problem. In this case, the trial eigenvalue is optimised for agreement with the boundary conditions. The trial eigenvalue is reflected in both the initial conditions and the equation of the initial value problem. A simple refinement is the direct multiple shooting method, in which the initial value problem is solved on several smaller domains, and solutions are optimised for continuity at the boundary between the subdomains as well as agreement with the boundary conditions. This technique is especially useful for problems with discontinuities, such as the external step potential in our system. The discontinuity is naturally handled by matching at the point of discontinuity.

For a given guess of the energy, we integrate Equation (3.11) forwards from $r \approx 0$ and backwards from $r \gg r_0$ to $r_0$, matching at the location of the potential barrier, $r_0$. The initial conditions for integration are readily derived from the asymptotic forms of Equation (3.11) for small and large values of $r$. We use Newton's method to optimise the trial energy for continuity of the wavefunction and its derivative at $r_0$. Continuity indicates that the correct energy has been found[1]. Because this method comprises only numerical integration of a one-dimensional linear differential equation and root finding, convergence is easily confirmed. Moreover, as we discuss below, nearly-exact analytical expressions for the bound states are also available for comparison. We present some computed wavefunctions in Figure 3.5. As is well known for shooting methods, it is vital to integrate backwards from $r \gg r_0$ outside the mesa rather than in the other direction. This suppresses the unbound solution that would otherwise grow exponentially with $r$. The shooting method is easily adapted to account for the difference in effective mass

---

[1]Because the radial Shröedinger equation is a linear differential equation, we are free to multiply solutions (and their derivatives) by a fixed scaling factor. We therefore scale the left solution (and its derivative) to enforce continuity of the wavefunctions at the boundary, and optimise energy to minimise the difference between the derivatives.
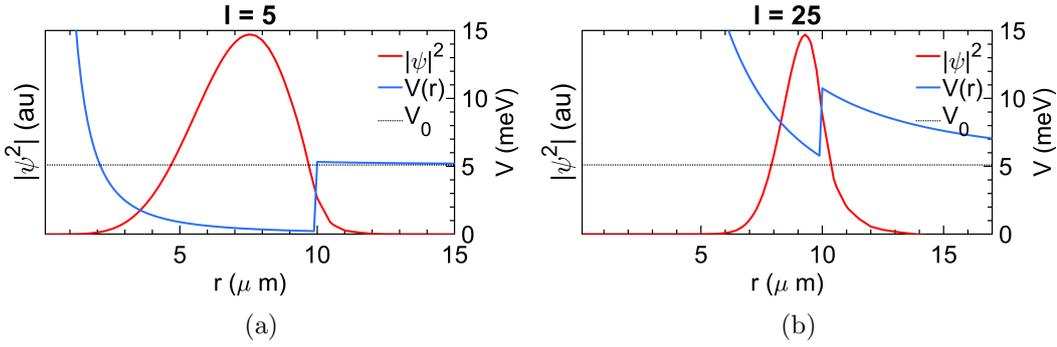
Figure 3.5: Radial wavefunction $\psi(r)$ and effective potential for: (a) $l = 5$, (b) $l = 25$ for the potential in Equation (3.14). The effective potential consists of a finite square well potential and a centrifugal potential that arises from the circular geometry. The combination localises the radial wavefunction near the edge of the barrier.

inside and outside the mesa, but we find this is not necessary in practice. Because we are interested in comparing the computed mode energies to those in the experiment, the lower polariton energy must be subtracted from the experimental data. The lower polariton energy and also effective mass can be measured experimentally by fitting the parabolic part of the free polariton dispersion curve, but we treat both the effective mass and lower polariton energy as fitting parameters and also optimise them for best fit with the experimental data. Our values agree well with the experimental ones.

The numerical and analytic results are shown alongside the experimental data in Figure 3.6. Energies of the bound states, which lie below the potential barrier are also
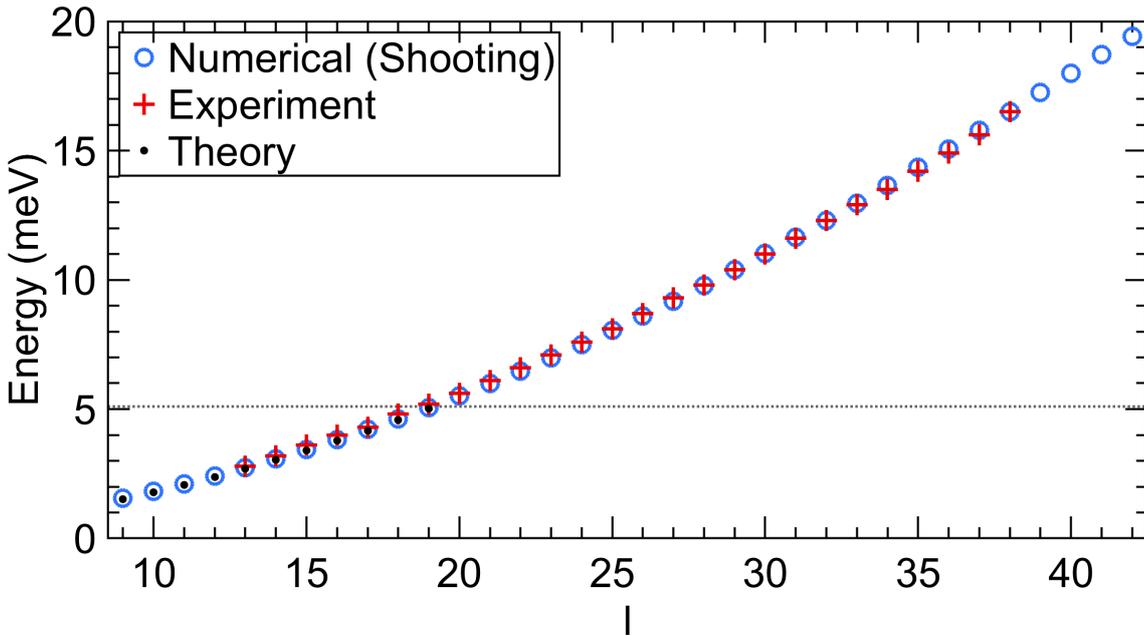


Figure 3.6: Experimental WMG energies for WGMs with increasing azimuthal quantum number, $l$, compared to shooting method calculations. Bound state energies computed with the analytic expressions given in [146] are also shown.

shown. These are calculated using analytic expressions based on approximations to the transcendental equations that arise from matching at the boundary of the trap [146]. We find that the linear theory closely matches both the experimental results and the bound state energies computed with analytical formulas. This simple result confirms that the modes observed in the experiment are indeed WGMs. It also shows that it is sufficient to model the local cavity elongation as an effective potential for polaritons. It also demonstrates that the experiment operates in the linear regime since with one pump spot, the experimental mode energies are not blueshifted from their linear counterparts. The lack of blueshift is attributable to the highly photonic detuning used in the experiment, which reduces the polariton-polariton interaction strength which arises from the excitonic part of the polariton wavefunction.

### 3.4.3   Mean Field Simulations

We also solve the time-dependent ODGPE, Equation (1.16) for the potential in Equation (3.14), excited by a $2\,\mu\mathrm{m}$ (FWHM) pump laser spot situated just inside the mesa to faithfully model the time dynamics and nonlinear physics of the system. The ODGPE contains a number of detuning-dependent parameter such as the polariton effective mass, interaction strength and decay rate, as explained in Section 1.2. In some studies these parameters are simply estimated, often using a detuning of zero. Because the photonic detuning in our experiment implies weak nonlinearity, we instead calculate these detuning-dependent parameters. Equation (1.12) shows that the detuning can be inferred from the cavity and polariton effective masses. The first is measured experimentally, and the second is obtained by fitting the linear results as explained in Section 3.4.2. This allows us to compute the ODGPE parameters given estimates of the cavity lifetime, and theoretical best estimate of the exciton-exciton interaction strength [120][2]. A phenomenological momentum-dependant energy-damping term, given in momentum space by

$$\left.\frac{\mathrm{d}\tilde{\psi}(\mathbf{k},t)}{\mathrm{d}t}\right|_{\mathrm{relax}} = -A|\mathbf{k}|^3\tilde{\psi}(\mathbf{k},t), \qquad (3.15)$$

where the parameter $A$ models the strength of the relaxation, is added to Equation (1.16). This both models the energy relaxation of polaritons and suppresses the modulational instability of the ODGPE [17, 114, 150]. We also add a small noise term to the reservoir equation,

$$\mathrm{d}n(\mathbf{r},t)|_{\mathrm{noise}} = \alpha n(\mathbf{r},t)\mathrm{d}n, \qquad (3.16)$$

where the parameter $\alpha$ models the strength of the noise, and $\mathrm{d}n$ is a stochastic variable, to model thermal fluctuations and quantum noise caused by scattering into the condensate and decay [151].

The ODGPE is readily solved with a standard split-step (Fourier) method [152], in which time evolution is split into small steps, and each time step is split into a linear part and a nonlinear part. The linear part of the time evolution is performed in the Fourier domain and the nonlinear part is performed in the time domain. More specifically,

---

[2]This has been the subject of some recent debate [147], but current consensus is that the theoretical estimate is correct [148, 149].

split-step methods are used to solve PDEs of the form

$$\partial_t u(x,t) = (A+B)u(x,t), \tag{3.17}$$

where $A$ and $B$ are operators, when the split equations

$$\partial_t u(x,t) = Au(x,t)$$
$$\partial_t u(x,t) = Bu(x,t) \tag{3.18}$$

are simpler to solve. The solution to equation (3.17) after a small time $h$ is approximately given by

$$u(x,h) \approx e^{h(A+B)}u(x,0) \approx e^{hA}e^{hB}u(x,0), \tag{3.19}$$

where the second step incurs an error on the order of $h^2$ if $A$ and $B$ do not commute. A number of splitting schemes are possible. For example the splitting

$$e^{h(A+B)}u(x,0) \approx e^{\frac{1}{2}hA}e^{hB}e^{\frac{1}{2}hA} \tag{3.20}$$

is called Strang splitting an incurs an error on the order of $h^3$.

The nonlinear Schrödinger equation is amenable to pseudospectral split-step methods because the Fourier correspondence

$$\partial_x \xrightarrow{\mathcal{F}} ik_x, \tag{3.21}$$

means that the dispersive part is easily handled in the Fourier domain. More concretely, if neglecting the reservoir for the sake of clarity, we write the ODGPE in the form

$$\partial_t \psi = -i\left(D + N[|\psi|^2, n_R]\right)\psi \tag{3.22}$$

where $D = c\nabla^2$, and $N[|\psi|^2, n_R]$ is the remaining nonlinear part, and then split Equation (3.22) as

$$\partial_t \psi = -iD\psi, \tag{3.23}$$
$$\partial_t \psi = -iN[|\psi|^2, n_R]\psi, \tag{3.24}$$

Equation (3.23) is easy to solve in the Fourier domain:

$$\psi(x,h) = \mathcal{F}^{-1}\left[e^{-ichk^2}\mathcal{F}\left[\psi(x,0)\right]\right], \tag{3.25}$$

where $\mathcal{F}$ denotes the Fourier transform. Equation (3.24) can be solved approximately as

$$\psi(x,h) = \exp\left(-ihN[|\psi(x,0)|^2, n_R]\right)\psi(x,0). \tag{3.26}$$

This reasoning is easily adapted to other splitting schemes, and the equation for the reservoir is simple to solve approximately under the approximation that reservoir carriers are almost stationary. Also, more refined methods are available, for example a fourth-order Runge-Kutta method in the interaction picture [153]. A major advantage of the split-step method over finite-difference methods is that it only requires Fourier transforms and elementwise matrix multiplication, both of which are accelerated on modern graphical

processing units (GPUs). A very simple implementation on a GPU gives approximately a hundredfold speed increase over a CPU. Pseudospectral methods also allow for high spatial accuracy despite relatively coarse discretisation grids and large timesteps [152, 154]

One subtlety of this method is that the Fourier periodicity imposes periodic boundary conditions, which means that if the condensate reaches the edges of the integration region it will interfere with itself. We avoid this by using a large integration region relative to the pumping region because the condensate rapidly decays outside the pumping region, and also by multiplying by a window function that ensures the condensate density is equal to zero at the boundaries of the integration region. The conventional Gross-Pitaevskii equation possesses a number of conserved quantities that can be used to validate numerical solutions, but the non-Hermitian nature of the ODGPE means that these quantities are no longer conserved. However, two simple considerations allow us to maintain the validity of numerical solutions. The discrete Fourier transform imposes a Nyquist limit on the maximum momentum that can be resolved. To ensure this is not a problem we record the momentum-space wavefunction and ensure that there is not significant occupation near the Nyquist momentum. Also, the timestep must be small enough that the integration scheme remains numerically stable. Determining the numerical stability of split-step methods as applied to the ODGPE is not trivial. However, numerical instability of split-step methods is known to manifest as rapid growth in only a few Fourier modes [152], which can be identified by monitoring the momentum-space wavefunction. Finally, we can compare the energies of WGMs identified in numerical simulation to those calculated in Section 3.4.2, and monitor the mean-field energy, which is given by

$$\mu(t) = -\frac{1}{4} \frac{\int \left[\nabla^2 |\psi|^2 - 2|\nabla\psi|^2 - 4g_C|\psi|^2\right] dr}{\int |\psi|^2 dr}. \tag{3.27}$$

We perform calculations on a $50\,\mu\text{m} \times 50\,\mu\text{m}$ grid (for a mesa with radius $10\,\mu\text{m}$) with 512 grid points in each dimension with a timestep of approximately $0.03\,\text{ps}$. This timestep is set by the desired spectral energy resolution and is more than sufficient to ensure numerical stability.

The solution of the ODGPE is a record of the order parameter, $\psi(\mathbf{r}, t)$, as a function of time. To compare with the experiment, we must identify WGMs and identify their azimuthal quantum numbers, as well as infer their energies. This is easily accomplished with spectral filtering. To generate a spectrum, we select a time interval and then record the wavefunction at each time step in this interval. Aggregating these time-slices in an array and then taking a Fourier transform along the time axis produces energy-resolved wavefunction slices from the original time-resolved data. To compare with the experimental spectra, we spatially filter out all but a narrow strip of the wavefunction which is offset $90°$ from the pump spot. This produces a spatially-resolved energy profile, as shown in Figure 3.7. A discrete set of energies strongly localised to the mesa edge are clearly visible, which correspond to WGMs. To verify this, we return to the energy-resolved wavefunctions and extract a spatial distribution, $\psi(\mathbf{r}, E)$, at the relevant energy. We present an example of such an energy-resolved wavefunction in Figure 3.8. The phase and spatial distributions of the filtered wavefunctions near the barrier are identical to that of a WGM. Counting the lobes the spatial distribution or the dislocations in the phase distribution allows us to infer the azimuthal quantum number, $l$, of the WGMs, and this
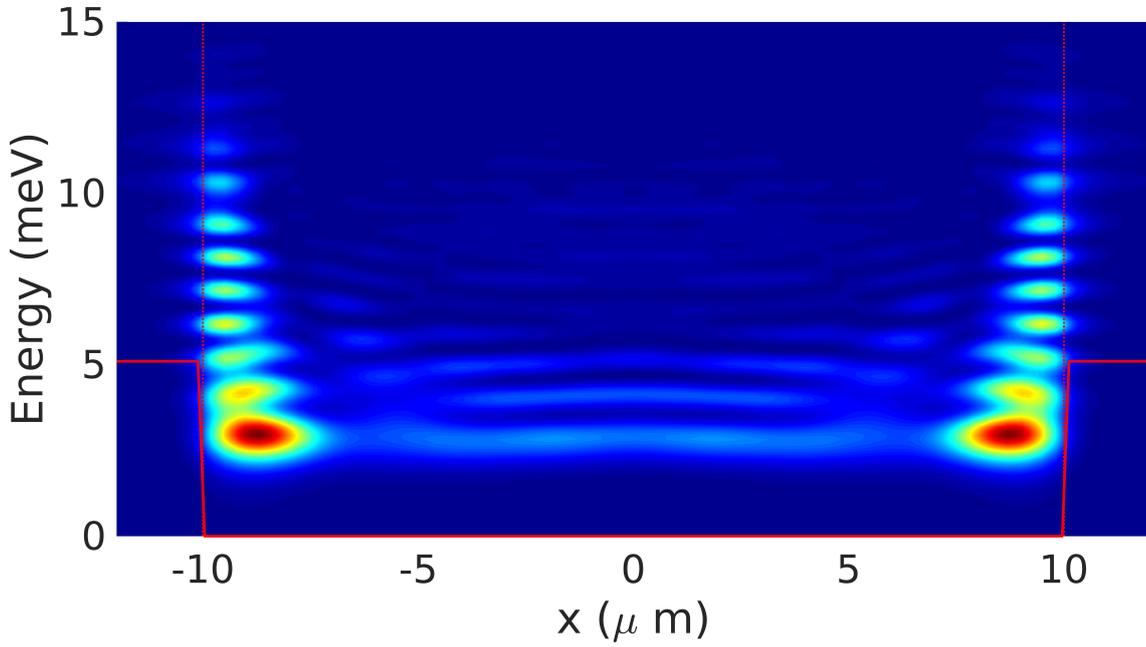
Figure 3.7: Spatially-resolved spectrum extracted from ODGPE simulations. The edge of the trap is located at $x = 10\,\mu$m, and the depth of the trap is $5.1\,$meV. Several WGMs are apparent, indicated by the discrete energies and spatial localisation near the edge of the trap. Note that WGMs are present up to energies of ~$30\,$meV, but are not visible in the image because the low-energy modes are much more strongly occupied.
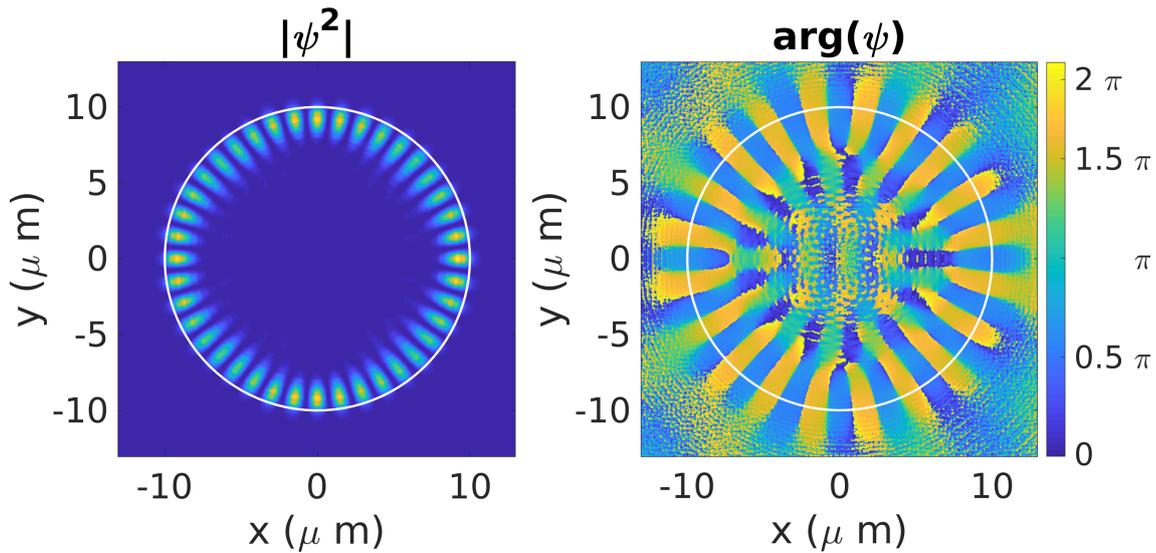


Figure 3.8: Filtered wavefunction for the $l = 20$ mode with $E = 5.58\,$meV extracted from the ODGPE simulation. The value of $l$ can be extracted by counting peaks in the density the phase steps.
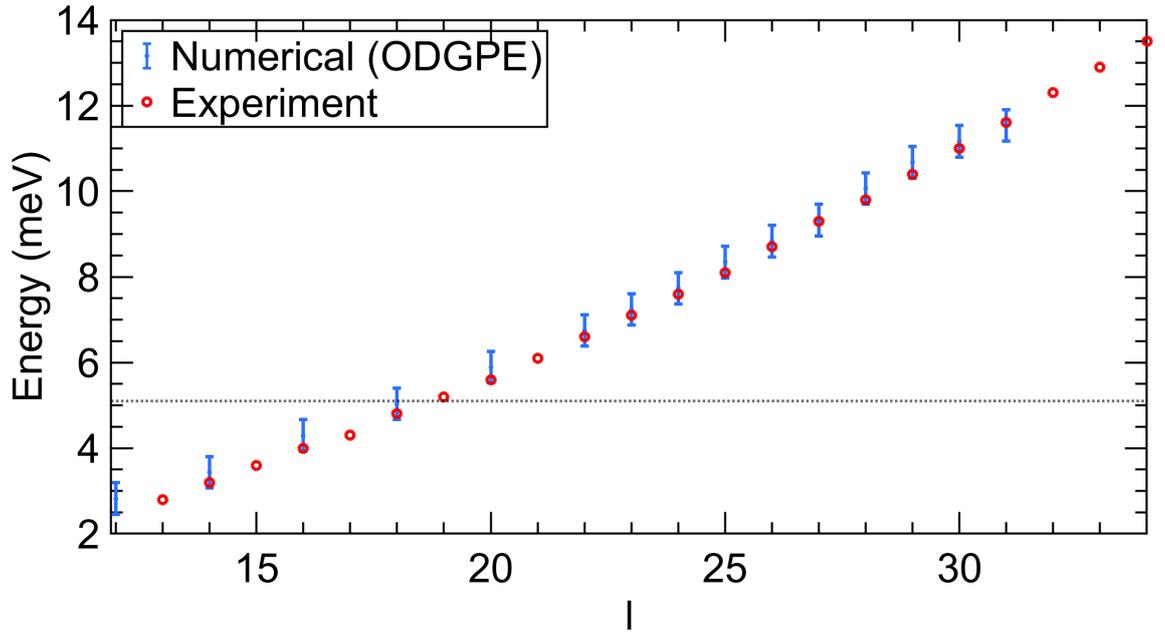
Figure 3.9: Experimental WGM energies and WGM energies extracted from ODGPE simulations. Error bars in the simulation results arise from the nonzero linewidths of WGMs in the simulation. This linewidth is set both by the intrinsic linewidth of the state, and the spectral integration time. We see close agreement between experiment and the simulation. The small discrepancy is due to polariton-polariton interactions, which blueshifts the numerically computed energies as easily verified by setting $g_C = 0$ in the simulation. Note that at lower energy, only every second mode is occupied in the simulation. This behaviour is still not understood, but it is certainly related to the pumping configuration as the threshold for full occupation is changed by moving the pump laser spot relative to the trap edge. Also, it mostly affects modes with energies below the trapping potential barrier.

task is easily automated. We next consider all the states from Figure 3.7 and compute the azimuthal quantum number, $l$, of the WGMs corresponding to each peak. These values, alongside the experimentally observed values and the linear results from Section 3.4.2 are plotted in Figure 3.9. It is clear that the experimental results are reproduced by simulations of the mean-field model.

There is a small discrepancy in that the energies from mean-field simulations are consistently slightly larger than those observed in the experiment. These discrepancies are explained by the nonlinear polariton-polariton interaction, which is easily confirmed by setting $g_C = 0$ in the simulation. With no interactions, our simulated energies match exactly the experimental energies. It is likely that our simulation parameters result in condensate densities somewhat higher than those in the experiment. It is difficult to exactly reproduce population densities because the ODGPE treats phenomenologically both relaxation from free carriers to reservoir polaritons, and stimulated scattering from reservoir polaritons to condensate polaritons. It is not possible to correlate exactly the experimental pump laser power with the reservoir injection rate $P(r)$ in the reservoir equation of Equation (1.16). The latter accounts for the efficiency of *all* of the energy relaxation processes that take free carriers to the reservoir population. Moreover, the stimulated scattering rate, $R$, that models the conversion of reservoir polaritons is purely phenomenological in this model. In fact, when exact population dynamics are important, for example in modelling pulsed experiments, it is normal to resort to phenomenological dual-reservoir models to overcome the difficulties in modelling relaxation processes [114, 155]. Refining the simulation, for example by tuning the stimulated scattering rate, $R$, may yield more accurate polariton densities and remove these discrepancies in energy.

These ODGPE simulations probe the time dynamics of the system. Notwithstanding the small discrepancy in mode energies, they demonstrate that population of WGMs by the experimental excitation scheme is adequately described by the ODGPE. It is also worth noting that the numerical solutions of the time-dependent ODGPE give us the opportunity to carefully explore how WGMs are excited because the solutions are resolved in time. However, experimental data are currently lacking on this front, because only CW experiments have been performed. The photoluminescence is effectively averaged over a long collection time of the signal on the camera. Time-resolved data could be obtained with a streak camera under pulsed excitation [30].

### 3.4.4   Pairs of Nearly-Degenerate Modes

The mean-field simulations also reveal pairs of nearly-degenerate modes which might be brought to degeneracy to realise an EP. As explained in Section 3.2.2, an EP can be reached by coupling pairs of counterpropagating WGMs using external scatterers. The EP is reached when the combination of external scatterers induces completely asymmetrical scattering. A small external pump spot naturally acts as an external scatterer since it induces both a real and an imaginary potential. As shown in Figure 3.10, the peak corresponding to the $l = 23$ WGM in the simulation is split in to three if the pump spot is aligned to the edge of the trap. In (a), a portion of the spectrum taken over an annular slice is shown. Three distinct peaks are apparent, and counting lobes of the

corresponding energy-resolved wavefunctions, shown in (d)-(f) confirms that these three peaks all correspond to a WGM with $l = 23$. Producing one-dimensional spectra by first taking a slice across the trap diameter and then extracting the portion corresponding to $r \approx 10\,\mu\mathrm{m}$, shown in (b)-(c), confirms that there are three distinct peaks[3]. Focusing on the energy-resolved wavefunctions in the vicinity of the pump spot reveals the structure of the states - the lower and middle peaks correspond approximately to the even and odd WGMs, whereas the upper peak is a combination of the two. This is also reflected in the spectrum shown in (a), where we plot vertical lines corresponding to the antinodes of the lower peak.

The structure of the states is further clarified by computing the overlap with travelling-wave WGMs,

$$\alpha_l^{(N)} = \int \psi^{(N)}(\mathbf{r}) R_l(r) r^{il\theta} r\,dr\,d\theta, \qquad (3.28)$$

where $\psi^{(N)}(\mathbf{r})$ is the energy-resolved wavefunction corresponding to the $N^{\mathrm{th}}$ peak, and $R_l(r)$ is the radial wavefunction of the $l^{\mathrm{th}}$ WGM, whose computation is explained in Section 3.4.2 [68]. These overlaps are shown as a function of the WGM azimuthal quantum number, $l$, in Figure 3.11. This reveals that the lower two peaks consist of a combination of propagating and counterpropagating travelling-wave WGMs weighted in favour of the counterpropagating mode. The state corresponding to the upper peak is almost entirely counterpropagating, which is reflected in the reduced contrast of the energy-resolved wavefunction in Figure 3.10 (f) compared to those shown in (d) and (e). A travelling-wave WGM has a position density which is homogeneous in $\theta$ since its wavefunction is of the form $\psi_l(\mathbf{r}) = R_l(r)e^{il\theta}$. Importantly, the peaks in Figure 3.11 (a) corresponding to $l = \pm 23$ for $\alpha^{(1)}$ are both positive, whereas for $\alpha^{(2)}$ one is positive and the other is negative. The same is true for the imaginary parts. This means that a linear combination of the two can correspond to a travelling wave, which implies the fulfilment of the asymmetrical scattering condition for an EP. Such a combination is shown in Figure 3.11 (j)-(l). An EP could therefore be achieved by tuning the coupling of the underlying states with a second pump spot. These results are significant because they demonstrate that an external pump spot can both populate WGMs also induce a coupling between counterpropagating WGMs which could be used to tune the system to an EP.

As explained in Section 3.2.2, EPs of WGMs can also be reached by coupling WGMs to modes with a higher principal quantum number. This is possible because these modes can be naturally nearly degenerate with WGMs, and because coupling can be achieved with a small perturbation to the boundary of a WGMR. Optically-induced potentials for polaritons can be on the order of several meV, which is comparable to the energy depth of traps manufactured with etch-and-overgrowth techniques [26, 27]. Therefore a pump spot focused near the edge of the trap, but mostly inside it effectively causes a small boundary perturbation to the trapping potential seen by polaritons, illustrated in Figure 3.12[4]. This raises the possibility of using the pump-induced potential to couple WGMs to modes with a higher principal quantum number and thereby achieve an EP. In Figure 3.13 (b) we

---

[3]In (c) the slice across the ring diameter must be taken $45°$ from the pump spot to reveal the middle peak.

[4]For the results presented above, the pump spot is focused on the edge of the trap and hence acts as an external scatterer

show the computed linear spectrum including the modes with principal quantum number $n = 2$ as well as the WGMs, which have $n = 1$. This shows that (24, 1) WGM is nearly degenerate with the (20, 2) mode. A one-dimensional spectrum computed from ODGPE simulations reveals two distinct peaks near the corresponding energy, with a splitting that corresponds approximately to the energy difference between the relevant linear modes. Examining the corresponding energy-resolved wavefunctions, shown in (c)-(e) reveals that while the upper peak corresponds to the WGM, the lower peak is a hybridised state consisting of both the WGM and the higher-order mode. The hybridisation implies that the pump spot couples these two modes. It may be possible to tune this coupling by adjusting the position of the pump spot relative to the trap edge, or by adding an additional pump spot. Established perturbation theory for nearly-degenerate modes of circular potentials [140] and numerical techniques for computing eigenstates [135] could provide theoretical guidance.
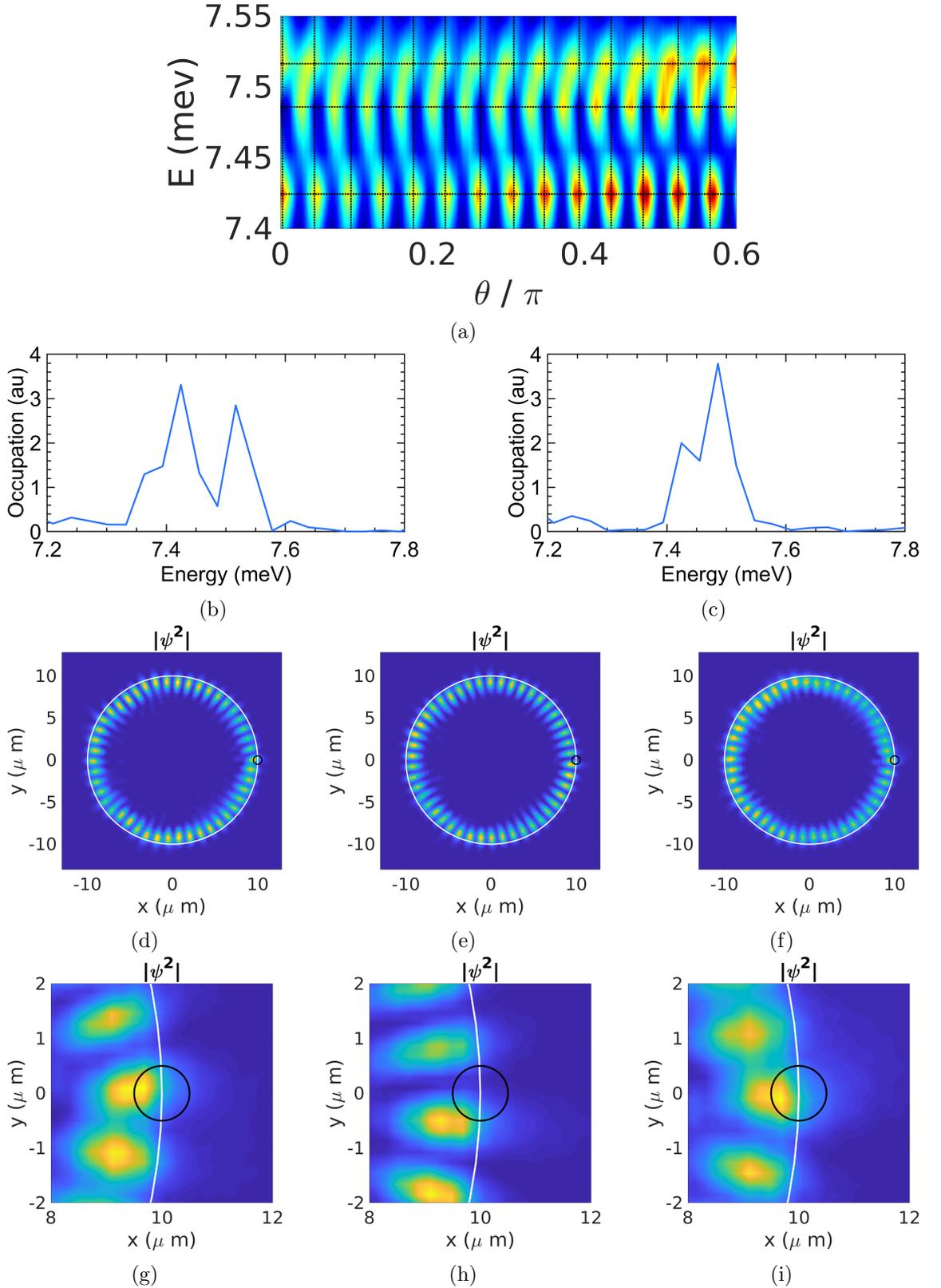
Figure 3.10: Detail of energy splitting caused by a pump spot which acts as an external scatter. A portion of a circular slice of the spectrum taken at the trap radius is shown in (a), revealing three distinct spectral peaks. These are reflected in slices taken across the diameter and resolved near the trap boundary, (b) and (d). The corresponding energy-resolved wavefunctions are shown in (d-f), and are magnified near the pump position in (h-i). The trap boundary is shown in white and the pump location is shown in black. Counting the lobes of the energy-resolved wavefunctions shows that the both correspond to the $l = 23$ mode. The magnified images show that the energy splitting arises from the differing overlaps with the reservoir induced by the pump.
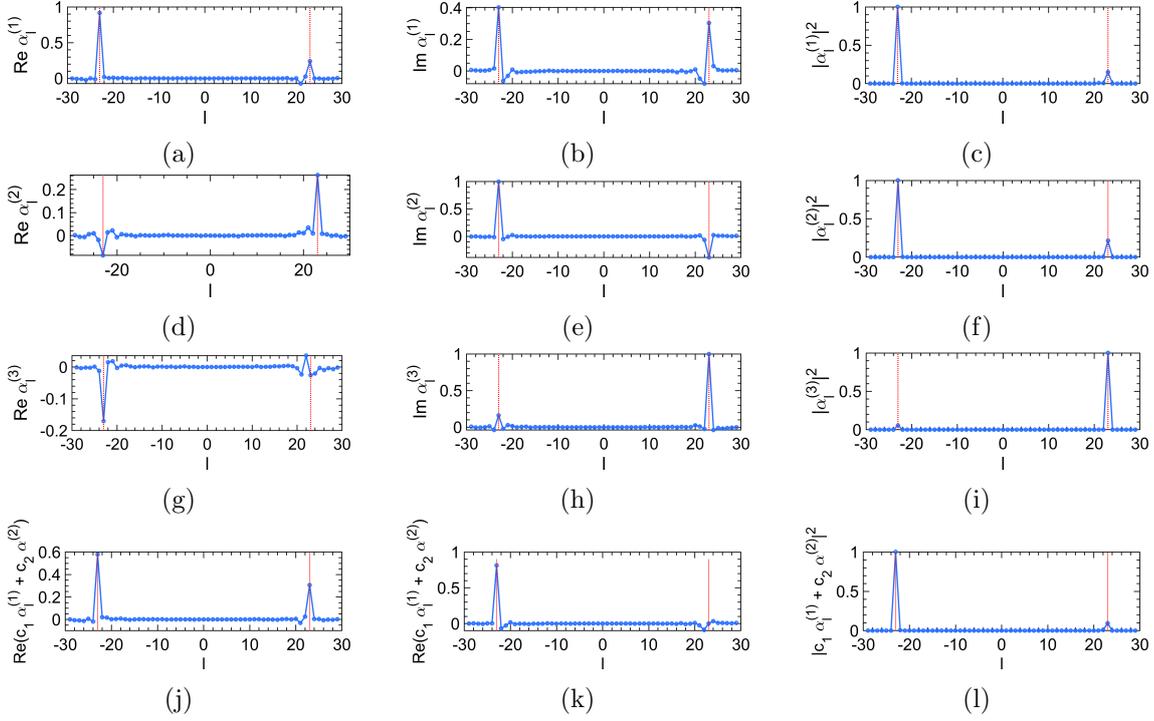
Figure 3.11: Real part, imaginary part and absolute value of the overlaps, $\alpha_l^N$, of the states in Figure 3.10 with WGMs with different azimuthal quantum number, $l$. $N$ increases with energy. In (a-c), $N = 1$, in (d-f), $N = 2$, and in (g-i), $N = 3$. In (j-l), a linear combination of the overlaps corresponding to the lower and middle state, $c_1\alpha_l^{(1)} + c_2\alpha_l^{(2)}$ is shown. Vertical lines corresponding to $l = \pm 23$ are also plotted.
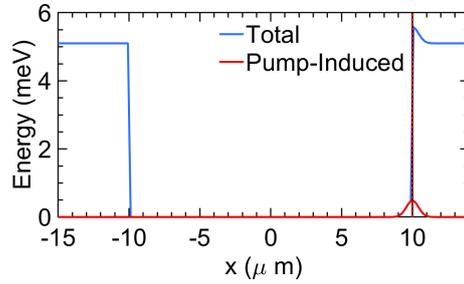


Figure 3.12: Cross section of the total potential experienced by polaritons, taken along a diameter of the trap. The pump spot is focused on the edge of the trap, and slightly deforms the trap boundary. Note that the total potential is no longer radially symmetric. This slice overlaps with the peak of the pump.

(a)

(b)

(c)

(d)

(e)
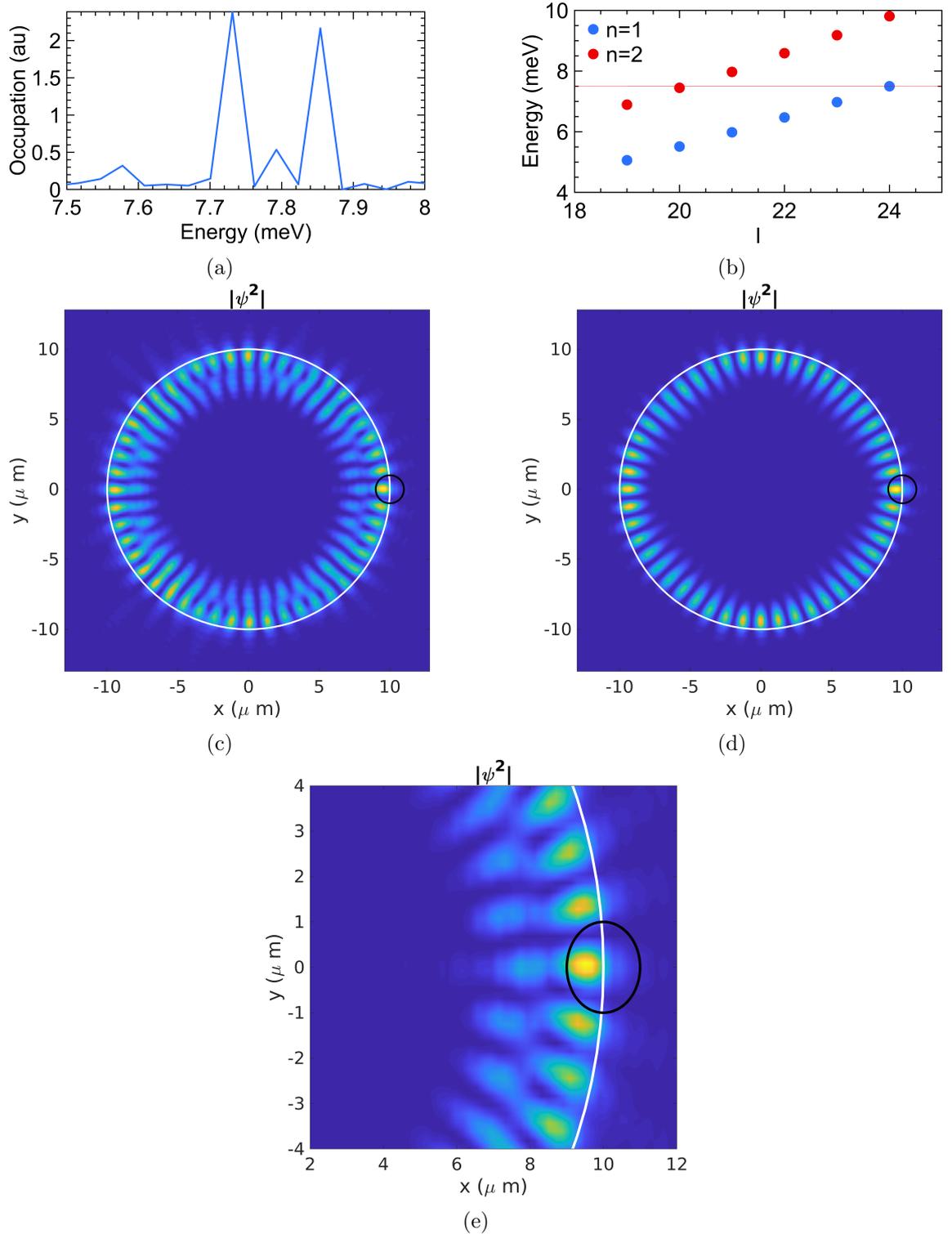
Figure 3.13: Detail of hybridisation between modes with differing principal quantum number. A portion of a slice of the spectrum taken at the trap radius is shown in (a), revealing two distinct spectral peaks at $7.73\,\text{meV}$ and $7.79\,\text{meV}$. The corresponding energy-resolved wavefunctions are shown in (c) and (d). The wavefunction show in (c) is magnified in (e). Counting lobes reveals that the wavefunction shown in (d) corresponds to the $l = 24$ mode, whereas the wavefunction in (c) is a hybrid of this mode, and the higher-order mode which has principal quantum number $n = 2$ and azimuthal quantum number $l = 20$. The linear spectrum computed with the shooting method (see Section 3.4.2) is shown in (b), including $n = 2$ modes. A horizontal line marks the energy of the $(1, 24)$ mode, which is nearly degenerate with the $(2, 20)$ mode. The linear theory predicts an energy difference of approximately $0.05\,\text{meV}$, which closely corresponds to the observed difference of $0.06\,\text{meV}$ in (a).

## 3.5   Excitation With two Pump Spots

### 3.5.1   Theory

One remarkable aspect of the experimental results is the behaviour when a second pump spot is added, illustrated in Figure 3.4. When the power of the second spot is increased, occupation of WGMs increases rapidly, accompanied a blueshift that also increases rapidly and then locks to exactly half a free spectral range. As discussed in Section 3.4.3, our simulated WGMs have an excess blueshift because we are not able to exactly match the polariton densities in the experiment. Because of this existing excess blueshift, we have not been successful in modelling the behaviour with two pump spots in mean-field simulations.

However, we have explored a number of phenomenological models that could account for the behaviour with two pump spots. As explained in Section 3.3, the power used in the one-spot excitation is split between the two pump spots, so the total excitation density with two spots is less than or equal the total excitation density with one spot. Hence the blueshift cannot be attributed to polariton-polariton interactions associated with the increased density. Furthermore, we have shown in Section 3.3 that the blueshift cannot be attributed to polariton-polariton interactions - some other mechanism must be at play.

One possible explanation is a nonlinear resonance, which has already been explored theoretically for WGMs of polaritons in a ring geometry with coherent pumping [133]. In this work, polariton-polariton interactions are shown to result in a nonlinear resonance which causes blueshifts that can exceed the linear FSR. Although coherent excitation of the resonator with a single pump spot was considered, the work is readily adapted to incoherent excitation with two pump spots. The first pump spot simply excites WGMs. Once they are present, the second pump spot can be regarded as a coherent source because it injects polaritons *into the mesa* with a range of wavevectors, many of which match WGMs. The theory also treats photons and excitons independently, but this can be addressed by moving to the polariton basis. We conclude that this theory cannot account for the experimental results because a half FSR blueshift is not favoured. Also, the blueshift depends strongly on the polariton-polariton interaction strength. It is unlikely that the interaction strength in the experiment and the pump powers happens to be exactly the value that yields a half FSR blueshift for every mode. To further confirm this, it would be possible to compare the dependence of blueshift and occupation on pump power predicted by this theory to the experimental dependence shown in Figure 3.4 (d).

We have also considered a theory for coupling of counterpropagating optical WGMs by multiple nanoparticles [67], with the view that a pump spot near the edge of the mesa should have a similar effect to a nanoparticle in an optical WGMR. This theory is explained in Section 3.2.2. The coupling causes a perturbation to the energy, which could result in a blueshift. This theory is readily ruled out for several reasons. The coupling causes a splitting of previously degenerate counterpropagating modes, so two WGMs with the same azimuthal quantum number should be observed at different energies. Also, the splitting depends strongly on the azimuthal quantum number, so it is not possible to achieve a half-FSR blueshift for a large number of WGMs.

Figure 3.14: Schematics of a resonator side-coupled to a waveguide. (a) resonator side-coupled to a waveguide, (b) schematic illustrating how a pair of pump spots form a sector WGM resonator which is side-coupled to WGMs. We may consider the WGMs as waveguide modes because the centripetal potential confines them near the mesa boundary.

The rapid increase in density correlated with blueshift indicates that a resonant effect may be responsible. We conjecture that the arrangement of two pump spots creates an effective non-Hermitian resonator inside the mesa, and that coupling between this resonator and WGMs explains the half-FSR blueshift. Although we introduce this theory in a phenomenological manner, it elegantly explains the experimental observations. In addition, we are able to verify a few assumptions of this theory, demonstrate its robustness, and explain how future experimental and theoretical work will help conclusively verify it.

A theory of coupling between optical waveguides and high Q resonators in the presence of loss and gain has been developed using scattering theory [156]. In the presence of loss and gain, a phenomenon called critical coupling, where the transmission coefficient drops to zero, can occur. In contrast to a resonance, which occurs when the frequency of the waveguide mode matches that of the resonator mode, and the gain of the waveguide mode balances the loss of the resonator mode, critical coupling is reached when the frequency of the resonator mode matches the frequency of the resonator mode, and loss in the waveguide mode also matches that of the resonator mode. This zero of the transmission coefficient has physical consequences, especially for phenomena that depend on its argument. For example, an experiment on optical waveguides coupled to microring resonators demonstrated anomalously large time delays for waveguide wavepackets after scattering mediated by coupling with the microring resonator [157]. The time delays are associated with the zero in the transmission coefficient that occurs at critical coupling.

We propose that the behaviour with two pump spots is also associated with critical coupling in our system. This theory requires a waveguide and a resonator. WMGs are effectively waveguide modes because of the strong radial confinement given by the effective centrifugal potential as explained in Section 3.4.1. In turn, the arrangement of two pump spots inside the mesa creates an effective sector WGM resonator. We explained

in Section 3.4.3, that the optically-induced potential associated with the pump spots is on the order of several meV, sufficient to trap polaritons, and this is supported by multiple experiments [7, 21, 29]. As we will see later, if the pump spots are close to the mesa edge, they create a sector WGM resonator with modes confined near the edge of the mesa, rather than modes which extend across the mesa, as illustrated in Figure 3.14 (b). The resonator modes are consequently very close in energy to whispering gallery modes. The non-Hermitian nature of the resonator and waveguide are of fundamental importance. The waveguide is lossy because of polariton decay, whereas the pump spots impose gain as well as a potential barrier, both of which increase with pump power, so the resonator can experience net loss or gain depending on the pump power. We will first explain how critical coupling causes a half-FSR blueshift, examine how robust this effect is to a small detuning between the resonator and waveguide, provide an account of the resonator modes, and discuss how well this theory explains the experimental results.

The transmission coefficient for waveguide modes when side coupled to a non-Hermitian resonator, shown in Figure 3.14 (a), is given by

$$t = \frac{g + 1 - i\tilde{\Delta}}{g - 1 - i\tilde{\Delta}}, \tag{3.29}$$

where $\tilde{\Delta} = \Delta\omega/\Gamma_C$ is the detuning between the waveguide mode and the resonator mode, $\Delta\omega$, normalised by the decay rate, $\Gamma_C$, of resonator modes due to coupling with the waveguide, and $g = -\Gamma_R/\Gamma_C$ is the intrinsic resonator gain rate, $\Gamma_R$, normalised by the decay rate due to coupling with the waveguide [156]. As we have mentioned, resonance occurs when $\tilde{\Delta} = 0$ and $g = 1$, that is when the waveguide mode is energy degenerate with the resonator mode and the intrinsic gain of the resonator exactly compensates the loss due to coupling with the waveguide. Critical coupling occurs when $\tilde{\Delta} = 0$ and $g = -1$, that is, when the resonator mode is energy degenerate with the resonator mode and the intrinsic loss of the resonator is equal to the loss due to coupling with the waveguide. Note that $\Gamma_C$ is always positive, since coupling to the waveguide modes always induces loss for the resonator. Consequently $g$ is positive when the resonator experiences gain. Our application of the theory is largely phenomenological. There is no clear way to translate between polariton parameters and the loss parameters, $\Gamma_R$ and $\Gamma_C$. Although the theory treats only the coupling of a single waveguide mode (WGM) to a nearby resonator mode, the arguments we make apply for every WGM.

In what follows, we assume that the pump strength sets the resonator gain, and that the detuning and loss due to waveguide coupling remain approximately constant. In reality, the pump imposes a potential as well as gain, which may affect the energies of resonator modes. Our approximation is readily verified. From Equation (1.20), the ratio of the imaginary part of the pump-induced potential to the real part is $\hbar R/2g_R$. For typical polariton parameters[5], this ratio is approximately equal to 5, so changing the pump power primarily increases the gain rather than the real part of the induced potential. That is, the effective resonator is not changed much, and the detuning and loss due to waveguide coupling remain approximately constant, whereas the loss or gain

---

[5]$g_R \approx 10^{-4}$ meVμm$^2$, which corresponds to a very photonic detuning. The parameter $R$ is phenomenological and its value cannot be measured, but $\hbar R \approx 10^{-3}$ meVμm$^2$ is typical of values used to successfully model experiments [7].

changes with the pump strength. As the pump strength is increased, the resonator loss decreases, leading to critical coupling.

We now focus on the WGMs. In the absence of a resonator, the quantisation condition for WGMs is

$$kL = 2l\pi, \tag{3.30}$$

where $L$ is an effective cavity length, approximately the mesa circumference, and $k$ is the wavenumber of the mode. When the waveguide is coupled to a resonator the quantisation condition changes because WGMs acquire extra phase from interaction with the resonator. The quantisation condition then reads

$$kL = 2\pi \left( l + \frac{\arg t}{2\pi} \right), \tag{3.31}$$

where $t$ is the transmission coefficient associated with scattering with the resonator, given by Equation (3.29). We discuss the precise definition of the complex argument in Section 3.5.2. To understand how this affects the energies of WGMs, we can conveniently interpret the quantity $\arg t/2\pi$ as an effective shift to the azimuthal mode number, $l$. If $\arg t/2\pi = 1/2$, then the WGM experiences a blueshift that corresponds to a one-half increase in the azimuthal quantum number. That is, a half-FSR blueshift.

To illustrate how critical coupling causes a half-FSR blueshift, we first consider a degenerate waveguide and resonator, so $\tilde{\Delta} = 0$. The transmission coefficient is then

$$t = \frac{g+1}{g-1}, \tag{3.32}$$

which is purely real. The transmission coefficient has a singularity when $g = 1$. This is the resonance, which is not important to our theory. Instead, we focus on the behaviour near $g = -1$, where the intrinsic loss of the resonator is equal to the loss due to coupling with the waveguide. At $g = -1$, critical coupling occurs. The transmission coefficient is zero, and it changes sign from positive to negative. Because of the change of sign, the argument of $t$ changes rapidly from 0 to $\pi$ across critical coupling. Below critical coupling, $g < -1$, the intrinsic loss of the resonator is greater than loss due to coupling with the waveguide, and waveguide modes experience no blueshift. Above critical coupling, they experience a one-half FSR blueshift due to coupling with the resonator, according to Equation (3.31). Moreover, the transition to one-half FSR blueshift happens instantly when critical coupling is reached. We believe this explains the rapid jump to half-FSR blueshift seen in the experiment. The resonator loss is set by the pump strength which accounts for the pump dependence. The drop in the transmission coefficient near critical coupling may also explain the rapid rise in WGM population. A lower transmission coefficient means waveguide modes - that is WGMs - are more strongly occupied. The dependence of the coupling-induced blueshift and the transmission coefficient on the gain are shown in Figure 3.15. Note that the induced blueshift returns to zero after the resonance is passed.

We now address a few potential discrepancies between the behaviour predicted by this model and experimental observations. In the experiment, WGM population

keeps rising with pump power, whereas the coupling theory predicts that the absolute value of the transmission coefficient will eventually increase with $g$, which should lead to a decrease in the WGM population. However, our theory only applies when the pump strength is sufficient to form an effective resonator. As the pump strength increases the system approaches a regime where the effective resonator model is valid, a result of the real potential induced by the pump, and the effective resonator model approaches critical coupling, a result of the gain induced by the pump. The power dependence observed in the experiment is then primarily caused by the system approaching the regime in which the resonator-waveguide model is valid, rather than by the value of $g$ changing. Since our application of the theory is phenomenological, we are not able to easily infer the loss of the effective resonator from the polariton parameters.

Critical coupling and the jump to a one-half FSR blueshift occurs when $g = -1$, that is when the resonator still experiences net loss. At first glance, net loss seems to be incompatible with the formation of a condensate. However, $g$ is essentially loss for the effective resonator, not for the whole system, so a negative value of $g$ does not preclude the population of WGMs. The pump spots also provide gain for WGMs, and it must be the case that the pumping provides a net gain for WGMs, but is insufficient to provide a net gain for the effective resonator. In fact, this is consistent with the experimental data, which indicate strong occupation of WGMs and not resonator modes, which are confined between the pump spots.
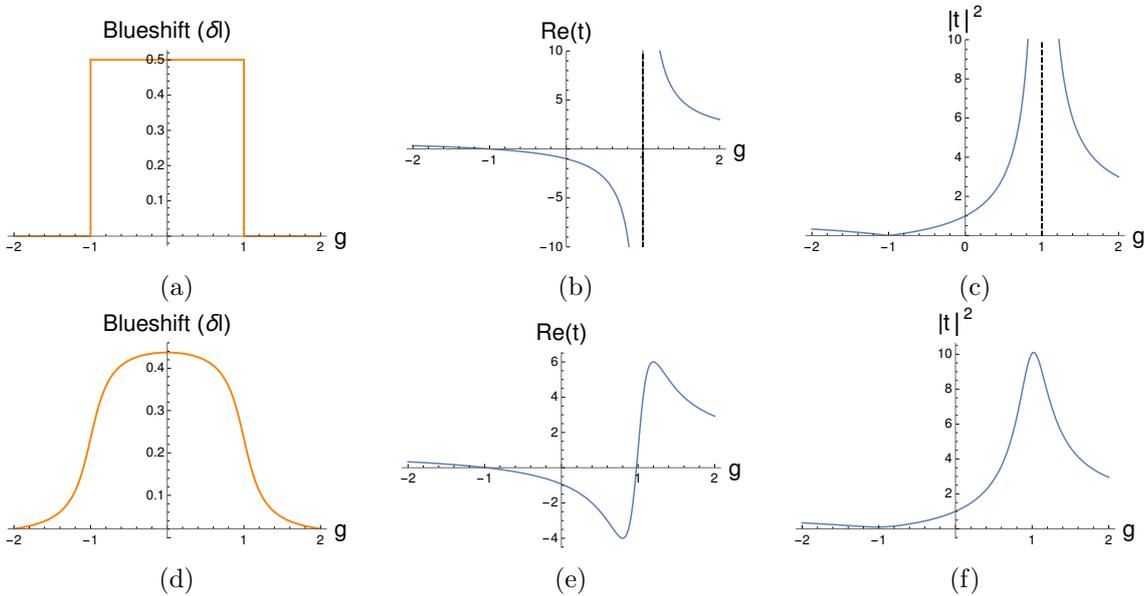


Figure 3.15: Coupling-induced blueshift, real part of transmission coefficient, and modulus of transmission coefficient for $\tilde{\Delta} = 0$ (a-e) and $\tilde{\Delta} = 0.2$ (d-f) of a WGM with azimuthal quantum number $l$. A small detuning shifts the root of the real part of $t$, lowers the maximum blueshift, and smooths the jump in the blueshift. The singularity in $|t|^2$ is also removed.

### 3.5.2 Effect of a Small Detuning

The picture we have presented holds only when the energies of the effective resonator modes exactly match those of WGMs, but this is unlikely to be the case in an experiment. We now examine the effect of a small detuning between the waveguide and resonator mode, and provide a rough estimate of the largest detuning that still allows for a sudden jump to half-FSR blueshift.

With nonzero detuning the transmission coefficient, Equation (3.29), can be written as

$$t = \frac{g^2 - 1 + \tilde{\Delta}^2}{(g - 1)^2 + \tilde{\Delta}^2} - 2i\frac{\tilde{\Delta}}{(g - 1)^2 + \tilde{\Delta}^2}. \tag{3.33}$$

The singularity at $g = 1$ is now removed. That is, resonance cannot be achieved, which is of little consequence to us. To examine how the critical coupling behaviour changes, we need to examine the roots of the real part of $t$. It is easy to see that the roots now occur at $g = \pm\sqrt{1 - \tilde{\Delta}^2} \approx \pm(1 - \tilde{\Delta}^2/2)$. Noting the denominator in Equation (3.33) is always positive, it is easy to see that $\mathrm{Re}(t)$ changes from positive to negative at the smaller root, and from negative to positive at the larger. Hence only the first root can be associated with a jump to a half-FSR blueshift. The second root is associated with resonance. The roots impose an obvious restriction on the magnitude of the detuning. We must have $|\tilde{\Delta}| < 1$ to preserve the smaller root. That is, the detuning must be smaller than the linewidth associated with loss due to coupling with the waveguide. The dependence of $t$ on $g$ for a large detuning is illustrated in Figure 3.15 (d-f). Note that the absolute minimum of $|t|^2$ still occurs at the smaller root of $\mathrm{Re}(t)$, so our arguments about rapid increase in WGM populations near critical coupling still hold. In particular, the magnitude of the drop in $|t|^2$ is relatively unchanged, so the detuning may not affect WGM populations.

The presence of the smaller root is necessary, but not sufficient to preserve the jump to half-FSR blueshift. Because the imaginary part of $t$ is nonzero, $\arg(t)$ will not be exactly equal to 1, and the coupling-induced blueshift will hence not be equal to one-half the FSR. We can easily estimate how small the detuning must be to maintain the half-FSR blueshift. When $\tilde{\Delta}$ is positive, $t$ is in the second quadrant of the complex plane[6], and the blueshift is given by $\pi - \arctan\left(2\tilde{\Delta}/(g^2 - 1 + \tilde{\Delta}^2)\right)$. The coupling-induced blueshift, measured in FSRs is $\frac{1}{2}(1 - \arctan\left(2\tilde{\Delta}/(g^2 - 1 + \tilde{\Delta}^2)\right)/\pi)$. Setting aside for a moment the second root of $\mathrm{Re}(t)$, it is clear that regardless of the value of $\tilde{\Delta}$, the transmission coefficient will be approximately real for large values of $g$, so the half-FSR blueshift is maintained for sufficiently large values of $g$.

To ensure the blueshift is approximately half an FSR, we ask that

---

[6] Note that for fixed $g$, and small values of $\tilde{\Delta}$, the transmission coefficient, $t$ is in the second quadrant when $\tilde{\Delta}$ is positive, and in the third quadrant otherwise. If the principal value of the argument is used, a small change in the detuning from positive to negative would appear to cause a large change in the coupling-induced blueshift. Clearly the branch cut of the argument should be chosen so as to ensure that the blueshift is continuous. We emphasise that the sudden jump in blueshift associated with critical coupling occurs because the sign of the transmission coefficient changes. It is not associated with a branch cut.
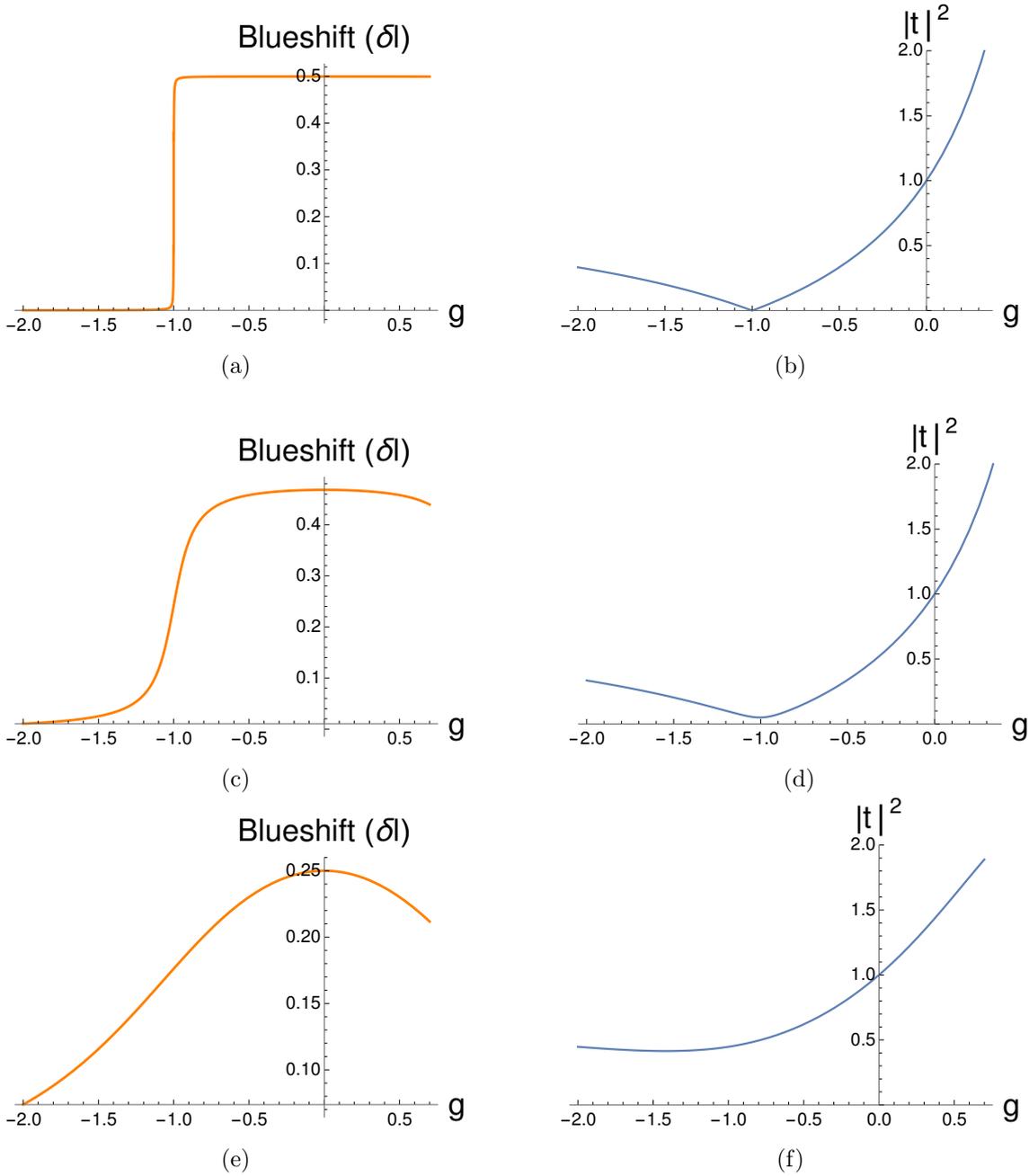
Figure 3.16: (a, c, e) dependence of coupling-induced blueshift, and (b, d, f )transmission coefficient on $g$ for a WGM with azimuthal quantum number $l$. Blueshift is plotted in terms of $l$. Detuning is $\tilde{\Delta} = 0.001$ in (a) and (b), $\tilde{\Delta} = 0.01$ in (c) and (d), and $\tilde{\Delta} = 0.1$ in (e) and (f).

$\arctan\left(2\tilde{\Delta}/|g^2 - 1 + \tilde{\Delta}^2|\right) < \epsilon\pi$. For example, choosing $\epsilon = 0.2$ will guarantee that the blueshift is at least 0.4 FSRs. Linearising, we get $2\tilde{\Delta}|g^2 - 1| < \tan(\epsilon\pi)$. The bound on $\tilde{\Delta}$ depends on $g$, and is looser for larger values of $g$. As we have explained, the transmission coefficient is always approximately real for large $g$. Of course, $g$ cannot be arbitrarily large because the blueshift is lost after the resonance, which occurs at the larger root of $\mathrm{Re}(t)$. Although it is not possible to determine the value of $g$ in the experiment, it is reasonable to set $g = 0$ in the inequality. Since this is exactly halfway between the two roots, we are asking that the blueshift reaches approximately half an FSR well before the resonance is reached. With $\epsilon = 0.2$, we get $\tilde{\Delta} < 0.1$. However, $\tilde{\Delta} = \Delta\omega/\Gamma_C$ depends on the resonator loss due to coupling with the waveguide, and this cannot easily be computed. If we approximate $\Gamma_C$ by the polariton decay rate, $\gamma_C$, which is on the order of $10^{-1}\,\mathrm{ps}^{-1}$ we see the detuning should be on the order of $10^{-2}\,\mathrm{meV}$. Although the polariton decay rate is the only other intrinsic loss rate in the system, it is likely to be a poor estimate of the coupling loss. We expect the coupling loss to be much lower than the polariton decay rate, which will relax the bound on $\tilde{\Delta}$. In Figure 3.16 we show the coupling-induced blueshift and transmission coefficient for various values of $\tilde{\Delta}$, confirming that $\tilde{\Delta} < 0.1$ is sufficient to ensure that the coupling-induced blueshift reaches half an FSR. We also note that the dip in $|t|^2$ is preserved for moderate detuning, so WGMs should be populated and resonator modes will not be populated. Since the transmission coefficient does not change substantially with $\tilde{\Delta}$, the detuning will not affect the population of WGMs.

### 3.5.3   Effective Resonator

Our explanation hinges on the hypothesis that the arrangement of two pump spots creates an effective resonator whose modes are close in energy to WGMs. In this section we provide a simple model of the effective resonator created by the real part of the pump-induced potential, and show that the energies of its modes are close to those of the WGMs. However, we are still not able to infer the intrinsic loss of the effective resonator, nor the loss induced by coupling with WGMs.

The pump-induced potential is on the order of several meV [21, 29], which is approximately equal to the potential barrier responsible for the trapping of WGMs. Since the pump spots are close to the edge of the mesa, we can model the effective resonator as a *sector* WGM resonator, shown in Figure 3.14 (b). A sector resonator approximation of a notched WGM resonator has also been used to explain mode selection in electrically-driven quantum dot microring cavities [158].

The theoretical treatment of a sector WGM resonator differs little from a normal WGM resonator [159]. After separation of variables as in Section 3.4.1, the angular quantisation condition is $Y(0) = Y(\theta_0)$, where $Y(\theta)$ is the angular wavefunction and $\theta_0$ is the angular size of the resonator. The azimuthal quantum number is hence quantised as $l = 2\pi n/\theta_0$, as opposed to $l = n$ for a full WGM resonator. Given a value of $l$, the mode energies are easily computed by numerically solving for the radial wavefunction as in Section 3.4.1. The energy is a continuous function of $l$, so we can view sector
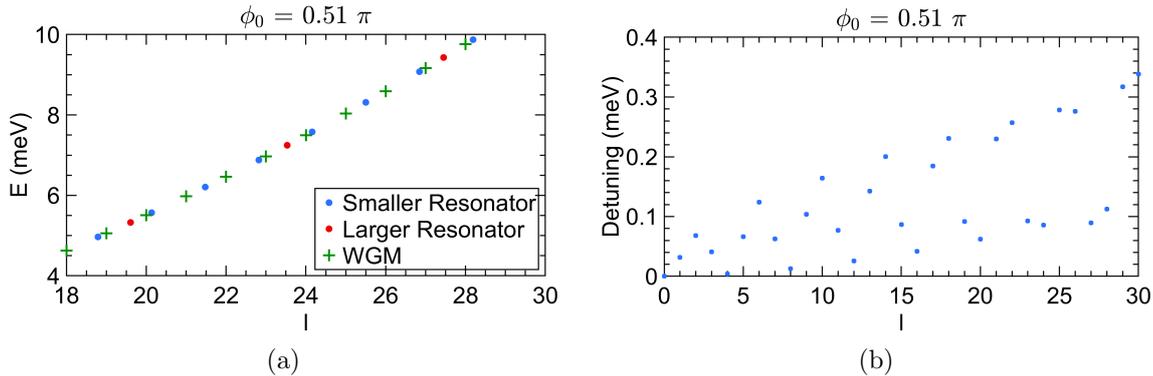
Figure 3.17: (a): Energies of the modes of the effective sector resonator formed by the two pump spots, (b): detuning from Whispering Gallery Modes. The angle between the pump spots is $0.51\pi$.

WGMs as WGMs with a non-integer value of $l$, and consequently a different energy. The arrangement of two pump spots actually creates two sector resonators, one with angular size $\theta_0$, and the other with angular size $2\pi - \theta_0$.

In the experiment the angle between the pump spots is approximately $\pi/2$. With $\theta_0 = \pi/2$, the two effective resonators are identical and the azimuthal quantum number for sector resonator modes is given by $l = 4n$, so the sector resonator simply supports every fourth WGM. This means that the detuning between resonator modes and WGMs is either zero or substantial - several FSRs, so it is not assured that every has a resonator mode close enough in energy to cause a half FSR blueshift.

In reality, the angle between the pump spots will not be exactly $\pi/2$ because the alignment of the laser cannot be controlled with sufficient precision. As shown in Figure 3.17, a small deviation from $\theta_0 = \pi/2$ actually results in many resonator modes being close in energy to WGMs. This is simply because the two effective resonators now have different angular sizes. Clearly the detuning from resonator modes varies between different WGMs, but we have shown that this should not strongly affect the population of different WGMs. In addition, since the blueshift does not depend strongly on the resonator-waveguide detuning, different WGMs may experience the same coupling blueshift despite the different detuning. Besides, the resonator loss due to coupling may be so large and the normalised detuning hence so small that this variation does not matter.

We have also investigated the dependence of the detuning on the angle between the pump spots. For each angular size of the effective resonator we compute the detuning of each WGM from the sector resonator mode closest in energy. It is clear that regardless of the angle between the pump spots, most WGMs have $\tilde{\Delta} \lesssim 0.1\,\mathrm{meV}$, and the maximum detuning of any WGM is on the order of $0.5\,\mathrm{meV}$. These detunings are several times larger than the bound we derived in Section 3.5.2, but still within an order of magnitude. As we explained, this bound depends on the loss experienced by the effective resonator due to coupling with the waveguide, and this is difficult to estimate. We expect that our estimate is too high, and the bound is looser than we have computed, so the detunings should fall well within the true bound. We

have hence shown that the WGMs may be sufficiently close in energy to the modes of the resonator to maintain the jump to half-FSR blueshift. In addition, we have shown that the maximum detuning does not depend strongly on the angle between the pump spots. It should be possible to observe the same effect for any angle between the pump spots, which is an important prediction that can be tested with further experiments.
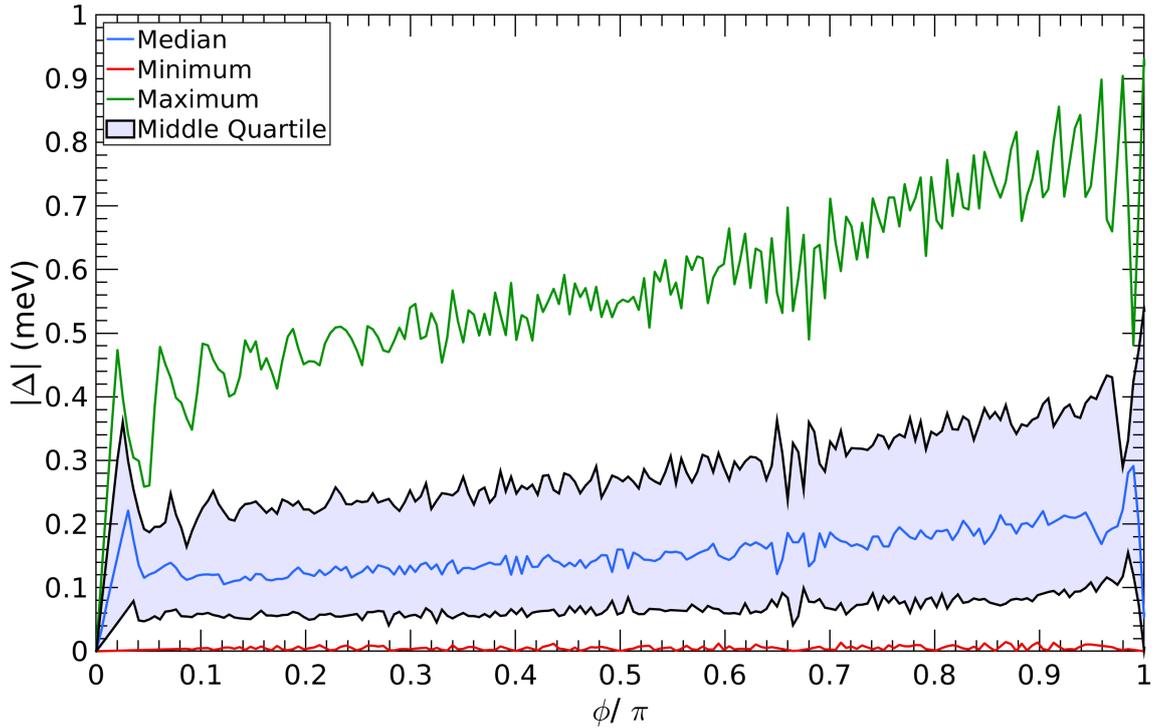


Figure 3.18: Detuning between energies of WGMs and the modes of the effective resonator for different angular separations, $\theta_0$, between the pump spots. For each value of $\theta_0$, we compute the detuning for WGMs with mode numbers between 0 and 50. We plot the maximum and minimum detunings, as well as the median and middle quartile. It is clear that regardless of the angular separation, almost all WGMs are close in energy to a resonator mode. In fact, the most extreme detunings are likely still small enough to guarantee a coupling-induced blueshift equal to half a free spectral range. Note that the dependence is symmetrical around $\theta_0 = \pi$ due to the formation of two effective sector resonators with angular separation $\theta_0$ and $2\pi - \theta_0$.

Demonstrating coupling-induced blueshift for only a few modes that have a sufficiently small detuning from resonator modes, as opposed to all modes, would be compelling evidence for our theory. This would best be done by selecting an angle between the pump spots that results in a small detuning for only a subset of WGMs. We have shown that this is likely not possible for the trap we have studied, since most WGMs have only a small detuning from resonator modes regardless of the angle between the pump spots. The dependence of WGM energy on azimuthal quantum number is affected by both the trap size and depth. If this dependence is strong enough, it may be possible to achieve detunings large enough that not all WGMs experience a coupling-induced blueshift. However, work in this direction will have to be supported with firm theoretical estimates of the resonator loss due to coupling with WGMs so that the normalised detuning can be estimated.

## 3.6   Conclusions and Further Work

Motivated by a recent experiment, we have investigated WGMs of polariton condensates confined in a circular trap, which is imprinted by locally lengthening a small part of the optical microcavity during sample manufacture. In the experiment, whispering gallery modes of this potential are excited by shining either one or two pump spots near the edge of the potential. With one spot, many WGMs are excited. When two pump spots are used, the same modes are occupied, but they are blueshifted by exactly half a free spectral range. The power of the second pump spot is varied from zero to equal with the first pump spot, revealing that the blueshift increases rapidly with power, quickly locking to half an FSR. In addition, the population of the modes increases rapidly with the power of the second pump spot. We have shown that the energies of these WGMs can be predicted using simple linear theory - polariton populations are low enough that the WGMs are not blueshifted by polariton-polariton interactions. Moreover, we have used numerical simulations of the time-dependent ODGPE to verify that the pumping scheme excites WGMs.

We have explained the blueshift observed with two pump spots by phenomenologically applying a scattering theory analysis of coupling between a non-Hermitian waveguide and resonator. We treat the WGMs as waveguide modes and assume that the arrangement of two pump spots creates an effective resonator whose intrinsic gain varies with the pump power. WGMs gain phase from the coupling with the resonator, quantified by the argument of the transmission coefficient. This modifies the quantisation condition and hence energies of WGMs. When the detuning between a resonator mode and waveguide mode is zero, the transmission coefficient is purely real, and depends on the intrinsic loss of the resonator, which is set by the gain from the pump. When the intrinsic loss is exactly equal to the loss induced by coupling to waveguide modes, the transmission coefficient is zero, and changes sign from positive to negative. Consequently, its argument jumps rapidly from 0 to $-1$, and this sudden jump explains exactly why every WGM experiences a half-FSR blueshift.

If the resonator mode is slightly detuned from the waveguide mode, the transmission coefficient is complex, the jump in the coupling-induced blueshift is smoothed, and the maximum blueshift is slightly reduced from half an FSR. We have provided bounds on the maximum detuning that preserves a jump to half-FSR blueshift. We have also explained qualitatively how the experimental arrangement of two pump spots creates an effective resonator. With a simple approximation we are able to compute the energies of the modes of this effective resonator, demonstrating that they are likely close enough to those of WGMs to explain the experimental observations. However, a precise comparison is not available because we do not yet have a theoretical estimate of the losses experienced by the effective waveguide.

There is still much scope for further work. Although our mean-field simulations demonstrate that WGMs can be populated by the experimental excitation scheme, we are not able to populate as many WGMs as in the experiment. To address this discrepancy we will likely need to carefully account for energy relaxation processes in our model [17, 160]. It may be possible to adapt work that provides a theoretical treatment of parametric scattering in ZnO microwires [124]. In any case, time-resolved experimental

measurements, rather than the current time-averaged ones will be vital, and will also allow us to compare time dynamics with numerical predictions.

More theoretical and experimental work will allow us to verify our explanation of the blueshift. The scope for experimental work is somewhat limited because optical excitation creates gain and a real potential, and the theory is best tested by varying only the gain of the non-Hermitian resonator. An additional difficulty is that the theory only applies when the real part of the pump-dependent potential is large enough that the spots act as an effective resonator. This places limits on the pump power and hence $g$ in Equation (3.29). Also, the maximum pump power is limited by the damage threshold of the sample. Repeating the measurements at a different photon-exciton detuning may allow us to access different values of $g$ because the stimulated scattering rate and polariton-reservoir interaction strength both depend on the detuning [2], and hence so does the strength of the real part of the pump-induced potential relative to the imaginary part. With a different detuning, the pump will create an effective resonator with a different value of the gain. However, the detuning also effects polariton energy relaxation efficiency [6, 134], and at a different detuning relaxation may be too strong to populate WGMs which have large azimuthal quantum numbers.

The theoretical parameter $g$ is defined as the intrinsic resonator gain normalised by the loss due to coupling with WGMs, but we currently lack a theoretical estimate of the latter. Without this, we are unable to quantify how much $g$ changes with pump power. Establishing a theoretical estimate of this quantity will help us test the theory. In principle, this is possible by adapting the scattering theory [156]. It will be necessary to carefully compute the resonator modes. This could be done by computing the modes of the system accounting for the pump-dependent potential, and identifying which are resonator modes. A pump spot on the mesa boundary could be treated as a boundary deformation. In this case, the boundary element method can be used to exactly compute the modes [135]. However, separating the intrinsic resonator loss from the loss due to coupling with WGMs may still be challenging.

It is simple to independently set the real and imaginary parts of the pump-dependent potential in numerical simulations by choosing the prefactors of the pump-dependent terms after the reservoir is eliminated from the ODGPE (Equation (1.20)). By setting the imaginary part independently, we can control the gain of the effective resonator, which will allow us to make a number of comparisons with theoretical predictions to more robustly demonstrate critical coupling. Filtering in energy will allow us to identify modes of the effective resonator and verify that their occupation drops and then revives through critical coupling. Most importantly, simulations will allow us to investigate large values of $g$, which is not possible in experiment. The maximum pump power, and hence value of $g$, is limited by the damage threshold of the sample. With increasing $g$, the blueshift should drop back to zero. Additionally, as $g$ becomes large enough to approach the resonance, the occupation of resonator modes should increase substantially. Observing resonance would be a crucial piece of evidence to demonstrate both the formation of an effective resonator, and coupling between this resonator and WGMs.

Finally, we have presented some preliminary results that indicate it may be possible to achieve an EP by coupling degenerate counterpropagating WGMs. Using mean-field simulations, we have demonstrated that a laser spot focused on the trap boundary not only populates WGMs, but also induces a small energy splitting between even and odd parity WGMs with the same azimuthal quantum number. We have also shown that it will be possible to achieve a mode with unidirectional propagation, and hence an EP by tuning the coupling between these modes. The obvious next step is to verify, using mean-field simulations that a pair of scatterers can induce an EP. Most importantly, it is necessary to check whether there exists a regime in which a pair of pump spots scatters propagating WGMs sufficiently, but does not lead to the formation of the effective resonator. It will also be necessary to check the sensitivity of this behaviour to the position of the pump spots. Moving the pump spots closer to the resonator boundary will alter the scattering strength, but some movement will be unavoidable in any real experiment due to mechanical vibrations. It may be possible to use the Boundary Element Method developed for optical WGMRs [135] for many of these tasks rather than time-resolved mean field simulations.

We have also presented preliminary evidence of hybridisation of a WGM and a nearly degenerate mode with a higher principal quantum number. This raises the possibility of achieving an EP by coupling these modes. It has already been established that this coupling can be achieved for optical WGMRs by perturbing the resonator boundary. In our case, the potential induced by the pump spot is sufficiently large that a pump spot placed just inside the mesa effectively modifies the resonator boundary. As we have mentioned, a perturbation theory for nearly-degenerate modes of a circular resonator with a perturbed boundary has been developed. It will be straightforward to apply this theory to our system to verify that the pump spots provides a perturbation that is sufficient to induce an EP.

# Conclusions and Further Work

Exciton polaritons are hybrid matter-light quasiparticles that can undergo Bose-Einstein condensation at temperatures as high as room temperature. Because of their hybrid light-matter nature, exciton polariton condensates are an attractive platform for realising optoelectronic devices. In contrast to Bose-Einstein condensates of atoms, exciton polariton BECs are inherently open systems as they experience loss and gain. This loss and gain allows for the exploration of non-Hermitian physics, including PT symmetry and EPs. These effects have been extensively explored in optics but are largely ignored in polariton condensates.

We have investigated a nearly-PT symmetric square well for polariton condensates, which can be created by combining a real potential created using an etch-and-overgrowth technique with an imaginary potential induced by a laser pump. However, such a potential will only be approximately PT symmetric since the fixed polariton loss is combined with a varying gain, and the pump also induces a real potential. Using a linear theory, we have demonstrated that although the asymmetries remove the PT symmetry breaking transition and associated EP, both can be restored by slightly shifting the position of the pump. These results must still be verified with mean-field simulations to account for nonlinearity and population dynamics. Nevertheless, they provide guidance for a future experimental test of some predictions of PT symmetric quantum mechanics in a truly quantum system.

Guided by recent experimental results, we have also investigated WGMs of polaritons in a circular trap. Using a simple linear theory we are able to accurately model the WGM energies, and using mean-field simulations we have verified that these modes are populated by the pumping scheme. We have also provided a phenomenological explanation for the behaviour when excited with two spots. When a second pump spot is added, all of the WGMs experience a one-half FSR blueshift and a large rise in occupation. This can be explained by coupling to an effective resonator formed by the two pump spots. Coupling to this resonator changes the quantisation condition and hence energy of WGMs. In particular, in the vicinity of critical coupling, where the transmission coefficient becomes zero, the argument of the transmission coefficient rapidly changes, causing the sudden jump to a half FSR blueshift. Although we have applied this theory phenomenologically, several key details have been verified. Mean-field simulations will conclusively demonstrate its validity.

Mean-field simulations of the circular trap excited with a single pump spot have also revealed pairs of nearly-degenerate modes that can be coupled to achieve an EP. A pump spot placed outside the trap both populates WGMs and scatters counterpropagating WGMs; it may be possible to tune the scattering using a second pump spot to achieve an EP, an idea which can be explored with further mean field simulations. In contrast a pump spot placed just inside the mesa acts as an effective deformation to the mesa boundary, which can couple WGMs to nearly-degenerate modes with a higher principal quantum number. We have found such a pair of modes with linear simulations, and demonstrated preliminary evidence for their hybridisation in mean-field simulations. A perturbation theory for nearly degenerate modes of circular potentials as well as numerical techniques for computing modes of two-dimensional cavities will help provide theoretical guidance to engineer a pumping scheme that drives these modes to degeneracy. Together, these results are a first step towards future experiments which will demonstrate EPs of polariton WGMs. This would be an exciting result since polaritons are a promising system for new optoelectronic devices, and EPs of optical WGMs have already been used to demonstrate a number of useful effects.

# Bibliography

[1] Hui Deng, Hartmut Haug, and Yoshihisa Yamamoto. Exciton-polariton Bose-Einstein condensation. *Reviews of Modern Physics*, 82(2):1489–1537, may 2010. doi: 10.1103/RevModPhys.82.1489.

[2] J. J. Hopfield. Theory of the Contribution of Excitons to the Complex Dielectric Constant of Crystals. *Physical Review*, 112(5):1555–1567, dec 1958. doi: 10.1103/PhysRev.112.1555.

[3] Yongbao Sun, Patrick Wen, Yoseob Yoon, Gangqiang Liu, Mark Steger, Loren N. Pfeiffer, Ken West, David W. Snoke, and Keith A. Nelson. Bose-Einstein Condensation of Long-Lifetime Polaritons in Thermal Equilibrium. *Physical Review Letters*, 118(1):016602, jan 2017. ISSN 0031-9007. doi: 10.1103/PhysRevLett.118.016602.

[4] I. A. Shelykh, G. Malpuech, and A. V. Kavokin. Bogoliubov theory of Bose-condensates of spinor exciton-polaritons. *physica status solidi (a)*, 202(14):2614–2620, nov 2005. ISSN 1862-6319. doi: 10.1002/pssa.200562000.

[5] J. Kasprzak, M. Richard, S. Kundermann, A. Baas, P. Jeambrun, J. M. J. Keeling, F. M. Marchetti, M. H. Szymańska, R. André, J. L. Staehli, V. Savona, P. B. Littlewood, B. Deveaud, and Le Si Dang. BoseEinstein condensation of exciton polaritons. *Nature*, 443(7110):409–414, sep 2006. ISSN 0028-0836. doi: 10.1038/nature05131.

[6] F. Tassone, C. Piermarocchi, V. Savona, A. Quattropani, and P. Schwendimann. Bottleneck effects in the relaxation and photoluminescence of microcavity polaritons. *Physical Review B*, 56(12):7554–7563, sep 1997. ISSN 0163-1829. doi: 10.1103/PhysRevB.56.7554.

[7] T. Gao, E. Estrecho, K. Y. Bliokh, T. C. H. Liew, M. D. Fraser, S. Brodbeck, M. Kamp, C. Schneider, S. Höfling, Y. Yamamoto, F. Nori, Y. S. Kivshar, A. G. Truscott, R. G. Dall, and E. A. Ostrovskaya. Observation of non-Hermitian degeneracies in a chaotic exciton-polariton billiard. *Nature*, 526(7574):554–558, oct 2015. ISSN 0028-0836. doi: 10.1038/nature15522.

[8] M H Anderson, J R Ensher, M R Matthews, C E Wieman, and E A Cornell. Observation of bose-einstein condensation in a dilute atomic vapor. *Science (New York, N.Y.)*, 269(5221):198–201, jul 1995. ISSN 0036-8075. doi: 10.1126/science.269.5221.198.

[9] Li Ge, Ani Nersisyan, Baris Oztop, and Hakan E. Tureci. Pattern Formation and Strong Nonlinear Interactions in Exciton-Polariton Condensates. *arXiv:1311.4847 [cond-mat, physics:nlin]*, nov 2013.

[10] K. Dunnett and M. H. Szymańska. Keldysh field theory for nonequilibrium condensation in a parametrically pumped polariton system. *Physical Review B*, 93(19), may 2016. ISSN 2469-9950, 2469-9969. doi: 10.1103/PhysRevB.93.195306.

[11] L. M. Sieberer, M. Buchhold, and S. Diehl. Keldysh Field Theory for Driven Open Quantum Systems. *arXiv:1512.00637 [cond-mat]*, dec 2015.

[12] A. Griffin, D. W. Snoke, and S. Stringari. *Bose-Einstein Condensation*. Cambridge University Press, jul 1996. ISBN 9780521589901.

[13] Michiel Wouters and Iacopo Carusotto. Excitations in a Nonequilibrium Bose-Einstein Condensate of Exciton Polaritons. *Physical Review Letters*, 99(14):140402, oct 2007. doi: 10.1103/PhysRevLett.99.140402.

[14] Alexis Askitopoulos. *Polariton condensates in optical traps and strong magnetic fields*. PhD thesis, University of Southampton, sep 2015.

[15] Yongbao Sun, Yoseob Yoon, Saeed Khan, Li Ge, Mark Steger, Loren N. Pfeiffer, Ken West, Hakan E. Türeci, David W. Snoke, and Keith A. Nelson. Stable switching among high-order modes in polariton condensates. *Physical Review B*, 97(4):045303, jan 2018. ISSN 2469-9950. doi: 10.1103/PhysRevB.97.045303.

[16] Jonathan Keeling and Natalia G. Berloff. Spontaneous Rotating Vortex Lattices in a Pumped Decaying Condensate. *Physical Review Letters*, 100(25):250401, jun 2008. doi: 10.1103/PhysRevLett.100.250401.

[17] Michiel Wouters. Energy relaxation in the mean-field description of polariton condensates. *New Journal of Physics*, 14(7):075020, 2012. ISSN 1367-2630. doi: 10.1088/1367-2630/14/7/075020.

[18] I. G. Savenko, T. C. H. Liew, and I. A. Shelykh. Stochastic Gross-Pitaevskii Equation for the Dynamical Thermalization of Bose-Einstein Condensates. *Physical Review Letters*, 110(12):127402, mar 2013. doi: 10.1103/PhysRevLett.110.127402.

[19] Michiel Wouters and Vincenzo Savona. Stochastic classical field model for polariton condensates. *Physical Review B*, 79(16):165302, apr 2009. doi: 10.1103/PhysRevB.79.165302.

[20] P. R. Eastham. Mode locking and mode competition in a nonequilibrium solid-state condensate. *Physical Review B*, 78(3):035319, jul 2008. doi: 10.1103/PhysRevB.78.035319.

[21] A. Askitopoulos, T. C. H. Liew, H. Ohadi, Z. Hatzopoulos, P. G. Savvidis, and P. G. Lagoudakis. Robust platform for engineering pure-quantum-state transitions in polariton condensates. *Physical Review B*, 92(3):035305, jul 2015. doi: 10.1103/PhysRevB.92.035305.

[22] T. Gao, G. Li, E. Estrecho, T.C.H. Liew, D. Comber-Todd, A. Nalitov, M. Steger, K. West, L. Pfeiffer, D.W. Snoke, A.V. Kavokin, A.G. Truscott, and E.A. Ostrovskaya. Chiral Modes at Exceptional Points in Exciton-Polariton Quantum Fluids. *Physical Review Letters*, 120(6):065301, feb 2018. ISSN 0031-9007. doi: 10.1103/PhysRevLett.120.065301.

[23] C Schneider, K Winkler, M D Fraser, M Kamp, Y Yamamoto, E A Ostrovskaya, and S Höfling. Exciton-polariton trapping and potential landscape engineering. *Reports on Progress in Physics*, 80(1):016503, jan 2017. ISSN 0034-4885. doi: 10.1088/0034-4885/80/1/016503.

[24] T. Gutbrod, M. Bayer, A. Forchel, J. P. Reithmaier, T. L. Reinecke, S. Rudin, and P. A. Knipp. Weak and strong coupling of photons and excitons in photonic dots. *Physical Review B*, 57(16):9950–9956, apr 1998. ISSN 0163-1829. doi: 10.1103/ PhysRevB.57.9950.

[25] M. Bayer, T. Gutbrod, A. Forchel, T. L. Reinecke, P. A. Knipp, R. Werner, and J. P. Reithmaier. Optical Demonstration of a Crystal Band Structure Formation. *Physical Review Letters*, 83(25):5374–5377, dec 1999. ISSN 0031-9007. doi: 10. 1103/PhysRevLett.83.5374.

[26] O. El Daïf, A. Baas, T. Guillet, J.-P. Brantut, R. Idrissi Kaitouni, J. L. Staehli, F. Morier-Genoud, and B. Deveaud. Polariton quantum boxes in semiconductor microcavities. *Applied Physics Letters*, 88(6):061105, feb 2006. ISSN 0003-6951. doi: 10.1063/1.2172409.

[27] Pierre Lugan, Davide Sarchi, and Vincenzo Savona. Theory of trapped polaritons in patterned microcavities. *physica status solidi (c)*, 3(7):2428–2431, aug 2006. ISSN 1610-1634. doi: 10.1002/pssc.200668045.

[28] Karol Winkler, Julian Fischer, Anne Schade, Matthias Amthor, Robert Dall, Jonas Geßler, Monika Emmerling, Elena A Ostrovskaya, Martin Kamp, Christian Schneider, and Sven Höfling. A polariton condensate in a photonic crystal potential landscape. *New Journal of Physics*, 17(2):023001, jan 2015. ISSN 1367-2630. doi: 10.1088/1367-2630/17/2/023001.

[29] G. Tosi, G. Christmann, N. G. Berloff, P. Tsotsis, T. Gao, Z. Hatzopoulos, P. G. Savvidis, and J. J. Baumberg. Sculpting oscillators with light within a nonlinear quantum fluid. *Nature Physics*, 8(3):190–194, mar 2012. ISSN 1745-2473. doi: 10.1038/nphys2182.

[30] E. Estrecho, T. Gao, N. Bobrovska, M. D. Fraser, M. Steger, L. Pfeiffer, K. West, T. C. H. Liew, M. Matuszewski, D. W. Snoke, A. G. Truscott, and E. A. Ostrovskaya. Single-shot condensation of exciton polaritons and the hole burning effect. *Nature Communications*, 9(1):2944, dec 2018. ISSN 2041-1723. doi: 10.1038/s41467-018-05349-4.

[31] Carl M. Bender. Introduction to PT-Symmetric Quantum Theory. *Contemporary Physics*, 46(4):277–292, jul 2005. ISSN 0010-7514, 1366-5812. doi: 10.1080/ 00107500072632.

[32] Carl M. Bender. Making sense of non-Hermitian Hamiltonians. *Reports on Progress in Physics*, 70(6):947, 2007. ISSN 0034-4885. doi: 10.1088/0034-4885/70/6/R03.

[33] Ali Mostafazadeh. Pseudo-hermitian representation of quantum mechanics. *International Journal of Geometric Methods in Modern Physics*, 07(07):1191–1306, nov 2010. ISSN 0219-8878. doi: 10.1142/S0219887810004816.

[34] Nimrod Moiseyev. *Non-Hermitian Quantum Mechanics*. Cambridge University Press, feb 2011. ISBN 978-1-139-49699-5.

[35] Carl M. Bender and Stefan Boettcher. Real Spectra in Non-Hermitian Hamiltonians Having P T Symmetry. *Physical Review Letters*, 80(24):5243–5246, jun 1998. ISSN 0031-9007. doi: 10.1103/PhysRevLett.80.5243.

[36] A A Zyablovsky, A P Vinogradov, A A Pukhov, A V Dorofeenko, and A A Lisyansky. PT-symmetry in optics. *Physics-Uspekhi*, 57(11):1063–1082, nov 2014. ISSN 1063-7869, 1468-4780. doi: 10.3367/UFNe.0184.201411b.1177.

[37] Ramy El-Ganainy, Konstantinos G. Makris, Mercedeh Khajavikhan, Ziad H. Musslimani, Stefan Rotter, and Demetrios N. Christodoulides. Non-Hermitian physics and PT symmetry. *Nature Physics*, 14(1):11–19, jan 2018. ISSN 1745-2473. doi: 10.1038/nphys4323.

[38] W D Heiss. The physics of exceptional points. *Journal of Physics A: Mathematical and Theoretical*, 45(44):444016, nov 2012. ISSN 1751-8113. doi: 10.1088/1751-8113/45/44/444016.

[39] Carl M. Bender, Dorje C. Brody, and Hugh F. Jones. Complex Extension of Quantum Mechanics. *Physical Review Letters*, 89(27):270401, dec 2002. ISSN 0031-9007. doi: 10.1103/PhysRevLett.89.270401.

[40] Ali Mostafazadeh and Ahmet Batal. Physical aspects of pseudo-Hermitian and PT -symmetric quantum mechanics. *Journal of Physics A: Mathematical and General*, 37(48):11645, 2004. ISSN 0305-4470. doi: 10.1088/0305-4470/37/48/009.

[41] Carl M. Bender, Stefan Boettcher, Peter N. Meisinger, and Qinghai Wang. Two-point Green's function in PT-symmetric theories. *Physics Letters A*, 302(5-6):286–290, sep 2002. ISSN 0375-9601. doi: 10.1016/S0375-9601(02)01196-9.

[42] Carl M. Bender and Barnabas Tan. Calculation of the hidden symmetry operator for a $PT$ -symmetric square well. *Journal of Physics A: Mathematical and General*, 39(8):1945, 2006. ISSN 0305-4470. doi: 10.1088/0305-4470/39/8/011.

[43] Carl M. Bender. Four easy pieces. *Journal of Physics A: Mathematical and General*, 39(32):9993, 2006. ISSN 0305-4470. doi: 10.1088/0305-4470/39/32/S04.

[44] M.V. Berry. Physics of Nonhermitian Degeneracies. *Czechoslovak Journal of Physics*, 54(10):1039–1047, oct 2004. ISSN 0011-4626. doi: 10.1023/B:CJOP.0000044002.05657.04.

[45] Markus Müller and Ingrid Rotter. Exceptional points in open quantum systems. *Journal of Physics A: Mathematical and Theoretical*, 41(24):244018, jun 2008. ISSN 1751-8113. doi: 10.1088/1751-8113/41/24/244018.

[46] C. Dembowski, B. Dietz, H.-D. Gräf, H. L. Harney, A. Heine, W. D. Heiss, and A. Richter. Encircling an exceptional point. *Physical Review E*, 69(5):056216, may 2004. ISSN 1539-3755. doi: 10.1103/PhysRevE.69.056216.

[47] Mohammad-Ali Miri and Andrea Alù. Exceptional points in optics and photonics. *Science (New York, N.Y.)*, 363(6422):eaar7709, jan 2019. ISSN 1095-9203. doi: 10.1126/science.aar7709.

[48] T Stehmann, W D Heiss, and F G Scholtz. Observation of exceptional points in electronic circuits. *Journal of Physics A: Mathematical and General*, 37(31):7813–7819, aug 2004. ISSN 0305-4470. doi: 10.1088/0305-4470/37/31/012.

[49] Patrick Dorey, Clare Dunning, Anna Lishman, and Roberto Tateo. {\cal PT} symmetry breaking and exceptional points for a class of inhomogeneous complex potentials. *Journal of Physics A: Mathematical and Theoretical*, 42(46):465302, nov 2009. ISSN 1751-8113. doi: 10.1088/1751-8113/42/46/465302.

[50] W D Heiss, F G Scholtz, and H B Geyer. The large <i>N</i> behaviour of the Lipkin model and exceptional points. *Journal of Physics A: Mathematical and General*, 38(9):1843–1851, mar 2005. ISSN 0305-4470. doi: 10.1088/0305-4470/38/9/002.

[51] W. D. Heiss. Repulsion of resonance states and exceptional points. *Physical Review E*, 61(1):929–932, jan 2000. ISSN 1063-651X. doi: 10.1103/PhysRevE.61.929.

[52] W. D. Heiss and W.H. Steeb. Avoided level crossings and Riemann sheet structure. *Journal of Mathematical Physics*, 32(11):3003–3007, nov 1991. ISSN 0022-2488. doi: 10.1063/1.529044.

[53] Bo Peng, ahin Kaya Özdemir, Fuchuan Lei, Faraz Monifi, Mariagiovanna Gianfreda, Gui Lu Long, Shanhui Fan, Franco Nori, Carl M. Bender, and Lan Yang. Paritytime-symmetric whispering-gallery microcavities. *Nature Physics*, 10(5):394–398, may 2014. ISSN 1745-2473. doi: 10.1038/nphys2927.

[54] Hossein Hodaei, Mohammad-Ali Miri, Matthias Heinrich, Demetrios N Christodoulides, and Mercedeh Khajavikhan. Parity-time-symmetric microring lasers. *Science (New York, N.Y.)*, 346(6212):975–8, nov 2014. ISSN 1095-9203. doi: 10.1126/science.1258480.

[55] Henri Benisty, Chen Yan, Aloyse Degiron, and Anatole T. Lupu. Healing Near-PT-Symmetric Structures to Restore Their Characteristic Singularities: Analysis and Examples. *Journal of Lightwave Technology*, 30(16):2675–2683, aug 2012. ISSN 15582213. doi: 10.1109/JLT.2012.2205222.

[56] Liang Feng, Zi Jing Wong, Ren-Min Ma, Yuan Wang, and Xiang Zhang. Single-mode laser by parity-time symmetry breaking. *Science (New York, N.Y.)*, 346(6212):972–5, nov 2014. ISSN 1095-9203. doi: 10.1126/science.1258479.

[57] Henri Benisty, Aloyse Degiron, Anatole Lupu, André De Lustrac, Sébastien Chénais, Sébastien Forget, Mondher Besbes, Grégory Barbillon, Aurélien Bruyant, Sylvain Blaize, and Gilles Lérondel. Implementation of PT symmetric devices using plasmonics: principle and applications. *Optics Express*, 19(19):18004, sep 2011. ISSN 1094-4087. doi: 10.1364/OE.19.018004.

[58] Sergey V. Suchkov, Andrey A. Sukhorukov, Jiahao Huang, Sergey V. Dmitriev, Chaohong Lee, and Yuri S. Kivshar. Nonlinear switching and solitons in PT-symmetric photonic systems. *Laser & Photonics Reviews*, 10(2):177–213, mar 2016. ISSN 1863-8899. doi: 10.1002/lpor.201500227.

[59] Jan Wiersig. Sensors operating at exceptional points: General theory. *Physical Review A*, 93(3):033809, mar 2016. ISSN 2469-9926. doi: 10.1103/PhysRevA.93.033809.

[60] Jan Wiersig. Enhancing the Sensitivity of Frequency and Energy Splitting Detection by Using Exceptional Points: Application to Microcavity Sensors for Single-Particle Detection. *Physical Review Letters*, 112(20):203901, may 2014. ISSN 0031-9007. doi: 10.1103/PhysRevLett.112.203901.

[61] Weijian Chen, ahin Kaya Özdemir, Guangming Zhao, Jan Wiersig, and Lan Yang. Exceptional points enhance sensing in an optical microcavity. *Nature*, 548(7666): 192–196, aug 2017. ISSN 0028-0836. doi: 10.1038/nature23281.

[62] Weijian Chen, Jing Zhang, Bo Peng, ahin Kaya Özdemir, Xudong Fan, and Lan Yang. Parity-time-symmetric whispering-gallery mode nanoparticle sensor [Invited]. *Photonics Research*, 6(5):A23, may 2018. ISSN 2327-9125. doi: 10.1364/PRJ.6. 000A23.

[63] W.D. Heiss and H.L. Harney. The chirality of exceptional points. *The European Physical Journal D*, 17(2):149–151, nov 2001. ISSN 14346060. doi: 10.1007/ s100530170017.

[64] Ingrid Rotter. A non-Hermitian Hamilton operator and the physics of open quantum systems. *Journal of Physics A: Mathematical and Theoretical*, 42(15):153001, apr 2009. ISSN 1751-8113. doi: 10.1088/1751-8113/42/15/153001.

[65] C. Dembowski, B. Dietz, H.-D. Gräf, H. L. Harney, A. Heine, W. D. Heiss, and A. Richter. Observation of a Chiral State in a Microwave Cavity. *Physical Review Letters*, 90(3):034101, jan 2003. ISSN 0031-9007. doi: 10.1103/PhysRevLett.90. 034101.

[66] Jan Wiersig, Sang Wook Kim, and Martina Hentschel. Asymmetric scattering and nonorthogonal mode patterns in optical microspirals. *Physical Review A*, 78(5): 053809, nov 2008. ISSN 1050-2947. doi: 10.1103/PhysRevA.78.053809.

[67] Jan Wiersig, Alexander Eberspächer, Jeong-Bo Shim, Jung-Wan Ryu, Susumu Shinohara, Martina Hentschel, and Henning Schomerus. Nonorthogonal pairs of copropagating optical modes in deformed microdisk cavities. *Physical Review A*, 84 (2):023845, aug 2011. ISSN 1050-2947. doi: 10.1103/PhysRevA.84.023845.

[68] Jan Wiersig. Structure of whispering-gallery modes in optical microdisks perturbed by nanoparticles. *Physical Review A*, 84(6):063828, dec 2011. ISSN 1050-2947. doi: 10.1103/PhysRevA.84.063828.

[69] O. V. Shramkova and G. P. Tsironis. Scattering properties of PT - symmetric layered periodic structures. *Journal of Optics*, 18(10):105101, 2016. ISSN 2040-8986. doi: 10.1088/2040-8978/18/10/105101.

[70] Xiaobo Yin and Xiang Zhang. Unidirectional light propagation at exceptional points. *Nature Materials*, 12(3):175–177, mar 2013. ISSN 1476-1122. doi: 10.1038/nmat3576.

[71] Liang Feng, Ye-Long Xu, William S. Fegadolli, Ming-Hui Lu, José E. B. Oliveira, Vilson R. Almeida, Yan-Feng Chen, and Axel Scherer. Experimental demonstration of a unidirectional reflectionless parity-time metamaterial at optical frequencies. *Nature Materials*, 12(2):108–113, feb 2013. ISSN 1476-1122. doi: 10.1038/nmat3495.

[72] C. Dembowski, H.-D. Gräf, H. L. Harney, A. Heine, W. D. Heiss, H. Rehfeld, and A. Richter. Experimental Observation of the Topological Structure of Exceptional Points. *Physical Review Letters*, 86(5):787–790, jan 2001. ISSN 0031-9007. doi: 10.1103/PhysRevLett.86.787.

[73] Raam Uzdin, Alexei Mailybaev, and Nimrod Moiseyev. On the observability and asymmetry of adiabatic state flips generated by exceptional points. *Journal of Physics A: Mathematical and Theoretical*, 44(43):435302, oct 2011. ISSN 1751-8113. doi: 10.1088/1751-8113/44/43/435302.

[74] Jörg Doppler, Alexei A. Mailybaev, Julian Böhm, Ulrich Kuhl, Adrian Girschik, Florian Libisch, Thomas J. Milburn, Peter Rabl, Nimrod Moiseyev, and Stefan Rotter. Dynamically encircling an exceptional point for asymmetric mode switching. *Nature*, 537(7618):76–79, sep 2016. ISSN 0028-0836. doi: 10.1038/nature18605.

[75] H. Xu, D. Mason, Luyao Jiang, and J. G. E. Harris. Topological energy transfer in an optomechanical system with exceptional points. *Nature*, 537(7618):80–83, sep 2016. ISSN 0028-0836. doi: 10.1038/nature18604.

[76] Henri Menke, Marcel Klett, Holger Cartarius, Jörg Main, and Günter Wunner. State flip at exceptional points in atomic spectra. *Physical Review A*, 93(1):013401, jan 2016. ISSN 2469-9926. doi: 10.1103/PhysRevA.93.013401.

[77] M. Liertzer, Li Ge, A. Cerjan, A. D. Stone, H. E. Türeci, and S. Rotter. Pump-Induced Exceptional Points in Lasers. *Physical Review Letters*, 108(17):173901, apr 2012. doi: 10.1103/PhysRevLett.108.173901.

[78] M. Brandstetter, M. Liertzer, C. Deutsch, P. Klang, J. Schöberl, H. E. Türeci, G. Strasser, K. Unterrainer, and S. Rotter. Reversing the pump dependence of a laser at an exceptional point. *Nature Communications*, 5:4034, jun 2014. ISSN 2041-1723. doi: 10.1038/ncomms5034.

[79] K. Y. Bliokh, Y. P. Bliokh, V. Freilikher, A. Z. Genack, and P. Sebbah. Coupling and Level Repulsion in the Localized Regime: From Isolated to Quasiextended Modes. *Physical Review Letters*, 101(13):133901, sep 2008. doi: 10.1103/PhysRevLett.101.133901.

[80] O. Atabek, R. Lefebvre, M. Lepers, A. Jaouadi, O. Dulieu, and V. Kokoouline. Proposal for a Laser Control of Vibrational Cooling in Na 2 Using Resonance Coalescence. *Physical Review Letters*, 106(17):173002, apr 2011. ISSN 0031-9007. doi: 10.1103/PhysRevLett.106.173002.

[81] G. C. Righini, Y. Dumeige, P. Féron, M. Ferrari, G. Nunzi Conti, D. Ristic, and S. Soria. Whispering Gallery Mode microresonators: Fundamentals and applications. *Rivista del Nuovo Cimento*, 34(7):435–488, 2011. ISSN 0393697X. doi: 10.1393/ncr/i2011-10067-2.

[82] Jan Wiersig, Chang-Hwan Yi, and Julius Kullig. Exceptional Points in Whispering-Gallery Microcavities. In *2018 IEEE Photonics Society Summer Topical Meeting Series (SUM)*, pages 241–242. IEEE, jul 2018. ISBN 978-1-5386-5343-2. doi: 10.1109/PHOSST.2018.8456794.

[83] A. Guo, G. J. Salamo, D. Duchesne, R. Morandotti, M. Volatier-Ravat, V. Aimez, G. A. Siviloglou, and D. N. Christodoulides. Observation of ${P}{T}$-Symmetry Breaking in Complex Optical Potentials. *Physical Review Letters*, 103(9):093902, aug 2009. doi: 10.1103/PhysRevLett.103.093902.

[84] K. G. Makris, R. El-Ganainy, D. N. Christodoulides, and Z. H. Musslimani. Beam Dynamics in P T Symmetric Optical Lattices. *Physical Review Letters*, 100(10): 103904, mar 2008. ISSN 0031-9007. doi: 10.1103/PhysRevLett.100.103904.

[85] Heinz-Peter Breuer and Francesco Petruccione. *The Theory of Open Quantum Systems*. Oxford University Press, jan 2007. ISBN 9780199213900. doi: 10.1093/acprof: oso/9780199213900.001.0001.

[86] Vladimir V. Konotop, Jianke Yang, and Dmitry A. Zezyulin. Nonlinear waves in PT -symmetric systems. *Reviews of Modern Physics*, 88(3):035002, jul 2016. ISSN 0034-6861. doi: 10.1103/RevModPhys.88.035002.

[87] Ralf Labouvie, Bodhaditya Santra, Simon Heun, Sandro Wimberger, and Herwig Ott. Negative Differential Conductivity in an Interacting Quantum Gas. *Physical Review Letters*, 115(5):050601, jul 2015. ISSN 0031-9007. doi: 10.1103/ PhysRevLett.115.050601.

[88] Nicholas P. Robins, Cristina Figl, Matthew Jeppesen, Graham R. Dennis, and John D. Close. A pumped atom laser. *Nature Physics*, 4(9):731–736, sep 2008. ISSN 1745-2473. doi: 10.1038/nphys1027.

[89] Andreas Müllers, Bodhaditya Santra, Christian Baals, Jian Jiang, Jens Benary, Ralf Labouvie, Dmitry A. Zezyulin, Vladimir V. Konotop, and Herwig Ott. Coherent perfect absorption of nonlinear matter waves. *Science Advances*, 4(8):eaat6539, aug 2018. ISSN 2375-2548. doi: 10.1126/sciadv.aat6539.

[90] Ralf Labouvie, Bodhaditya Santra, Simon Heun, and Herwig Ott. Bistability in a Driven-Dissipative Superfluid. *Physical Review Letters*, 116(23):235302, jun 2016. ISSN 0031-9007. doi: 10.1103/PhysRevLett.116.235302.

[91] G. Barontini, R. Labouvie, F. Stubenrauch, A. Vogler, V. Guarrera, and H. Ott. Controlling the Dynamics of an Open Many-Body Quantum System with Localized Dissipation. *Physical Review Letters*, 110(3):035302, jan 2013. ISSN 0031-9007. doi: 10.1103/PhysRevLett.110.035302.

[92] Eva-Maria Graefe. Stationary states of a PT symmetric two-mode BoseEinstein condensate. *Journal of Physics A: Mathematical and Theoretical*, 45(44):444015, 2012. ISSN 1751-8121. doi: 10.1088/1751-8113/45/44/444015.

[93] Holger Cartarius and Günter Wunner. Model of a PT -symmetric Bose-Einstein condensate in a $\delta$ -function double-well potential. *Physical Review A*, 86(1):013612, jul 2012. ISSN 1050-2947. doi: 10.1103/PhysRevA.86.013612.

[94] Dennis Dast, Daniel Haag, Holger Cartarius, Jörg Main, and Günter Wunner. Eigenvalue structure of a BoseEinstein condensate in a PT-symmetric double well. *Journal of Physics A: Mathematical and Theoretical*, 46(37):375301, sep 2013. ISSN 1751-8113. doi: 10.1088/1751-8113/46/37/375301.

[95] Daniel Haag, Dennis Dast, Andreas Löhle, Holger Cartarius, Jörg Main, and Günter Wunner. Nonlinear quantum dynamics in a PT -symmetric double well. *Physical Review A*, 89(2):023601, feb 2014. ISSN 1050-2947. doi: 10.1103/PhysRevA.89. 023601.

[96] Manuel Kreibich, Jörg Main, Holger Cartarius, and Günter Wunner. Realizing PT -symmetric non-Hermiticity with ultracold atoms and Hermitian multi-well potentials. *Physical Review A*, 90(3):033630, sep 2014. ISSN 1050-2947. doi: 10.1103/PhysRevA.90.033630.

[97] Jiun-Yi Lien, Yueh-Nan Chen, Natsuko Ishida, Hong-Bin Chen, Chi-Chuan Hwang, and Franco Nori. Multistability and condensation of exciton-polaritons below threshold. *Physical Review B*, 91(2):024511, jan 2015. doi: 10.1103/PhysRevB. 91.024511.

[98] Igor Yu Chestnov, Sevak S Demirchyan, Alexander P Alodjants, Yuri G Rubo, and Alexey V Kavokin. Permanent Rabi oscillations in coupled exciton-photon systems with PT-symmetry. *Scientific reports*, 6:19551, jan 2016. ISSN 2045-2322. doi: 10.1038/srep19551.

[99] Hassan K. Khalil. *Nonlinear systems*. Prentice Hall, 2002. ISBN 0130673897.

[100] Z. H. Musslimani, K. G. Makris, R. El-Ganainy, and D. N. Christodoulides. Optical Solitons in P T Periodic Potentials. *Physical Review Letters*, 100(3):030402, jan 2008. ISSN 0031-9007. doi: 10.1103/PhysRevLett.100.030402.

[101] Fatkhulla Kh. Abdullaev, Yaroslav V. Kartashov, Vladimir V. Konotop, and Dmitry A. Zezyulin. Solitons in PT -symmetric nonlinear lattices. *Physical Review A*, 83(4):041805, apr 2011. ISSN 1050-2947. doi: 10.1103/PhysRevA.83.041805.

[102] Andrey E. Miroshnichenko, Boris A. Malomed, and Yuri S. Kivshar. Nonlinearly PT -symmetric systems: Spontaneous symmetry breaking and transmission resonances. *Physical Review A*, 84(1):012123, jul 2011. ISSN 1050-2947. doi: 10.1103/PhysRevA.84.012123.

[103] Martin Wimmer, Alois Regensburger, Mohammad-Ali Miri, Christoph Bersch, Demetrios N. Christodoulides, and Ulf Peschel. Observation of optical solitons in PT-symmetric lattices. *Nature Communications*, 6(1):7782, nov 2015. ISSN 2041-1723. doi: 10.1038/ncomms8782.

[104] Absar U. Hassan, Hossein Hodaei, Mohammad-Ali Miri, Mercedeh Khajavikhan, and Demetrios N. Christodoulides. Nonlinear reversal of the PT -symmetric phase transition in a system of coupled semiconductor microring resonators. *Physical Review A*, 92(6):063807, dec 2015. ISSN 1050-2947. doi: 10.1103/PhysRevA.92.063807.

[105] Li Ge and Ramy El-Ganainy. Nonlinear modal interactions in parity-time (PT) symmetric lasers. *Scientific Reports*, 6(1):24889, jul 2016. ISSN 2045-2322. doi: 10.1038/srep24889.

[106] Haydar Uncu and Ersan Demiralp. Bound state solutions of the Schrödinger equation for a PT-symmetric potential with Dirac delta functions. 2006.

[107] E M Graefe, U Günther, H J Korsch, and A E Niederle. A non-Hermitian \mathcal{P}\mathcal{T} symmetric BoseHubbard model: eigenvalue rings from unfolding higher-order exceptional points. *Journal of Physics A: Mathematical and Theoretical*, 41(25):255206, jun 2008. ISSN 1751-8113. doi: 10.1088/1751-8113/41/25/255206.

[108] Eva Maria Graefe and Hans Jürgen Korsch. Crossing scenario for a nonlinear non-Hermitian two-level system. *Czechoslovak Journal of Physics*, 56(9):1007–1020, 2006. ISSN 0011-4626, 1572-9486. doi: 10.1007/s10582-006-0396-8.

[109] MILOSLAV ZNOJIL and GÉZA LÉVAI. SPONTANEOUS BREAKDOWN OF PT SYMMETRY IN THE SOLVABLE SQUARE-WELL MODEL. *Modern Physics Letters A*, 16(35):2273–2280, nov 2001. ISSN 0217-7323. doi: 10.1142/S0217732301005722.

[110] Miloslav Znojil. PT-symmetric square well. *Physics Letters A*, 285(12):7–10, jun 2001. ISSN 0375-9601. doi: 10.1016/S0375-9601(01)00301-2.

[111] Miloslav Znojil. Solvable PT-symmetric model with a tunable interspersion of non-merging levels. *Journal of Mathematical Physics*, 46(6):062109, jun 2005. ISSN 0022-2488, 1089-7658. doi: 10.1063/1.1925249.

[112] Miloslav Znojil. Fragile PT-symmetry in a solvable model. *Journal of Mathematical Physics*, 45(11):4418–4430, nov 2004. ISSN 0022-2488. doi: 10.1063/1.1803928.

[113] E. Wertz, L. Ferrier, D. D. Solnyshkov, R. Johne, D. Sanvitto, A. Lemaître, I. Sagnes, R. Grousson, A. V. Kavokin, P. Senellart, G. Malpuech, and J. Bloch. Spontaneous formation and optical manipulation of extended polariton condensates. *Nature Physics*, 6(11):860–864, nov 2010. ISSN 1745-2473. doi: 10.1038/nphys1750.

[114] C Antón, T C H Liew, G Tosi, M D Martín, T Gao, Z Hatzopoulos, P S Eldridge, P G Savvidis, and L Viña. Energy relaxation of exciton-polariton condensates in quasi-one-dimensional microcavities. *PHYSICAL REVIEW B*, 88(71), 2013. doi: 10.1103/PhysRevB.88.035313.

[115] Aurélien Trichet, Emilien Durupt, François Médard, Sanjoy Datta, Anna Minguzzi, and Maxime Richard. Long-range correlations in a 97% excitonic one-dimensional polariton condensate. *Physical Review B*, 88(12):121407, sep 2013. ISSN 1098-0121. doi: 10.1103/PhysRevB.88.121407.

[116] R. Balili, V. Hartwell, D. Snoke, L. Pfeiffer, and K. West. Bose-Einstein Condensation of Microcavity Polaritons in a Trap. *Science*, 316(5827):1007–1010, may 2007. ISSN 0036-8075, 1095-9203. doi: 10.1126/science.1140990.

[117] Lloyd N Trefethen. Spectral Methods in Matlab. *Lloydia Cincinnati*, 10:184, 2000. ISSN 0586-7614. doi: 10.1137/1.9780898719598.

[118] Marco Ornigotti and Alexander Szameit. Quasi $$ -symmetry in passive photonic lattices. *Journal of Optics*, 16(6):065501, 2014. ISSN 2040-8986. doi: 10.1088/2040-8978/16/6/065501.

[119] H. Benisty and M. Besbes. Confinement and optical properties of the plasmonic inverse-rib waveguide. *Journal of the Optical Society of America B*, 29(4):818, apr 2012. ISSN 0740-3224. doi: 10.1364/JOSAB.29.000818.

[120] F. Tassone and Y. Yamamoto. Exciton-exciton scattering dynamics in a semiconductor microcavity and stimulated scattering into polaritons. *Physical Review B*, 59 (16):10830–10842, apr 1999. doi: 10.1103/PhysRevB.59.10830.

[121] Lord Rayleigh. CXII. <i>The problem of the whispering gallery</i>. *The London, Edinburgh, and Dublin Philosophical Magazine and Journal of Science*, 20(120): 1001–1004, dec 1910. ISSN 1941-5982. doi: 10.1080/14786441008636993.

[122] Gaël Reecht, Hervé Bulou, Fabrice Scheurer, Virginie Speisser, Bernard Carrière, Fabrice Mathevet, and Guillaume Schull. Oligothiophene Nanorings as Electron Resonators for Whispering Gallery Modes. *Physical Review Letters*, 110(5):056802, jan 2013. ISSN 0031-9007. doi: 10.1103/PhysRevLett.110.056802.

[123] Liaoxin Sun, Zhanghai Chen, Qijun Ren, Ke Yu, Lihui Bai, Weihang Zhou, Hui Xiong, Z. Q. Zhu, and Xuechu Shen. Direct Observation of Whispering Gallery Mode Polaritons and their Dispersion in a ZnO Tapered Microcavity. *Physical Review Letters*, 100(15):156403, apr 2008. ISSN 0031-9007. doi: 10.1103/PhysRevLett.100. 156403.

[124] C. P. Dietrich, R. Johne, T. Michalsky, C. Sturm, P. Eastham, H. Franke, M. Lange, M. Grundmann, and R. Schmidt-Grund. Parametric relaxation in whispering gallery mode exciton-polariton condensates. *Physical Review B*, 91(4):041202, jan 2015. ISSN 1098-0121. doi: 10.1103/PhysRevB.91.041202.

[125] A. Yu. Voronin, V. V. Nesvizhevsky, and S. Reynaud. Whispering-gallery states of antihydrogen near a curved surface. *Physical Review A*, 85(1):014902, jan 2012. ISSN 1050-2947. doi: 10.1103/PhysRevA.85.014902.

[126] Dmitry V Strekalov, Christoph Marquardt, Andrey B Matsko, Harald G L Schwefel, and Gerd Leuchs. Nonlinear and quantum optics with whispering gallery resonators. *Journal of Optics*, 18(12):123002, dec 2016. ISSN 2040-8978. doi: 10.1088/2040-8978/18/12/123002.

[127] A. Monakhov and N. Sablina. Whispering gallery mode lasers. *Semiconductor Lasers*, pages 551–578, jan 2013. doi: 10.1533/9780857096401.3.551.

[128] Matthew R Foreman, Jon D Swaim, and Frank Vollmer. Whispering gallery mode sensors. *Advances in optics and photonics*, 7(2):168–240, jun 2015. ISSN 1943-8206. doi: 10.1364/AOP.7.000168.

[129] M. A. Kaliteevski, S. Brand, R. A. Abram, A. Kavokin, and Le Si Dang. Whispering gallery polaritons in cylindrical cavities. *Physical Review B*, 75(23):233309, jun 2007. ISSN 1098-0121. doi: 10.1103/PhysRevB.75.233309.

[130] Hongxing Dong, Beier Zhou, Jingzhou Li, Jingxin Zhan, and Long Zhang. Ultraviolet lasing behavior in ZnO optical microcavities. *Journal of Materiomics*, 3(4): 255–266, dec 2017. ISSN 2352-8478. doi: 10.1016/J.JMAT.2017.06.001.

[131] Christian Czekalla, Chris Sturm, Rüdiger Schmidt-Grund, Bingqiang Cao, Michael Lorenz, and Marius Grundmann. Whispering gallery mode lasing in zinc oxide microwires. *Applied Physics Letters*, 92(24):241102, jun 2008. ISSN 0003-6951. doi: 10.1063/1.2946660.

[132] Qingqing Duan, Dan Xu, Wenhui Liu, Jian Lu, Long Zhang, Jian Wang, Yinglei Wang, Jie Gu, Tao Hu, Wei Xie, Xuechu Shen, and Zhanghai Chen. Polariton lasing of quasi-whispering gallery modes in a ZnO microwire. *Applied Physics Letters*, 103 (2):022103, jul 2013. ISSN 0003-6951. doi: 10.1063/1.4813441.

[133] O. A. Egorov and D. V. Skryabin. Frequency comb generation in a resonantly pumped exciton-polariton microring resonator. *Optics Express*, 26(18):24003, sep 2018. ISSN 1094-4087. doi: 10.1364/OE.26.024003.

[134] D. Porras, C. Ciuti, J. J. Baumberg, and C. Tejedor. Polariton dynamics and Bose-Einstein condensation in semiconductor microcavities. *Physical Review B*, 66(8): 085304, aug 2002. doi: 10.1103/PhysRevB.66.085304.

[135] Jan Wiersig. Boundary element method for resonances in dielectric microcavities. *Journal of Optics A: Pure and Applied Optics*, 5(1):53–60, jan 2003. ISSN 1464-4258. doi: 10.1088/1464-4258/5/1/308.

[136] Q. Zhong, J. Ren, M. Khajavikhan, D.N. Christodoulides, .K. Özdemir, and R. El-Ganainy. Sensing with Exceptional Surfaces in Order to Combine Sensitivity with Robustness. *Physical Review Letters*, 122(15):153902, apr 2019. ISSN 0031-9007. doi: 10.1103/PhysRevLett.122.153902.

[137] Chang-Hwan Yi, Julius Kullig, and Jan Wiersig. Pair of Exceptional Points in a Microdisk Cavity under an Extremely Weak Deformation. *Physical Review Letters*, 120(9):093902, feb 2018. ISSN 0031-9007. doi: 10.1103/PhysRevLett.120.093902.

[138] Julius Kullig, Chang-Hwan Yi, and Jan Wiersig. Exceptional points by coupling of modes with different angular momenta in deformed microdisks: A perturbative analysis. *Physical Review A*, 98(2):023851, aug 2018. ISSN 2469-9926. doi: 10.1103/PhysRevA.98.023851.

[139] R. Dubertrand, E. Bogomolny, N. Djellali, M. Lebental, and C. Schmit. Circular dielectric cavity and its deformations. *Physical Review A*, 77(1):013804, jan 2008. ISSN 1050-2947. doi: 10.1103/PhysRevA.77.013804.

[140] Jan Wiersig. Perturbative approach to optical microdisks with a local boundary deformation. *Physical Review A*, 85(6):063838, jun 2012. ISSN 1050-2947. doi: 10.1103/PhysRevA.85.063838.

[141] C. P. Dettmann, G. V. Morozov, M. Sieber, and H. Waalkens. Internal and external resonances of dielectric disks. *EPL (Europhysics Letters)*, 87(3):34003, aug 2009. ISSN 0295-5075. doi: 10.1209/0295-5075/87/34003.

[142] T.C.H. Liew, I.A. Shelykh, and G. Malpuech. Polaritonic devices. *Physica E: Low-dimensional Systems and Nanostructures*, 43(9):1543–1568, jul 2011. ISSN 1386-9477. doi: 10.1016/J.PHYSE.2011.04.003.

[143] B. R. Johnson. Theory of morphology-dependent resonances: shape resonances and width formulas. *JOSA A, Vol. 10, Issue 2, pp. 343-352*, 10(2):343–352, feb 1993. ISSN 1520-8532. doi: 10.1364/JOSAA.10.000343.

[144] William H. Press. *Numerical recipes : the art of scientific computing.* Cambridge University Press, 2007. ISBN 9780521880688.

[145] G. Vanden Berghe, V. Fack, and H.E. De Meyer. Numerical methods for solving radial Schrödinger equations. *Journal of Computational and Applied Mathematics*, 28:391–401, dec 1989. ISSN 0377-0427. doi: 10.1016/0377-0427(89)90350-6.

[146] X. Leyronas and M. Combescot. Quantum wells, wires and dots with finite barrier: analytical expressions for the bound states. *Solid State Communications*, 119(10-11): 631–635, aug 2001. ISSN 0038-1098. doi: 10.1016/S0038-1098(01)00288-5.

[147] Yongbao Sun, Yoseob Yoon, Mark Steger, Gangqiang Liu, Loren N. Pfeiffer, Ken West, DavidW. Snoke, and Keith A. Nelson. Direct measurement of polaritonpolariton interaction strength. *Nature Physics*, 13(9):870–875, sep 2017. ISSN 1745-2473. doi: 10.1038/nphys4148.

[148] E. Estrecho, T. Gao, N. Bobrovska, D. Comber-Todd, M. D. Fraser, M. Steger, K. West, L. N. Pfeiffer, J. Levinsen, M. M. Parish, T. C. H. Liew, M. Matuszewski, D. W. Snoke, A. G. Truscott, and E. A. Ostrovskaya. Direct measurement of polariton-polariton interaction strength in the Thomas-Fermi regime of exciton-polariton condensation. *Physical Review B*, 100(3):035306, jul 2019. ISSN 2469-9950. doi: 10.1103/PhysRevB.100.035306.

[149] M. Pieczarka, M. Boozarjmehr, E. Estrecho, Y. Yoon, M. Steger, K. West, L. N. Pfeiffer, K. A. Nelson, D. W. Snoke, A. G. Truscott, and E. A. Ostrovskaya. Effect of optically induced potential on the energy of trapped exciton polaritons below the condensation threshold. *Physical Review B*, 100(8):085301, aug 2019. ISSN 2469-9950. doi: 10.1103/PhysRevB.100.085301.

[150] S. Choi, S. A. Morgan, and K. Burnett. Phenomenological damping in trapped atomic Bose-Einstein condensates. *Physical Review A*, 57(5):4057–4060, may 1998. doi: 10.1103/PhysRevA.57.4057.

[151] Michiel Wouters and Vincenzo Savona. Stochastic classical field model for polariton condensates. *Physical Review B*, 79(16):165302, apr 2009. ISSN 1098-0121. doi: 10.1103/PhysRevB.79.165302.

[152] J. Yang. *Nonlinear Waves in Integrable and Nonintegrable Systems.* Mathematical Modeling and Computation. Society for Industrial and Applied Mathematics, jan 2010. ISBN 978-0-89871-705-1.

[153] Benjamin Michael Caradoc-Davies. *Vortex dynamics in Bose-Einstein condensates.* PhD thesis, 2000.

[154] Bengt Fornberg. *A Practical Guide to Pseudospectral Methods.* Cambridge University Press, oct 1998. ISBN 9780521645645.

[155] Konstantinos Lagoudakis. *The Physics of Exciton-Polariton Condensates.* EFPL Press, dec 2013. ISBN 9781482212143.

[156] Yong Xu, Yi Li, Reginald K. Lee, and Amnon Yariv. Scattering-theory analysis of waveguide-resonator coupling. *Physical Review E*, 62(5):7389–7404, nov 2000. ISSN 1063-651X. doi: 10.1103/PhysRevE.62.7389.

[157] M. Asano, K. Y. Bliokh, Y. P. Bliokh, A. G. Kofman, R. Ikuta, T. Yamamoto, Y. S. Kivshar, L. Yang, N. Imoto, .K. Özdemir, and F. Nori. Anomalous time delays and quantum weak measurements in optical micro-resonators. *Nature Communications*, 7:13488, nov 2016. ISSN 2041-1723. doi: 10.1038/ncomms13488.

[158] Alexander Schlehahn, Ferdinand Albert, Christian Schneider, Sven Höfling, Stephan Reitzenstein, Jan Wiersig, and Martin Kamp. Mode selection in electrically driven quantum dot microring cavities. *Optics Express*, 21(13):15951, jul 2013. ISSN 1094-4087. doi: 10.1364/OE.21.015951.

[159] A. M. Monakhov, V. V. Sherstnev, A. P. Astakhova, Yu. P. Yakovlev, G. Boissier, R. Teissier, and A. N. Baranov. Experimental observation of whispering gallery modes in sector disk lasers. *Applied Physics Letters*, 94(5):051102, feb 2009. ISSN 0003-6951. doi: 10.1063/1.3075852.

[160] M. Wouters, T. C. H. Liew, and V. Savona. Energy relaxation in one-dimensional polariton condensates. *Physical Review B*, 82(24):245315, dec 2010. doi: 10.1103/PhysRevB.82.245315.